

Disulfide-Bridged Organosilica Frameworks: Designed, Synthesis, Redox-Triggered Biodegradation, and Nanobiomedical Applications

Xin Du,* Freddy Kleitz,* Xiaoyu Li, Hongwei Huang, Xueji Zhang, and Shi-Zhang Qiao*

Over the past few years, silica-based nanotheranostics have demonstrated their great potential for nano/biomedical applications. However, the uncontrollable and difficult degradability of their pure silica framework and long-time in vivo retention still cause severe and unpredictable toxicity risks. Therefore, it is highly desirable to design and synthesize materials with safer framework structures and compositions. To this aim, the introduction of disulfide bonds into the silica framework can not only maintain high stability in physiological conditions, but also achieve a stimuli-responsive biodegradation triggered by intracellular reducing microenvironment in living cells, especially in cancer cells. Once nanotheranostics with disulfide (i.e., thioether)-bridged silsesquioxane framework are taken up by tumor cells via passive or active targeting, the disulfide bonds in the hybrid silica matrix can be cleaved by a high concentration of intracellular glutathione, enabling redox-triggered biodegradation of the nanosystems for both concomitant release of the loaded therapeutic cargo and in vivo clearance. It is envisioned that such hybrid materials comprised of disulfide-bridged silsesquioxane frameworks can become promising responsive and biodegradable nanotheranostics. This review summarizes the recent advances in the synthesis of hybrid organosilicas with disulfide-bridged silsesquioxane frameworks, and discuss their redox-triggered biodegradation behaviors combined with their biocompatibility and nanobiomedical applications.

which offer enormous opportunities for nanobiomedicine.^[1–5] Among them, silica, which is often found in food as additives due to being safe for human consumption, is promising as a carrier platform for in vivo applications. In particular, mobile composition of matter (MCM)-41-type mesoporous silica powder was first employed as a drug (ibuprofen) carrier in 2001 and demonstrated an interesting sustained release behavior in aqueous solution.^[6] Since then, mesoporous silica nanoparticles/nanospheres (MSNs) have been considered as one of the most promising platforms for modern drug delivery systems owing to their well-defined mesopores with various pore sizes and structures for efficient drug loading, their high stability under physiological conditions, the possibility of easy and versatile functionalization, and suitable biocompatibility.^[7–36] In order to adjust the pharmacokinetic profile, reduce off-target toxicity, and improve therapeutic and diagnostic efficacy/index, many silica-based delivery and/or imaging nanosystems exhibiting


1. Introduction

1.1. Silica-Based Nanotheranostics

Nanotechnology has brought the rapid development of new smart functional materials built up of diverse components,

stimuli (pH, redox potential, enzyme, light, thermal, etc.)-responsive release and active targeting properties (by introduction of a variety of ligands such as antibodies, aptamers, and peptides) have been developed.^[7–36] The study of silica-based nanocarriers or nanoprobe has gradually evolved initially from investigations in solutions to cells, then to animal level

Prof. X. Du, Prof. X. Zhang
Research Center for Bioengineering and Sensing Technology
School of Chemistry and Biological Engineering
Beijing Key Laboratory for Bioengineering
and Sensing Technology
University of Science and Technology Beijing
Beijing 100083, P. R. China
E-mail: duxin@ustb.edu.cn

 The ORCID identification number(s) for the author(s) of this article can be found under <https://doi.org/10.1002/adfm.201707325>.

© 2018 The Authors. Published by WILEY-VCH Verlag GmbH & Co. KGaA, Weinheim. This is an open access article under the terms of the Creative Commons Attribution-NonCommercial License, which permits use, distribution and reproduction in any medium, provided the original work is properly cited and is not used for commercial purposes.

The copyright line was changed on 28th November 2018 after initial publication.

DOI: 10.1002/adfm.201707325

Prof. X. Du, Prof. S.-Z. Qiao
School of Chemical Engineering
The University of Adelaide
Adelaide, SA 5005, Australia
E-mail: s.qiao@adelaide.edu.au

Prof. F. Kleitz
Department of Inorganic Chemistry—Functional Materials
Faculty of Chemistry
University of Vienna
1090 Vienna, Austria
E-mail: freddy.kleitz@univie.ac.at

Prof. X. Li
Key Laboratory of Green Process and Engineering
Institute of Process Engineering
Chinese Academy of Sciences
Beijing 100190, P. R. China

Prof. H. Huang
School of Materials Science and Technology
China University of Geosciences
Beijing 100083, P. R. China

(e.g., mice), and finally to preclinical stage.^[7–36] Excitingly, a type of multimodal small (size: 5–7 nm) nonporous silica nanoparticles (NPs) (also known as Cornell Dots (C-Dots)) was approved by the U.S. Food and Drug Administration (FDA) in 2011 for the “first-in-human” clinical trial for target diagnostics of advanced melanoma due to specific tumor targeting imaging and efficient renal clearance.^[37,38] For this smart design, an organic dye was encapsulated in the interior of a silica shell for fluorescent imaging, while polyethylene glycol (PEG), targeting peptides (cyclic arginine–glycine–aspartic acid (cRGDY)), and radioiodine were attached on the surface of the silica shell to form ¹²⁴I-cRGDY-PEGylated core–shell silica NPs, for improved colloidal stability, enhanced tumor-selective accumulation, and positron emission tomography (PET) imaging, respectively. This success was the first use of a silica-based nanosystem for human diagnostics. Since then, the synthesis method of C-Dots has been updated from the alcohol-based modified Stöber strategy to a water-based synthesis method,^[39] and a series of small fluorescent silica NPs, aluminosilicate NPs, zirconium-89-labeled NPs, and core–shell NPs with different multiple surface functional groups (even drug molecules) were created for further nanomedicine applications.^[40–46]

Successful translation of MSN-based nanosystems from laboratory research to clinical application requires comprehensive and systematic studies in the area of in vivo nanobiomedical applications. Although many designed silica-based nanosystems/formulations exhibit superior therapeutic efficacy in small animal models, uncontrolled degradability of silica framework and long-term in vivo retention still cause potential risks.^[7–36] Therefore, their biosafety has to be investigated at different levels from the molecule, cell, blood, tissue, and finally, to animal, before preclinical and clinical trials in the near future. The study of the biosafety, including cytotoxicity, hemocompatibility, blood circulation, biodistribution, tissue penetration, in vivo toxic side effects, immune response, excretion, and biodegradability, has recently attracted increasing attention.^[7–36]

1.2. Biological Barriers and In Vivo Clearance

In order to achieve a successful targeting function of nanotherapeutics toward diseased sites, a series of successive biological barriers have to be overcome, including opsonization, sequestration by the mononuclear phagocyte system (MPS, also known as reticuloendothelial system (RES), which includes liver, spleen, lungs, etc.), abnormal biodistribution, hemorheological limitations, intratumoral pressure gradients, cellular internalization, endosomal and lysosomal escape, and drug efflux pumps.^[47–49] Therefore, the design of NPs and their parameters (e.g., size, shape, charge, deformability, and degradability) should comply with several important principles:^[47] 1) NPs with an average size of about 100 nm generally have longer-lasting half-lives in the blood circulation; 2) compared to spherical NPs, discoidal NPs are more prone to tumbling and oscillatory effects in the vasculature, which greatly improves the propensity of contact between NPs and the vessel/cell wall, and further favors NPs' binding and adhesion to the endothelium; 3) NPs with neutral and negative surface charges usually show reduced adsorption of serum proteins compared with those with positive



Xin Du received his B.Sc. in 2007 from Nankai University and Ph.D. degree in 2012 from Technical Institute of Physics and Chemistry, CAS. He pursued his research as a postdoctoral researcher at School of Chemical Engineering in The University of Adelaide, from 2012 to 2014. He is currently an Associate Professor in the Research Center for

Bioengineering and Sensing Technology, University of Science and Technology Beijing. His current research interests focus on the design and controlled synthesis of novel nanostructured silica materials as nanoreactors and nanobiomedical materials.



Freddy Kleitz is a University Professor in the Faculty of Chemistry at the University of Vienna, Austria, and is the director of the Department of Inorganic Chemistry–Functional Materials (2016). He received his Ph.D. degree in Chemistry (2002) from the Max-Planck-Institut für Kohlenforschung, Germany, with Prof. Ferdi Schüth. In 2002–2003, he was a postdoc-

toral researcher with Prof. Ryong Ryoo in KAIST (Korea). In 2005, he joined the Department of Chemistry of Université Laval, Canada, and was promoted Full Professor in 2014. His research focuses on the design of functional nanoporous materials and their applications as selective sorbents, catalysts, and biomedical materials.



Shi-Zhang Qiao received his Ph.D. degree in chemical engineering from the Hong Kong University of Science and Technology in 2000, and is currently a Chair Professor at the School of Chemical Engineering of The University of Adelaide, Australia. His research expertise is in nanomaterials and nanoporous materials for drug/gene delivery and new energy technologies.

charges, thus leading to longer-circulation half-lives. However, after arrival at the tumor location, a responsive switch to a positive charge is highly desired to facilitate cellular uptake and subsequent endosomal escape via the proton pump

mechanism; 4) deformable (soft) NPs demonstrate prolonged circulation half-lives and reduced accumulation in the spleen compared with rigid NPs; and 5) NPs should remain stable during circulation in order to prevent premature drug leakage, yet have adequate degradation/dissociation kinetics for drug release and their clearance at the tumor sites.

Once entering into the blood stream by intravenous administration, the injected NPs will be immediately surrounded by a complex and tightly bound layer of adsorbed biomolecules, thus forming the “protein corona.”^[50,51] The corona can result in the suppression of the active targeting capability, abnormal biodistribution, unexpected toxicity, and low theranostic efficacy.^[50,51] Then, the injected NPs are prone to be cleared from blood circulation primarily through two pathways: MPS and renal clearance.^[52–60] As main constituents of MPS, the Kupffer cells (KCs) of the liver and the macrophages of the spleen are responsible for clearance of large NPs, while the kidney is capable of filtering small NPs from the blood (also called glomerular filtration). Spherical NPs with a hydrodynamic diameter (HD) of ≤ 6 nm can easily cross through glomerular capillary walls, while it is hard for NPs with $HD \geq 8$ nm to pass through it.^[53–57] For intermediate HD sizes of 6–8 nm, the filtration characteristics of the NPs are not only dependent on size, shape, and charge, but also on the plasticity of the material. Thus, the kidney filtration threshold is usually regarded as ≤ 6 nm. There are several limitations:^[52–60] 1) premature elimination from blood circulation will stop NPs from accumulating in tumor sites through the enhanced permeability and retention (EPR) effect; 2) severe and long-term accumulation in RES-related organs, such as the liver and spleen, may cause toxic side effects of NPs, opsonization, and organ damage/diseases; 3) glomerular filtration, which is dependent on size, shape and surface chemistry, generally requires NPs with $HD \leq 6$ nm, and the filtrated NPs are excreted via the renal system. For biosafety, U.S. FDA states that all injected contrast agents have to be completely cleared from the body during a reasonable amount of time.^[59,60] It is worth noting that the EPR effect at sites of fast cancer growth is very important for specific tumor therapy and/or diagnosis of NP-based nanosystems. The common explanation of EPR revolves around the presence of highly fenestrated tumor blood vessels due to structural and architectural abnormalities. New insights indicate that impairment of lymphatic drainage, permeability enhancing factors, and the role of nutritional pathways contribute to the EPR effect.^[61]

On the basis of numerous studies dealing with the interactions between engineered NPs and biological systems, the creation of a “stealth layer” on the surface of NPs can achieve steric stabilization, inhibit unspecific biomolecule adsorption, and prevent interactions with immune cells.^[62,63] Therefore, this strategy may improve the colloidal stability and counter corona formation, and prolong blood circulation, diminish RES uptake, facilitate the EPR effect, and, ultimately, positively affect the biodistribution profiles and theranostic effects. The most common modification strategy is the grafting of hydrophilic polymers (such as PEG),^[64,65] PEG derivatives,^[64] zwitterionic ligands,^[66–68] or other macromolecules, such as polysaccharides or peptides) on the external surface of the nanoparticles. Most importantly, PEG has been approved by FDA,^[64] and PEGylation is always required for injection in vivo.

From an in vivo clearance standpoint, ideal nanosystems should not only be sufficiently stable in vivo to execute their function of diagnosis or/and therapy at the targeted sites, but also should completely exit the body after completion of their tasks, via the two pathways of biodegradation and/or excretion, after a suitable acting time, to avoid severe and unpredictable toxicity risks due to long-term retention in the body.^[52–60] Although the International Union of Pure and Applied Chemistry (IUPAC) defines biodegradation as the “degradation caused by the enzymatic process resulting from the action of cells,”^[69] in most of the literature, both environmentally and biologically acceptable degradations are generally referred to as biodegradation.^[10] In principle, only NPs with $HD \leq 6$ nm could be directly excreted via the kidney and urine pathway. These quickly cleared NPs may be used in some bioimaging applications, but are unsuitable for drug delivery and therapy due to the necessity of sufficient retention time in vivo. In addition, for efficient loading of drugs, genes and/or proteins, the sizes of the constructed NP-based nanosystems are usually well above 8 nm. Thus, efficient in vivo biodegradation is necessary for NPs with a size larger than that of the excretion threshold. Moreover, NPs have to be degraded into small ($HD \leq 6$ nm) nontoxic components for efficient excretion. Currently, most of the approved nanosystems in human clinical trials are biodegradable NPs, as well as renal-clearable NPs, such as liposomes, polymers, micelles, lipids, albumin, Fe_3O_4 NPs, and C-Dots.^[52–60] In contrast, nondegradable nanomaterials are raising critical concerns in terms of their biosafety owing to their uncontrollable bioaccumulation in vivo. Generally, the absence of biodegradability restricts the approval of U.S. FDA and other regulatory agencies. Therefore, suitable surface functionalizations and intrinsic biodegradation properties of NPs ($HD \geq 8$ nm) are prerequisites for sufficient blood circulation time, tumor targeting, and efficient in vivo clearance.

1.3. Biodegradation and In Vivo Clearance of Mesoporous Silica Nanoparticles

Thus far, much effort has been devoted to the study of biosafety and the in vivo fate of silica-based nanomaterials such as MSNs, mesoporous organosilica NPs (MONs), their derivatives, and constructed nanosystems based on these as platforms. There are still conflicting conclusions about the biosafety of silica-based nanomaterials, although a lot of research results indicated their low cytotoxicity and in vivo toxicity under relatively high dosage.^[32–37] In addition, detailed knowledge about their in vivo biosafety is still insufficient and unclear, and their ultimate fate in vivo has not yet been fully substantiated due to the complex in vivo environment and high-resolution bioimaging technological obstacles. Based on the abovementioned key principles for the design of nanotheranostics to cross biological barriers, the sizes of MSNs should be controlled below 100 nm, which can be relatively easily achieved, but it remains difficult to synthesize MSNs with discoidal shape. The surface of MSNs can be modified with various functional groups (e.g., PEG or zwitterionic ligands); however, there are only a few reports about responsive charge switch based on MSNs as a platform. The MSNs have a rigid framework built of an $-Si-O-Si-$ network.

In contrast, it was recently discovered that the introduction of organic moieties in the framework walls of hollow MSNs with a thin shell could endow the particles with slight deformability (soft) property, which could improve cellular uptake.^[70,71] MSNs possess a relatively stable structure compared with polymers, but the framework stability can thus still be regulated by introducing suitable species in the framework.

The stability/degradation of silica materials is of high significance toward in vivo clearance, further determining biosafety and in vivo fate. Currently, real-time in vivo imaging observation, inductively coupled plasma optical emission spectrometry (ICP-OES) analysis, and transmission electron microscopy (TEM) observation are the main tools to detect the degradation situation. However, it is still a great challenge to achieve real-time monitoring of the in vivo dynamic degradation profiles, and accurate determination of complete degradation and clearance dynamics.^[72] Silica is usually regarded as a rigid material due to the stable framework of $-\text{Si}-\text{O}-\text{Si}-$ network. However, silica can slowly degrade in aqueous media because $-\text{Si}-\text{O}-\text{Si}-$ bonds slowly hydrolyze into two $-\text{Si}-\text{OH}$ units, and their degradation behaviors appear to be complex, depending on many factors, such as framework condensation degree (i.e., $-\text{Si}-\text{O}-\text{Si}-$ and $-\text{Si}-\text{OH}$ contents), particle size and concentration, specific surface area, pore size and texture, aggregation degree among MSNs, functionalization groups, and the presence of organic/inorganic species into the silica framework, solution type, temperature, etc.;^[9–13,73–79] He et al. reported a three-stage degradation behavior of surfactant-extracted MCM-41-type MSNs in simulated body fluid (SBF), including 1) a fast degradation stage on an hour scale 1), 2) then a decelerated degradation stage due to the formation of calcium/magnesium silicate layer on the MSNs surface 2), and 3) finally, a maintained slow diffusion stage on a dayscale 3), with a nearly complete degradation after a 15 day immersion at the particle concentration of 0.5 mg mL^{-1} .^[56] Calcined MSNs were found to be more resistant to degradation in physiological media compared with template-extracted ones. Lindén and co-workers showed that specific surface area was the main parameter of controlling silica dissolution rates of different MSNs studied.^[75] Quignard et al. reported a significant decrease in the size of fluorescent nonporous fluorescein isothiocyanate (FITC)- SiO_2 NPs located in endocytic vesicles after 14 days, on the basis of TEM observation, and the dissolution process was proved by both the detected colloidal and soluble silica species in the cell culture medium.^[77] Several research groups found that PEG-modified MSNs exhibited a slower degradation rate than their unmodified counterparts.^[78,79] In addition, compared with MSNs with $-\text{Si}-\text{O}-\text{Si}-$ siloxane frameworks, porous silicon with crystalline network usually shows more rapid dissolution into silicic acid by successive hydrolysis reactions, and is regarded as being biodegradable in vivo.^[10,80–82] In particular, the excellent biodegradation and biocompatibility of luminescent porous silicon NPs have boosted many applications for cargo delivery and near-infrared fluorescent bioimaging, and even resulted in promising results in preclinical tests.^[80–82] However, generally, the hydrolysis reaction in aqueous environments occurs randomly at any time, thus leading to a “passive” uncontrolled degradation, which is not the most desirable for in vivo application.

The in vivo stability/degradation of silica-based materials was also investigated, combined with critical pharmacological parameters, such as blood circulation and clearance half-life, biodistribution, and excretion. For example, the abovementioned famous multimodal C-Dots were very stable and reported to have blood (5.9 h), liver (65.9 h), spleen (42.3 h), kidneys (66 h), and tumor (73.5 h) clearance half-life ($t_{1/2}$) values, respectively.^[38] Nearly half and about 72% was excreted within the first 24 and 96 h, respectively, and no significant NPs were detected in urine after 7 days. Importantly, the excreted dots were found to be intact in the urine and without release of the encapsulated dye. These results show that their property of small size (HD of ^{124}I -cRGDY-PEGylated NPs was $\approx 7 \text{ nm}$), the PEGylation and the nondegradation character are in favor of their excellent biosafety, thus entering a first-in-human clinical trial. Most of MSNs and MSN-based nanosystems with HD $\geq 8 \text{ nm}$ are resistant to degradation in vivo and are retained for a relatively long term.^[83–89] Shi and co-workers investigated the effects of particle sizes (80, 120, 200, and 360 nm) and PEGylation of spherical MSNs toward urinary excretion by tail-vein injection in Institute of Cancer Research (ICR) mice,^[84] and found that the PEGylated MSNs (PEG-MSNs) with smaller particle size demonstrated longer blood circulation lifetime, escaped more easily from capture by liver, spleen, and lung tissues; had slower degradation rates; and correspondingly, showed a lower excreted amount of degraded products in the urine (Figure 1). In this case, MSNs and PEG-MSNs were still detected in the liver and spleen after 1 month of injection.^[84] These studies revealed that silica NPs with larger than 100 nm size could be rapidly excreted through renal and hepatic routes in the urines and feces containing either intact MSNs or partially degraded products. However, the excretion mechanism is still unclear and needs to be studied further.

In vivo biodegradation of silica-based materials also has a significant effect on tolerance threshold and thus dosage.^[90–93] In their early research work, Tang and co-workers systematically investigated single and repeated dose toxicity, and clearance of rattle-type hollow MSNs (HMSNs, particle size: 110 nm) without any modification in ICR mice.^[90] It was found that lethal dose 50 (LD_{50}) of HMSNs was higher than 1000 mg kg^{-1} for single dose toxicity, while further repeated dose toxicity studies indicated no death when mice were injected with HMSNs at 20, 40, and 80 mg kg^{-1} by continuous intravenous administration over 14 days. In addition, these HMSNs mainly accumulated in mononuclear phagocytic cells in liver and spleen, and their entire clearance time required more than 4 weeks. They also discovered that continuous intraperitoneal injection of these HMSNs increased liver injury markers in serum, and induced silicotic nodular-like lesions in liver with a dose-dependent manner.^[91] The possible mechanism was ascribed to the KC-initiated lesions. Specifically, HMSNs were taken up by KCs, and caused cell damage and death, and then HMSNs were liberated from the dead cells and subsequently taken up by other KCs. This recurring cycle of macrophage phagocytosis perpetuated the inflammatory process and ultimately resulted in silicotic nodule lesions.^[91]

Overall, the nondegradation behavior of small silica NPs ($\leq 6 \text{ nm}$) may be better than noncontrollable degradation for in vivo bioimaging applications owing to their facilitated excretion.

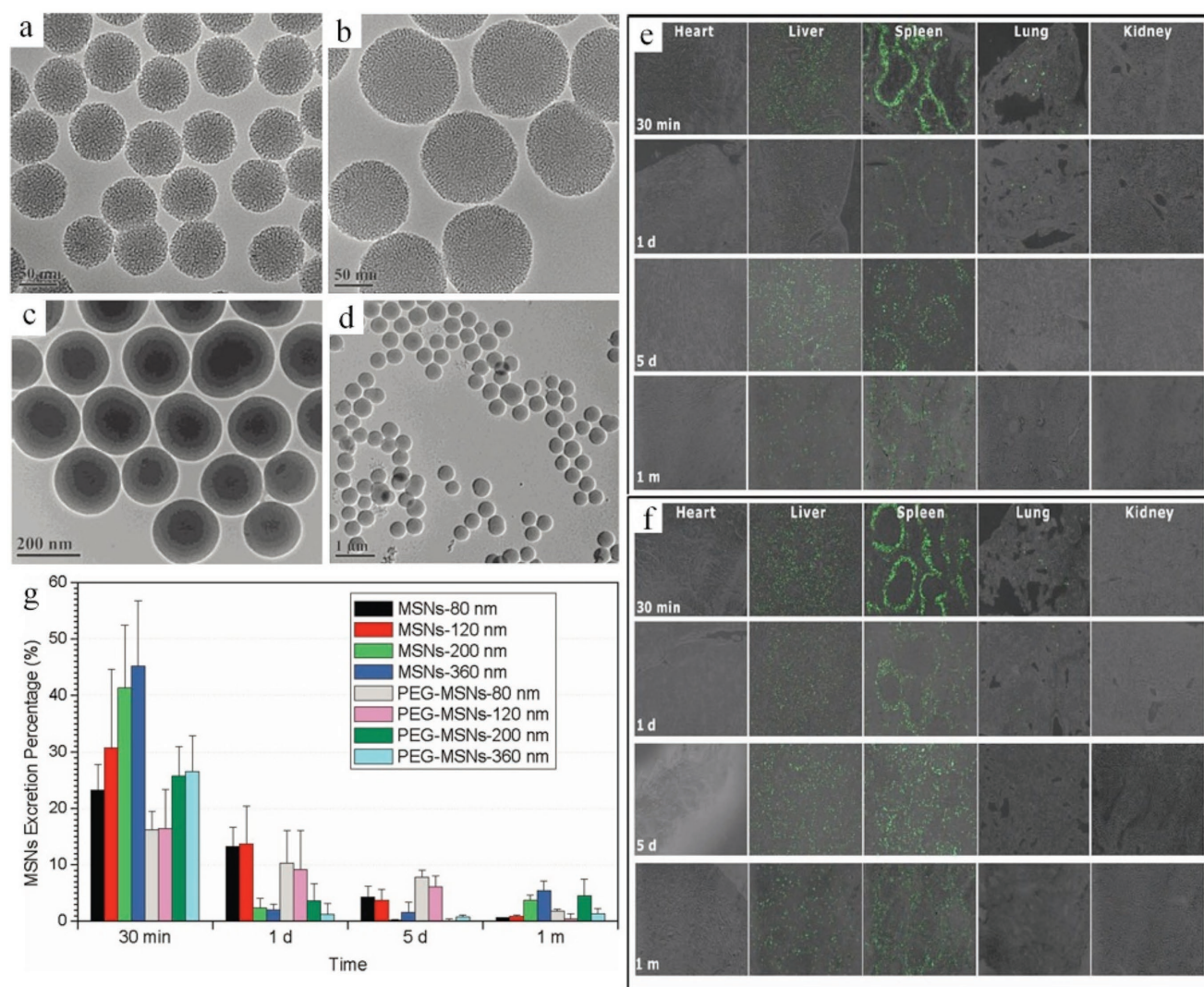


Figure 1. TEM images of PEG-MSNs with different particle sizes: a) PEG-MSNs-80 nm, b) PEG-MSNs-120 nm, c) PEG-MSNs-200 nm, and d) PEG-MSNs-360 nm. Fluorescence images of heart, liver, spleen, lung, and kidney tissue slices from ICR mice injected with e) MSNs-80 nm and f) PEG-MSNs-80 nm. g) Excretion percentages of the degradation products of MSNs and PEG-MSNs of different particle sizes (80, 120, 200, and 360 nm) in urine of ICR mice up to 1 month after tail intravenous injection. Reproduced with permission.^[84] Copyright 2011, Wiley-VCH.

However, for larger sizes of nondegradable silica-based nanomaterials, severe and/or long-term accumulations (complete clearance from the body needs a period of several days to a few months) in organs may induce biliary excretion and glomerular filtration dysfunction, and raise concerns of in vivo toxicity and organ diseases, such as silicosis. Possibly, a stimuli-triggered degradation into nontoxic and small species (≤ 6 nm) may be a potential solution for efficient in vivo clearance.^[94] In addition, the exact compositions and biosafety of the degraded products of MSNs with or without various functionalizations should also be systematically investigated. It was demonstrated that silica materials can be degraded into silica fragments and silicic acids including monomeric silicic acid and/or different polysilicic acids with varied polymerization degrees under physiological conditions.^[9–11] Previous reports showed that monomeric silicic acid could not bind to enzymes and proteins, thus could induce no cytotoxicity. On the other hand, the cytotoxicity of dimeric and trimeric silicic

acids has not yet been fully elucidated, while high content of polysilicic acids would cause certain cytotoxicity by adsorbing and binding enzymes and proteins.^[74,95,96] In the case of mesoporous materials, Shi and co-workers reported that the biodegraded products of the extracted MSNs (particle size: 420 nm; without any modification) had no toxicity to both COS-7 cells and MDA-MB-468 cells over a broad concentration range of biodegraded products from ≈ 26 to $76 \mu\text{g mL}^{-1}$.^[74] In conclusion, in vivo biodegradation of silica-based nanosystems may solve the problem of long-term retention; however, the biosafety of their resulting biodegraded products then becomes another major concern.

1.4. Intracellular Reductive Microenvironment

Compared to the chemically inert properties and the “passive” uncontrolled slow hydrolysis of pure silica materials, a precise

control over the degradation of silica-based NPs is highly necessary and desirable. Efforts have thus been devoted to develop stimuli-triggered degradable theranostic nanosystems that can recognize specific microenvironments.^[9–13] To achieve tumor microenvironment (pH, redox, enzyme, etc.)-triggered biodegradation of silica-based materials, scientists regulated the structural stability of the silica framework by introducing various organic/inorganic moieties into the framework walls, such as methylene ($-\text{CH}_2-$), ethylene ($-\text{CH}_2-\text{CH}_2-$), ethynylene ($-\text{CH}=\text{CH}-$), phenylene ($-\text{C}_6\text{H}_4-$), bis(propyl)disulfide (thioether) ($-(\text{CH}_2)_3-\text{S}-\text{S}-(\text{CH}_2)_3-$), bis(propyl)tetrasulfide (thioether) ($-(\text{CH}_2)_3-\text{S}-\text{S}-\text{S}-\text{S}-(\text{CH}_2)_3-$), and metal cations (e.g., Ca, Fe, Mn, Al, and Zr).^[9–13] Note that MONs with these organo-bridged silsesquioxane frameworks are abbreviated to “methane-, ethane-, ethene-, benzene, or disulfide-bridged MONs, for convenience. Among the different functions, the disulfide bond is relatively stable in a mild oxidizing

environment (e.g., oxygen gas and blood stream) and under physiological pH conditions; however, it is sensitive to the disulfide–thiol exchange reaction. Thus, the integration of the cleavable disulfide bond in the framework was seen as a promising way to realize intracellular redox-responsive biodegradation along with the release of the loaded cargos (**Figure 2**).^[97–102] The redox potential results from the huge concentration difference of glutathione (GSH, a tripeptide containing a reducing thiol) between intracellular ($\approx(2-10) \times 10^{-3} \text{ M}$) and extracellular ($\approx(2-20) \times 10^{-6} \text{ M}$) microenvironments.^[97–102] More importantly, the GSH concentration in a few cancer cells was observed to be several times higher than that in normal cells,^[103] which may be used for specific cancer treatment. GSH/oxidized GSH (glutathione disulfide, GSSG), which is a major redox couple in animal cells, determines the antioxidative capacity. Generally, once GSH is oxidized, the intracellular GSH reductase/thioredoxin can reduce it back to maintain high intracellular

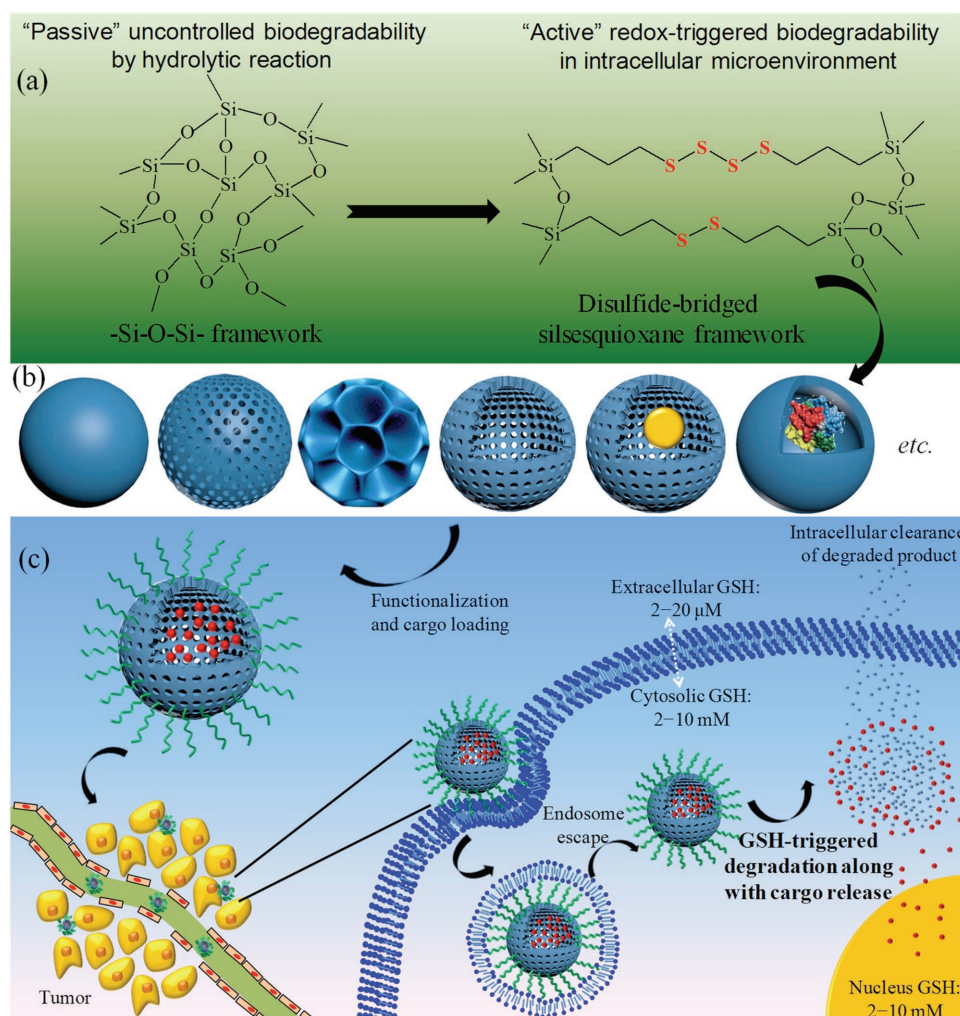


Figure 2. a) Possible molecular structure of disulfide-bridged silsesquioxane framework, which may show “active” redox-triggered biodegradability in intracellular microenvironment of cancer cells compared with “passive” uncontrolled biodegradability of pure $-\text{Si}-\text{O}-\text{Si}-$ framework by hydrolytic reaction. Schematic illustration of b) synthesized hybrid NPs with disulfide-bridged silsesquioxane framework, but with different sulfur (S) contents and structures including solid, mesopores, center-radial pores, hollow, yolk-shell, and core-shell, and c) further functionalization and cargo loading, blood transport, tumor accumulation, cellular uptake, GSH-triggered degradation along with cargo release, and the intracellular clearance of degraded product for improved anticancer drug delivery and efficient in vivo clearance.

GSH concentration.^[97–102] In healthy animal cells and tissues, over 90% of the total GSH/GSSG pool is under the form of reductive GSH. In addition, it should be pointed out that endosomal and lysosomal compartments are also redox active due to the presence of gamma interferon-inducible lysosomal thiol reductase and cysteine in endosomes, and Fe²⁺ and cysteine in lysosomes.^[104,105] Therefore, GSH has been regarded as a promising intracellular stimulus in living cells, especially cancer cells, to realize intracellular responsive degradation, drug release, bioimaging, and detection.^[97–102] Since the disulfide bond was introduced into drugs, polymers, and micelles, it has been extensively applied to construct various nanotheranostic systems based on various components,^[97–102] which are stable in the blood circulation and tumor tissues, but show intracellular responsive cleavage properties after entering into tumor cells. For silica-based nanosystems, the early studies mainly focused on the design and synthesis of pore blockers on the particle surface and drug linkage on the pore walls by using the disulfide bond as a responsive linker.^[99]

The introduction of disulfide bond in the silica framework has become a subject of great interest because the high intracellular GSH concentration can trigger the redox breakage of the –S–S– bond in disulfide-bridged silsesquioxane framework, which can further accelerate the hydrolysis of –Si–O–Si– bonds within the silica framework, thus achieving the fast biodegradation of hybrid NPs along with GSH-triggered release of the loaded cargos (Figure 2). Most importantly, it may solve the problem of uncontrollable and difficult biodegradation of the silica-based nanomaterials with HD ≥ 8 nm. Once nanosystems with a disulfide-bridged silsesquioxane framework were taken up by tumor cells via passive or active targeting, the disulfide bonds in the silica matrix may be reduced by intracellular GSH, enabling triggered biodegradation of the nanocarriers into fragmented residues for rapid clearance. In spite of the significance for promising applications in vivo, only a few reviews focused on the tailored synthesis and redox-triggered intracellular biodegradability of silica-based nanomaterials with a disulfide-bridged silsesquioxane framework.^[10–12] Therefore, the present review article aims to provide a summary of the recent research progress on this topic, and it is organized as follows: design synthesis of hybrid nanomaterials with disulfide-bridged silsesquioxane framework, redox-triggered degradability and cargo release, biocompatibility, and nanobiomedical applications.

2. Controlled Synthesis of Hybrid Nanomaterials with Disulfide-Bridged Silsesquioxane Frameworks

The formation of a disulfide-bridged silsesquioxane framework is generally achieved by co-condensation of tetraethoxysilane (TEOS)/tetramethoxysilane (TMOS) and one or more bis- or multibridged organosilica precursor(s) containing disulfide bonds (Figure 3), based on sol–gel-type chemistry. Up to now, commercially available bridged silanes containing disulfide bonds were only of two kinds: 1) bis(triethoxysilyl propyl) disulfide (BTEPDS, (H₅C₂O)₃Si–(CH₂)₃–S–S–(CH₂)₃–Si(OC₂H₅)₃) or bis(trimethoxysilyl propyl) disulfide (BTMPDS,

(H₃CO)₃Si–(CH₂)₃–S–S–(CH₂)₃–Si(OC₂H₅)₃) and 2) bis(3-triethoxysilyl propyl) tetrasulfide (BTEPTS, (H₅C₂O)₃Si–(CH₂)₃–S–S–S–S–(CH₂)₃–Si(OC₂H₅)₃) (Figure 3a,b). Other bridged silanes containing disulfide bonds are synthesized by smart molecular design, as shown in Figure 3c–h.^[106–111] In the case of MONs with the different bridged groups of “–(CH₂)₃–S₂–(CH₂)₃–”, “–(CH₂)₃–S₄–(CH₂)₃–”, or other groups with disulfide bond in Figure 3, we abbreviate them into disulfide-bridged MONs. Due to the existence of a relatively hydrophobic –(CH₂)₃–S₄ (or S₂)–(CH₂)₃– chain, BTEPTS (or BTEPDS), exhibiting light yellow color, has slightly slower hydrolysis and condensation rates compared to TEOS, and this will, to a certain degree, affect the cooperative self-assembly process with the structure-directing agent. Generally, TEOS and disulfide-bridged organosilane should be premixed before addition into the reaction medium. Since the first inclusion of disulfide bonds into the framework of mesoporous silicas in 2003,^[112] scientists have successfully synthesized various organosilica materials or nanocomposites comprising a disulfide-bridged silsesquioxane framework, with different sulfur (S) contents and a variety of possible morphologies, which include irregular and regular systems, e.g., solid/nonporous, mesoporous, center-radial pores, and hollow, yolk–shell, core–shell structures. For the characterization of disulfide bond, Raman spectroscopy is a sensitive tool used to detect –S–S–. ICP-OES can assess S content, and energy dispersive X-ray (EDX) element mapping can reveal the S distribution in the materials.

2.1. Disulfide-Bridged Mesoporous Organosilicas with Irregular Particle Morphologies

The formation of mesopores is mainly achieved by employing triblock copolymer poly(ethylene oxide)₂₀–poly(propylene oxide)₇₀–poly(ethylene oxide)₂₀ (EO₂₀PO₇₀EO₂₀, P123, *M_n* = 5800)^[112–121] or the cationic surfactant cetyltrimethylammonium bromide (CTAB)/cetyltriethylammonium bromide (CTEAB)^[122,123] as templates, as compiled in Table 1. For the P123 template, Zhang et al. reported the first synthesis of ordered mesoporous organic–inorganic composites with disulfide-bridged organosilica framework by one-step co-condensation of BTEPTS and TEOS, in order to generate materials for Hg²⁺ adsorption with high selectivity and capacity.^[112] By regulating the BTEPTS content from 0 to 15 at%, the S content increased from 0 to 14.1 wt%; however, at high BTEPTS content, the mesopore order suffered from some disturbance, the pore diameter decreased, and the pore size distribution became wider. Mehdi and co-workers synthesized mesoporous organosilica materials with disulfide-bridged organosilica framework and aminopropyl-modified pore walls via one-pot sequential co-condensation reaction of TEOS/BTMPDS/3-tertbutyloxycarbonyl (aminopropyl) trimethoxysilane (TBCATMS) = 10:1:1.^[113] Nevertheless, instead of *p6mm* ordered mesopores, disordered wormlike mesopores were formed due to introduction of the organosilanes. In order to obtain ordered mesopores, the authors designed and synthesized a bis-silylated precursor containing a more hydrophilic disulfide unit (Figure 3d) than BTMPDS

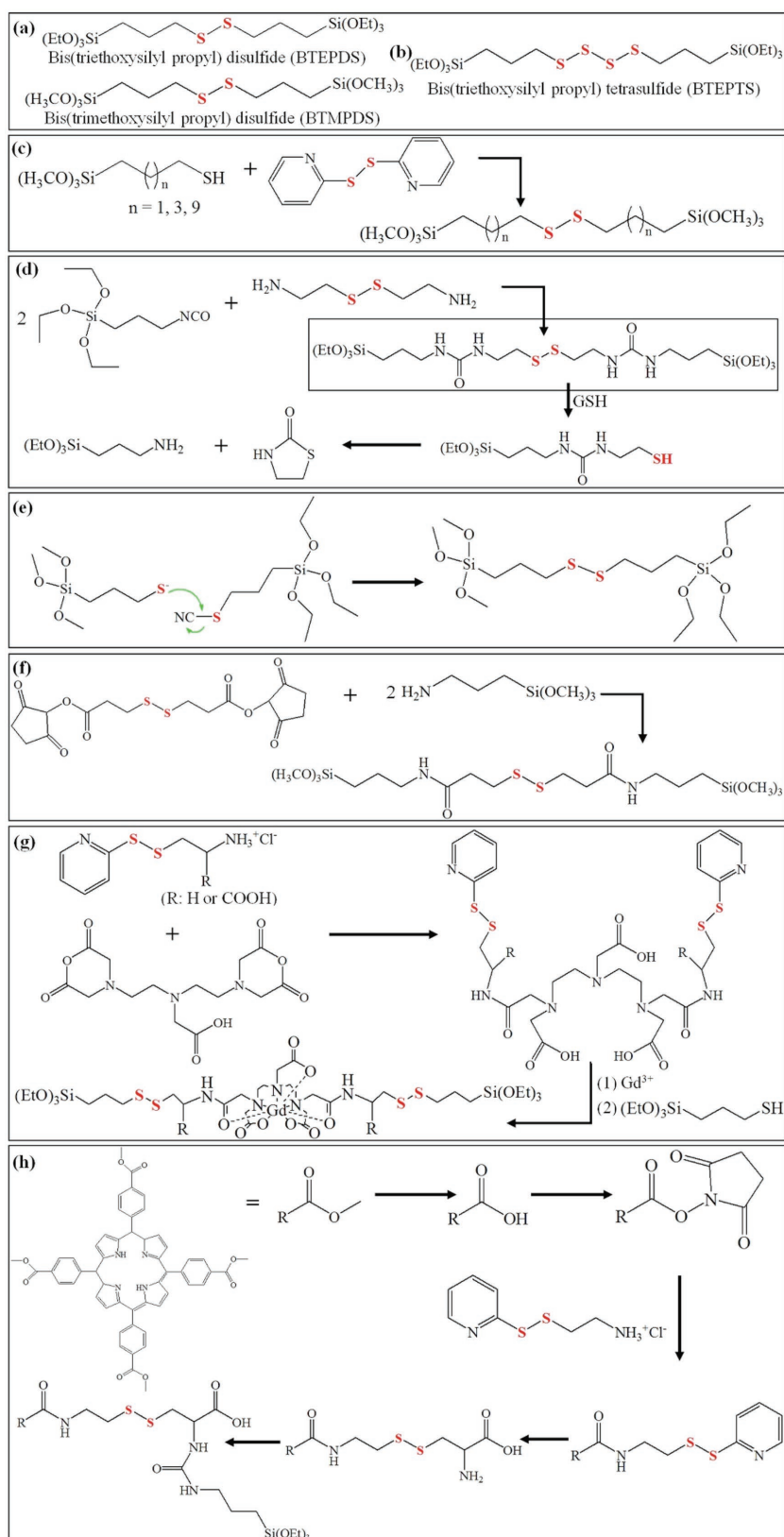


Figure 3. Molecular formulae of bridged silanes containing disulfide bond: a,b) commercially available and c–h) smartly designed.^[106–111]

with $-(\text{CH}_2)_3-\text{S}-\text{S}-(\text{CH}_2)_3-$ group, and achieved the synthesis of disulfide-bridged organosilica materials with a well-structured 2D hexagonal mesopore under a wide range of molar ratios of TEOS/bridged silane from 30:1 to 10:1.^[114] Liu et al. observed mesophase transformations from a highly ordered 2D hexagonal structure, then to a vesicle-like structure, and finally to a mesostructured cellular foam by varying the molar ratio of BTEPTS/TMOS from 1/38 to 1/3 during the synthesis of disulfide-bridged mesoporous organosilicas.^[115,116] Hao et al. found that the addition of Zn^{2+} facilitated well-ordered hexagonal ($p6mm$) mesoporous organosilicas with a high content of bridged disulfide bonds via tuning the BTEPTS/TEOS molar ratio from 5% to 20%.^[117] However, a ratio over 20 at% resulted in the complete collapse of the ordered mesostructure.

By using CTAB as a template, Liu et al. synthesized disulfide-bridged mesoporous organosilica materials with a wide range of molar ratios of BTEPTS/TMOS up to 1/3.^[122] The BTEPTS/TMOS molar ratios in the range of 1/8–1/3 resulted in structural defects (i.e., holes) in the walls of the mesochannels, and the highest S content was up to 20.3 wt%. Chiu et al. reported the synthesis of well-ordered cubic ($Pm\bar{3}n$) mesoporous organosilicas with a high loading of disulfide groups using the regulation of the BTEPDS/TEOS molar ratio from 1/9 to 8/2 under acidic conditions using CTEAB as a template.^[123] Ordered and uniform mesopores were maintained up to 50 mol% of BTEPDS/TEOS, while the cubic mesostructure completely collapsed when this ratio was over 60 mol%.

To summarize, generally, the increase of disulfide-bridged organosilane content in the initial premixed silanes results in the increase of disulfide-bridged silsesquioxane content in the framework; however, it also caused a decrease of the pore size, pore volume, specific surface area, and mesopore ordering.^[112–123] The structural change is attributed to the fact that the high content of disulfide-bridged organosilane with a hydrophobic chain interacts with the hydrophobic part of the surfactant template, thus interfering with their cooperative self-assembly and condensation. In addition, the incorporation of the relatively long $-(\text{CH}_2)_3-\text{S}_2-$ (or S_4)- $(\text{CH}_2)_3-$ group in the mesoporous framework usually led to enhanced hydrothermal stability, as checked in boiling water for several days, owing to its hydrophobic character.^[119,122]

Table 1. Disulfide-bridged mesoporous organosilicas with irregular bulk morphologies. (“–” means “not provided data” in the reported references.)

| Silica source | Template | pH condition | Pore size [nm] | Brunauer–Emmett–Teller surface area [m ² g ^{−1}] | Pore volume [m ³ g ^{−1}] | Pore structure | S content [wt%] | Ref. |
|----------------------------------|--------------------------|---|----------------|---|---|-----------------------|-----------------|-----------|
| 98 at% TEOS, 2 at% BTEPTS | P123 | HCl | 5.02 | 634 | – | <i>p6mm</i> | 4.80 | [112] |
| 94 at% TEOS, 6 at% BTEPTS | | | 3.74 | 654 | – | | 9.06 | |
| 92 at% TEOS, 8 at% BTEPTS | | | 3.47 | 576 | – | | 11.1 | |
| 90 at% TEOS, 10 at% BTEPTS | | | 3.35 | 532 | – | | 12.0 | |
| 88 at% TEOS, 12 at% BTEPTS | | | 3.26 | 253 | – | | 12.9 | |
| 85 at% TEOS, 15 at% BTEPTS | | | 3.13 | 242 | – | | 14.1 | |
| TEOS/BTMDPS/TBCATMS = 10:1:1 | P123 | HCl | 8.9 | 562 | 1.06 | Wormlike | 5.8 | [113] |
| TEOS/silane in Figure 3d = 30/1 | P123 | HCl | 5.9 | 593 | 0.88 | <i>p6mm</i> | Si/S:39/1 | [114] |
| TEOS/silane in Figure 3d = 20/1 | | | 5.4 | 549 | 0.75 | <i>p6mm</i> | Si/S:25/1 | |
| TEOS/silane in Figure 3d = 10/1 | | | 5.3 | 357 | 0.48 | <i>p6mm</i> | Si/S:13/1 | |
| BTEPTS/TEOS = 1/38 (molar ratio) | P123 | CH ₃ COOH, CH ₃ COONa | 8.0 | 854 | 1.00 | <i>p6mm</i> , Vesicle | – | [115,116] |
| BTEPTS/TEOS = 1/18 (molar ratio) | | | 7.4 | 764 | 1.07 | <i>p6mm</i> , Vesicle | – | |
| BTEPTS/TEOS = 1/8 (molar ratio) | | | 7.1 | 413 | 0.93 | <i>p6mm</i> , Vesicle | – | |
| BTEPTS/TEOS = 3/14 (molar ratio) | | | 8.0, 20.5 | 485 | 1.02 | Vesicle, foam | – | |
| BTEPTS/TEOS = 1/3 (molar ratio) | | | 7.3, 20.6 | 303 | 0.79 | Vesicle, foam | – | |
| 5 at% BTEPTS, 95 at% TEOS | P123 (Zn ²⁺) | HCl | 6.3 | 580 | 0.69 | <i>p6mm</i> | 4.0 | [117] |
| 10 at% BTEPTS, 90 at% TEOS | | | 5.6 | 341 | 0.39 | <i>p6mm</i> | 6.5 | |
| 15 at% BTEPTS, 85 at% TEOS | | | 4.0 | 382 | 0.40 | <i>p6mm</i> | 8.7 | |
| 20 at% BTEPTS, 80 at% TEOS | | | 3.5 | 472 | 0.40 | <i>p6mm</i> | 10.8 | |
| BTEPTS/TEOS = 1/18 (molar ratio) | CTAB | NaOH | 2.75 | 979 | 0.69 | <i>p6mm</i> | 6.75 | [122] |
| BTEPTS/TEOS = 1/8 (molar ratio) | | | 2.82 | 846 | 0.63 | <i>p6mm</i> | 9.38 | |
| BTEPTS/TEOS = 3/14 (molar ratio) | | | 2.70 | 711 | 0.55 | Wormlike | 15.0 | |
| BTEPTS/TEOS = 1/3 (molar ratio) | | | 2.09 | 597 | 0.40 | Wormlike | 18.2 | |
| BTEPTS/TEOS = 1/2 (molar ratio) | | | 2.10 | 453 | 0.29 | Wormlike | 20.3 | |
| BTEPDS/TEOS = 1/9 (molar ratio) | CTEAB | H ₂ SO ₄ | 4.4 | 1107 | 0.61 | <i>Pm3n</i> | 9.3 | [123] |
| BTEPDS/TEOS = 3/7 (molar ratio) | | | 4.0 | 859 | 0.47 | | 14.1 | |
| BTEPDS/TEOS = 1/1 (molar ratio) | | | 3.2 | 325 | 0.19 | | 17.5 | |
| BTEPDS/TEOS = 7/3 (molar ratio) | | | 2.7 | 140 | 0.10 | | 22.5 | |

2.2. Disulfide-Bridged Organosilicas with Well-Defined Structures

As shown in **Table 2**, various disulfide-bridged organosilicas with well-defined structures and S contents have been successfully prepared by exploring the details of the synthesis systems and carefully controlling experimental parameters.

2.2.1. Nonporous (Solid) Nanoparticles

Kim et al. prepared monodisperse disulfide-bridged organosilica spheres with a diameter size of ≈350 nm by using BTEPTS as the sole silane in NH₃·H₂O–ethanol–water system at room temperature (**Figure 4A**).^[124] Quignard et al. synthesized disulfide-bridged NPs with dye introduced by an unusual sequential addition into an ammonia–ethanol solution:

first TEOS, then BTEPDS, and finally FITC-grafted 3-aminopropyltriethoxysilane (APTES). Noticeably, higher amount of BTEPDS addition resulted in inhomogeneous products.^[125] Xu et al. reported the synthesis of disulfide-bridged organosilica NPs with sizes in the range of 50–200 nm in NH₃·H₂O–ethanol–water system by co-condensation of TEOS and the silane shown in **Figure 3d**.^[107] Hsu and co-workers synthesized NPs with a combined bis(propylamide-ethyl)disulfide-bridged and aminopropyl-modified organosilica scaffold in the NH₃·H₂O–ethanol–water system by co-condensation of 3-aminopropyltrimethoxysilane (APTMS) and the silane in **Figure 3f** at room temperature (**Figure 4B**). The S/Si molar ratio increased from the particle surface (1/8.7) to the core (1/2).^[109] Croissant et al. prepared disulfide-bridged nanospheres containing two-photon electron donor (2PS) and porphyrin (POR) groups in CTAB–NaOH–water system at 80 °C for two photon-excited (TPE) imaging and therapy (**Figure 4C**).^[126] Both the

Table 2. Disulfide-bridged organosilicas with regular morphologies. ("–" means "not provided data" in the reported references.)

| Silica source | Template | Product structure | Particle size [nm] | Pore size [nm] | Brunauer-Emmett-Teller surface area [m ² g ^{−1}] | Pore structure | S content [wt%] | Ref. |
|--------------------------------|----------------------------|--------------------------------------|--------------------|----------------|---|----------------------|-----------------|-----------|
| BTEPTS | Non | Solid NPs | 350 | Non | – | Non | – | [124] |
| BTEPTS, C ₁₈ TMS | Non | MONs | 150 | – | – | Wormlike | – | |
| BTEPTS | CTAB | MONs | 150 | – | – | Wormlike | – | |
| BTEPDS/TEOS = 1/10 | Non | Solid NPs | ≈40 | – | – | – | 2.6 | [125] |
| BTEPDS/TEOS = 2/10 | | | ≈40 | – | – | – | 3.5 | |
| BTEPDS/TEOS = 3/10 | | | ≈40 | – | – | – | 4.8 | |
| BTEPDS/TEOS = 4/10 | | | ≈40 | – | – | – | 6.5 | |
| TEOS, silane in Figure 3d | Non | Solid NPs | Tunable in 50–200 | Non | – | Non | – | [107] |
| APTMS, silane in Figure 3f | Non | Solid NPs | 143 ± 38 | Non | – | Non | – | [109] |
| BTEPDS | CTAB | Solid NPs | 30 | – | – | – | – | [126] |
| BTEPDS, silane with 2PS | | Solid NPs | 40 | – | – | – | – | |
| BTEPDS, silane with POR | | Solid NPs | 50 or 200 | – | – | – | – | |
| Silane in Figure 3g | Non | Solid NPs | 100–150 | Non | – | Non | – | [110] |
| Silane in Figure 3h | Water-in-oil microemulsion | Solid NPs | 144 ± 15 | Non | – | Non | – | [111] |
| BTEPDS | CTAB | Solid NPs | 200 ± 15 | Non | – | Non | 1.84 | [127] |
| BTEPDS | CTAB | Solid NPs | 120 or 330 | Non | – | Non | – | [128] |
| BTEPTS/TEOS = 0.179 | CTAB | MONs | Tunable in 90–290 | 2.0 | – | Wormlike | – | [129] |
| BTEPDS/TEOS = 3:7 | CTAB | MONs | 88.9 ± 10.9 | 2.2 | 161 | Wormlike | – | [132] |
| BTEPDS/TEOS = 1:4.8 | CTAB | MONs | 60 | 1.7 | 614 | Wormlike | – | [128] |
| | | | 110 | 2 | 366 | Wormlike | | |
| BTEPTS/TEOS = 1/6.6 | | | 110 | 2.7 | 808 | Wormlike | – | |
| BTEPDS/BTEPTS, TEOS | CTAC, TIPB | MONs | Tunable in 30–200 | 2.8–4.5 | 290–1040 | Wormlike | – | [133] |
| BTEPTS (1.3 g) TEOS (1 g) | CTAC | MONs | 30 | 6.2 | 614 | Radial pore | – | [134] |
| TEOS (1 mL) BTEPDS (0.2 mL) | CTAC | MONs | Tunable in 20–40 | 1.8 | 480 | Wormlike | – | [136] |
| BTEPDS/TEOS = 1:5 | CTAC | MONs | 20 | 1.8 | – | Wormlike | – | |
| BTEPDS/TEOS = 2:5 | | | 20 | 2.0 | – | Wormlike | – | |
| BTEPDS/TEOS = 3:5 | | | 20 | 2.2 | – | Wormlike | – | |
| BTEPDS/TEOS = 4:5 | | | 20 | 3.8 | – | Wormlike | – | |
| BTEPTS (2 g) TEOS (1 g) | CTAC, MSNs | MONs | 70 | 4–9 | 441 | Dual-modal mesopores | – | [138] |
| BTEPTS (0.8 mL) TEOS (1 mL) | CTAB NaSal | MONs | 200 | 14 | 405 | Radial pore | – | [140] |
| BTEPTS:TEOS = 0.179 | CTAB | Yolk-shell MONs | Tunable in 90–290 | 2.0 | 400 | Wormlike | – | [129,143] |
| BTEPTS:TEOS = 0.179 | CTAB | Deformable HMons | 310 | 3.2 | 878 | Wormlike | – | [70] |
| TEOS, BTEE, BTEPTS, BTEB | CTAB | Yolk-shell MONs, dual-shell HMons | 290 | 2.5 | 320 | Wormlike | – | [144,145] |
| BTEPTS, BTEB | CTAB, SiO ₂ NPs | HMons | ≈300 | 3.8 | 1005 | Wormlike | – | [147] |
| TEOS (1 mL) BTEPDS (0.6 mL) | MSNs as core, CTAB | HMons | ≈40 | 4.0 | 515 | Wormlike | – | [148,149] |
| TEOS (1 mL) BTEPDS (1.2 mL) | | HMons | ≈40 | – | – | Wormlike | – | |
| TEOS (1 mL) BTEPDS (1.8 mL) | | HMons | ≈40 | – | – | Wormlike | – | |

Table 2. Continued.

| Silica source | Template | Product structure | Particle size [nm] | Pore size [nm] | Brunauer-Emmett-Teller surface area [m ² g ⁻¹] | Pore structure | S content [wt%] | Ref. |
|---|--------------------------------------|-----------------------|--------------------|----------------|---|----------------|-----------------|-------|
| TEOS (1 mL) BTEPDS (2.4 mL) | | HMONs | ≈40 | – | – | Wormlike | – | |
| BTEPTS | CTAC, SiO ₂ NPs | HMONs | 184 | 3.7 | 293 | Wormlike | – | [152] |
| BTEPTS | 3-aminophenol, formaldehyde | Core-shell | ≈400 | Non | – | Non | – | [153] |
| TEOS (0.9 mL), BTEPTS (0.6 mL) | PAA | HONs | 40–100 | 3.6 | 251 | Disordered | 5.8 | [154] |
| TEOS, APTMS silane in Figure 3d | PS nanospheres | HONs | 200 ± 5 | – | – | Single hole | | [155] |
| BTEEE (0.9 mL) BTEPDS (0.1 mL) | CTAB | Nanorods | 450 × 200 | 2.5 | 458 | <i>p6mm</i> | 0.10 | [127] |
| BTEEE (0.6 mL) BTEPDS (0.2 mL) | | Nanorods | 130 × 70 | 2.0 | 278 | <i>p6mm</i> | 0.55 | |
| BTEEE (0.4 mL) BTEPDS (0.4 mL) | | MONs | 200 ± 50 | 2.0 | 255 | <i>p6mm</i> | 0.95 | |
| TEOS (1 mL), BTEPTS (0.4 mL) | CTAB | Nanorods | 75 × 33 | 2.4 | 570 | Wormlike | – | [156] |
| | | Nanorods | 150 × 48 | 2.6 | 820 | Wormlike | – | |
| | | Nanorods | 310 × 75 | 2.6 | 870 | Wormlike | – | |
| TEOS (0.5 mL) BTEPDS (0.1 mL) | CTAB | Nanorods | 70 × 50 | – | – | Wormlike | – | [136] |
| | | Nanorods | 140 × 60 | – | – | Wormlike | – | |
| | | Nanorods | 200 × 50 | 1.7–2.0 | 450 | Wormlike | – | |
| | | Nanorods | 460 × 50 | – | – | Wormlike | – | |
| BTEEE (0.2 mL) BTEPDS (0.1 mL) | CTAB, benzene-PMO cores | Short multipods | ≈150 | 2.1 | 1506 | <i>p6mm</i> | 0.11 | [157] |
| BTEEE (0.3 mL) BTEPDS (0.1 mL) | | Long multipods | ≈200 | 2.1 | 1433 | <i>p6mm</i> | 0.18 | |
| BTEPDS/TEOS = 2/10 | PLGA and CTAB | Polymer Composites | ≈50–200 | – | – | Non | 0.58 | [158] |
| BTEPDS (0.5 mL) BTEE (0.5 mL) | CS-RhB | Core-shell composites | ≈35 | Non | – | Non | – | [159] |
| MPTMS/TPTES = 1/1 | Oil-in-water microemulsion | Hollow composites | ≈220 | Non | – | Non | – | [108] |
| TEOS (80 μL) BTEPTS (40 μL) | (PAH/PSS) ₄ microcapsules | Hollow composites | ≈2000 | Non | – | Non | – | [160] |
| TEOS (40 μL) BTEPDS (60 μL) | Water-in-oil microemulsion | Protein Composites | 40–50 | Non | – | Non | – | [161] |
| TEOS (0.4 mL) BTEPDS (0.9 mL) | Water-in-oil microemulsion CDs | Core-shell composites | ≈80 | Non | – | Non | – | [162] |
| APTMS (8 × 10 ⁻⁶ M) DTSP (2 × 10 ⁻⁶ M) | Au NPs | Core-shell composites | ≈10 | Non | – | Non | – | [163] |
| TEOS (0.1 mL), BTEPTS (0.01 mL) | PB nanocubes | Core-shell composites | 125 ± 8 | 3.2 | 866 | Wormlike | – | [165] |
| Silane in Figure 3d, TEOS | DOX | Drug Composites | ≈100 | Non | – | Non | – | [166] |

Durand and Ghandehari and co-workers fabricated non-porous disulfide NPs when BTEPDS was used as the sole silane in similar CTAB–NaOH–ethanol–water system, even though CTAB, commonly used as a mesopore template, was included.^[127,128]

Functional diagnostic and/or therapeutic species can be introduced into the framework by two or four disulfide bonds-bridged forms. Lin and co-workers reported the preparation of polysilsesquioxane (PSQ) NPs with high content (14–16 wt%) of paramagnetic Gd(III) centers in a reverse microemulsion

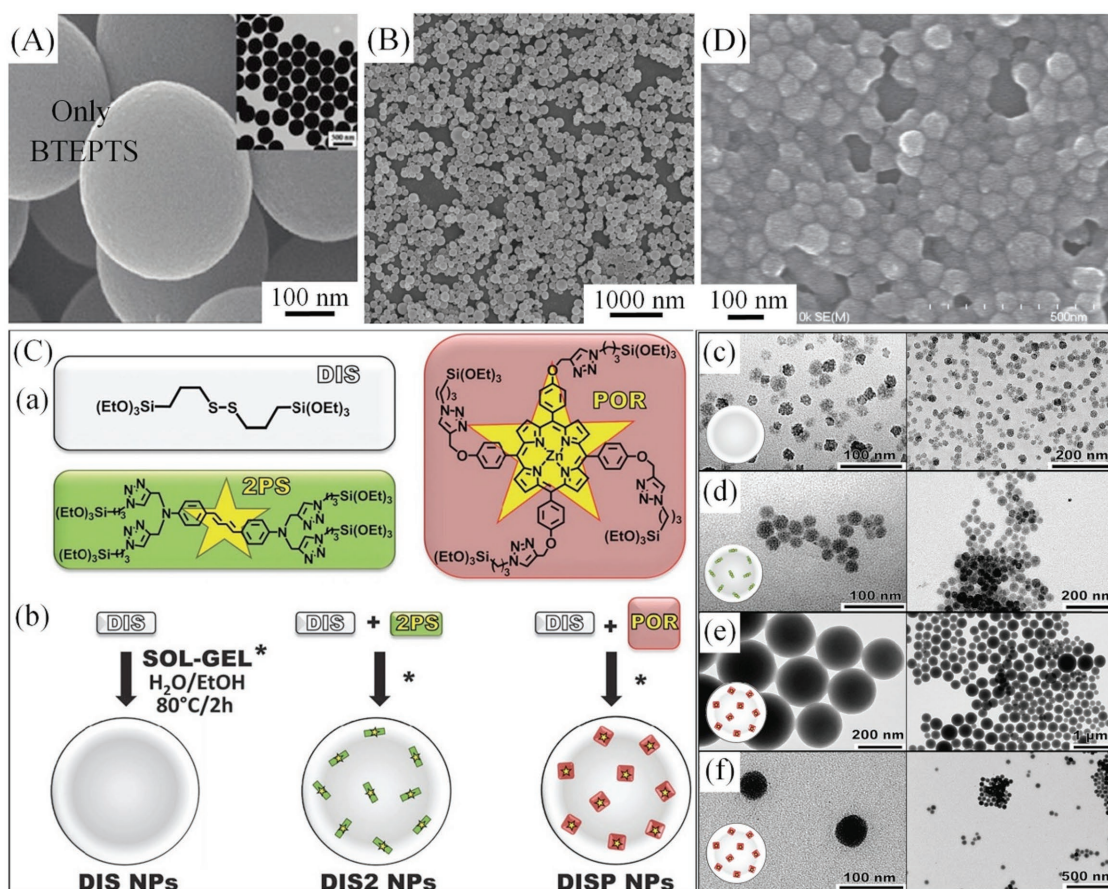


Figure 4. A) SEM and TEM (inset) images of monodisperse as-synthesized disulfide-bridged organosilica spheres. Reproduced with permission.^[124] Copyright 2012, American Chemical Society. B) SEM image of NPs with disulfide-bridged and aminopropyl-modified organosilica scaffold. Reproduced with permission.^[109] Copyright 2015, Elsevier. C) Schemes of a) BTEPDS (DIS), and bridged-organosilanes containing 2PS and POR, and b) synthesis of DIS, DIS + 2PS (DIS2), and DIS + POR (DISP) NPs. TEM images of c) DIS, d) DIS2, e) ≈ 200 nm, and f) 50 nm of DISP NPs. Reproduced with permission.^[126] Copyright 2015, The Royal Society of Chemistry. D) SEM image of PSQ NPs with high content of Gd(III). Reproduced with permission.^[110] Copyright 2013, Wiley-VCH.

system of Triton X-100, 1-hexanol, cyclohexane, $\text{NH}_3 \cdot \text{H}_2\text{O}$, and water at room temperature (Figure 4D). Two disulfide bond-bridged silanes containing Gd(III) diethylenetriamine pentaacetate (Gd-DTPA) derivatives were designed and synthesized, as shown in Figure 3g.^[110] Vega et al. synthesized polysilsesquioxane NPs with four disulfide bond-bridged porphyrin in a water-in-oil microemulsion of Triton X-100, *n*-hexanol, and cyclohexane followed by the addition of a freshly prepared solution of the organosilane shown in Figure 3h, water, and $\text{NH}_3 \cdot \text{H}_2\text{O}$ at room temperature.^[111]

2.2.2. Mesoporous Organosilica Nanoparticles

In order to introduce mesopores in the abovementioned disulfide-bridged organosilica spheres,^[124] Kim et al. added CTAB or octadecyltrimethoxysilane (C_{18}TMS) into the BTEPTS- $\text{NH}_3 \cdot \text{H}_2\text{O}$ -ethanol-water system. Based on TEM analysis of the as-prepared, air-calcined, and N_2 -calcined products (Figure 5), the CTAB-BTEPTS organosilica nanospheres (size: 150 nm) showed a hydrocarbon-rich core and a silica-rich shell-like nanostructure, while C_{18}TMS -BTEPTS organosilica nanospheres

(size: 150 nm) showed the reverse situation. Teng et al. synthesized uniform MONs with disulfide-bridged organosilica frameworks in the BTEPTS-TEOS-CTAB- $\text{NH}_3 \cdot \text{H}_2\text{O}$ -ethanol-water system at 35 °C with a molar ratio of 0.179 of BTEPTS/TEOS.^[129–131] The particle size could be tailored in the range of 90–290 nm by adjusting the CTAB concentration or the ethanol/water volume ratio. De Cola and co-workers synthesized disulfide-bridged MONs with the grafting of fluorescent dye molecules in a BTEPDS-TEOS-CTAB- NaOH -ethanol-water system at 80 °C with a 3/7 molar ratio of BTEPTS/TEOS using the one-pot co-condensation method.^[132] The dye introduction was achieved by the addition of rhodamine B isothiocyanate (RITC) –modified APTES before adding BTEPTS and TEOS. EDX elemental mapping revealed the homogeneous distribution of S over the entire particle structure. Möller and Bein prepared a series of disulfide-bridged MONs in the BTEPDS/BTEPTS-TEOS-cetyltrimethylammonium chloride (CTAC)-triethanolamine (TEA)- NH_4F -triisopropyl benzene (TIPB)-water system at 90 °C.^[133] The increase of BTEPDS/BTEPTS molar ratio from 1/10 to 1/2 led to a successive loss of surface area from 976 to 530 $\text{m}^2 \text{g}^{-1}$ accompanied by a reduction of pore size. Interestingly, all of MON samples became increasingly

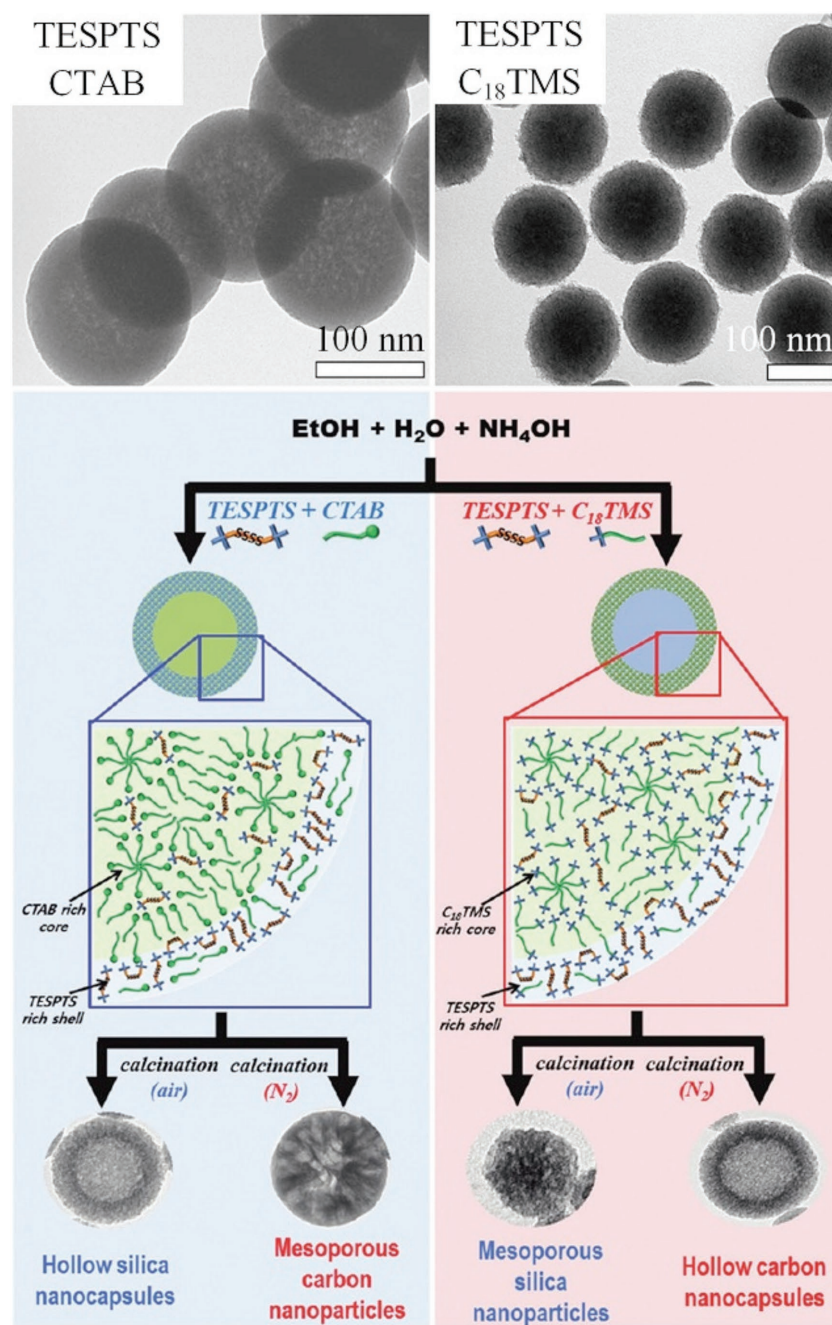


Figure 5. TEM images and schemes of TESPTS (i.e., BTEPTS)-based nanostructured organosilica materials from self-assembly between BTEPTS and mediator (CTAB or $C_{18}TMS$) and subsequent topological transformations. Reproduced with permission.^[124] Copyright 2012, American Chemical Society.

aggregated under higher organic content. In addition, amino-propyl and mercaptopropyl functions could be selectively introduced in the particle interior and on the outer surface by the delayed addition of APTES and 3-mercaptopropyltriethoxysilane (MPTES).

Chen and co-workers reported the synthesis of monodisperse dendrimer-like disulfide-bridged MONs with small particle size (size about 30 nm) and large radial mesopores (size between 8 and 13 nm) in a BTEPTS–TEOS–CTAC–TEA–water

system at 95 °C based on a micelle and precursor co-templating assembly strategy (Figure 6A).^[134–137] The possible formation mechanism was ascribed to the penetration of the long hydrophobic chain ($-\text{CH}_2-\text{C}(\text{H}_2-\text{CH}_2-\text{S}-\text{S}-\text{S}-\text{S}-\text{CH}_2-\text{CH}_2-\text{CH}_2-)$) of the partially hydrolyzed BTEPTS molecules into the hydrophobic zones of surfactant CTAC micelles, resulting in substantially enlarged micelles, and thus larger pore sizes (Figure 6B). The pore sizes could easily be tuned by varying the TEA or/and BTEPTS contents (Figure 6C), while the particle sizes could be controlled by regulating the mass ratio of TEA/CTAC, BTEPTS/TEOS, or BTEPDS/TEOS.^[136] Furthermore, based on this strategy, the authors also achieved interfacial growth of disulfide-bridged MONs with large radial mesopores on the surface of conventional MSNs (Figure 6D,E), thus constructing core-shell hierarchical dual-modal mesoporous NPs.^[138,139] Yu and co-workers synthesized degradable dendritic MONs (DMONs) with disulfide-bridged organosilica frameworks in a BTEPTS–TEOS–CTAB–sodium salicylate (NaSal)–TEA–water system at 80 °C.^[140] Both the particle size and the pore size could be tailored up to ≈ 500 nm and up to ≈ 40 nm, respectively, by tuning the CTAB/NaSal molar ratio (Figure 7).

2.2.3. Core–Shell, Yolk–Shell, and Hollow Mesoporous Organosilica Nanoparticles

Templating is a common method to synthesize core-shell, yolk-shell (rattle-type), or hollow MONs.^[141,142] By using a “self-template selective etching” strategy (Figure 8A), Teng et al. reported the synthesis of yolk-shell structured MONs with disulfide-bridged organosilica frameworks via hydrothermal treatment of MONs with disulfide-bridged organosilica frameworks.^[129,143] Interestingly, when disulfide-bridged MONs were etched with a NaOH solution at room temperature for appropriate time, disulfide-bridged hollow MONs (HMONs) with a flexible and deformable structure were formed (Figure 8B).^[70]

Moreover, a so-called “multi-interface transformation” approach combined with “multihybridization” was developed.^[144–146] Disulfide (core and internal shell)- and ethane (external shell)-bridged HMONs with an inner core and double hollow shell were prepared by coating an ethane-bridged organosilica layer on disulfide-bridged organosilica NPs (Figure 9a–g).^[144] Furthermore, yolk-shell-structured triple (ethane, disulfide, and benzene)-hybridized HMONs were synthesized with a mixture of TEOS, bis(triethoxysilyl)ethane (BTEE, $-\text{CH}_2-\text{CH}_2-$), BTEPTS, and bis(triethoxysilyl)benzene

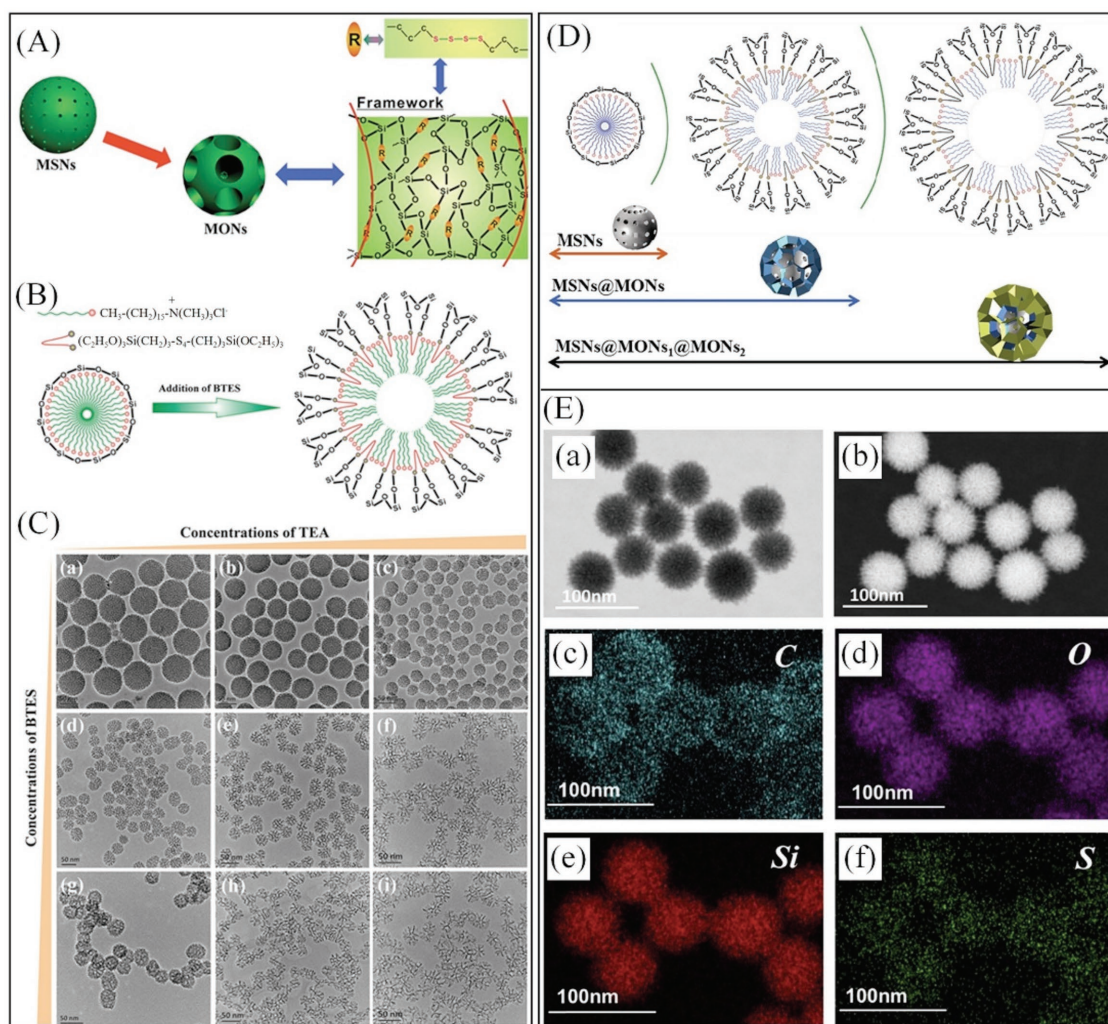


Figure 6. A) Schematic illustration of composition and structure of disulfide-bridged MONs. B) Possible micelle/precursor co-templating assembly strategy to enlarge the micelle size by incorporating hydrophobic long organic chains into the hydrophobic zone of CTAC micelles. C) TEM images of disulfide-bridged MONs prepared under varied TEA and BTES (i.e., BTEPTS) amounts. Reproduced with permission.^[134] Copyright 2017, Wiley-VCH. D) Schematic illustration of the formation mechanism. E) a) Bright-field, b) dark-field scanning transmission electron microscopy (STEM), and c–f) element mapping images of MSNs@MONs with core-shell hierarchical mesoporous nanostructure. Reproduced with permission.^[138] Copyright 2017, Elsevier.

(BTEB, $-\text{C}_6\text{H}_4-$) with molar ratios of 5.6:10.8:2.0: 2.5 (Figure 9h–m).^[145] However, hydrothermal treatment resulted in high degree of silica condensation, thus decreasing the biodegradation capability caused by quick GSH-triggered disulfide cleavage and slow hydrolysis reaction.^[129,144–146]

The strategy of selective core etching of core-shell structured SiO_2 @MONs was developed to synthesize a series of HMONs with various framework components, based on the principle that Si–C bonds within the MON shell are more stable than Si–O bonds within the SiO_2 core.^[147–151] By using solid silica nanospheres as core, Shi and co-workers synthesized several HMONs with one up to quintuple group-bridged silsesquioxane framework using a mixture of BTEPTS (R_1 = disulfide), BTEB (R_2 = benzene), bis(triethoxysilyl)ethene (BTEEE, R_3 = ethene ($-\text{CH}=\text{CH}-$)), BTEE (R_4 = ethane), and bis(triethoxysilyl) biphenyl (BTEBP, R_5 = biphenyl) (Figure 10A).^[147] In addition, by replacing solid silica nanospheres with small MSNs as cores, they prepared disulfide-bridged HMONs with a particle

size of ≈ 40 nm (Figure 10B).^[148–151] Moreover, they synthesized HMONs with varied pore diameters by tuning the volume ratios (5:3, 5:6, 5:9, and 5:12) of TEOS to BTEPDS during the coating process, and achieved scale-up synthesis of more than 10 g.^[149] However, the increase of $V_{\text{TEOS}}/V_{\text{BTEPDS}}$ led to the increased aggregation of NPs. The authors also succeeded in synthesizing monodisperse disulfide-bridged HMONs with large mesopore size of about 6–9 nm by selectively etching the core of the abovementioned hierarchical dual-modal mesoporous NPs.^[139] Fan et al. also employed this strategy to synthesize disulfide-bridged HMONs (size: 184 nm) by using BTEPTS as the sole silane during the coating process (Figure 10C).^[152]

Liu and co-workers reported a facile synthesis of core-shell structured polymer@disulfide-bridged organosilica nanospheres via triconstituent co-assembly of 3-aminophenol, formaldehyde, and BTEPDS by employing a Stöber-like approach.^[153] Du and co-workers synthesized a series of uniform disulfide-bridged hollow organosilica NPs (HONs) with particle sizes smaller than

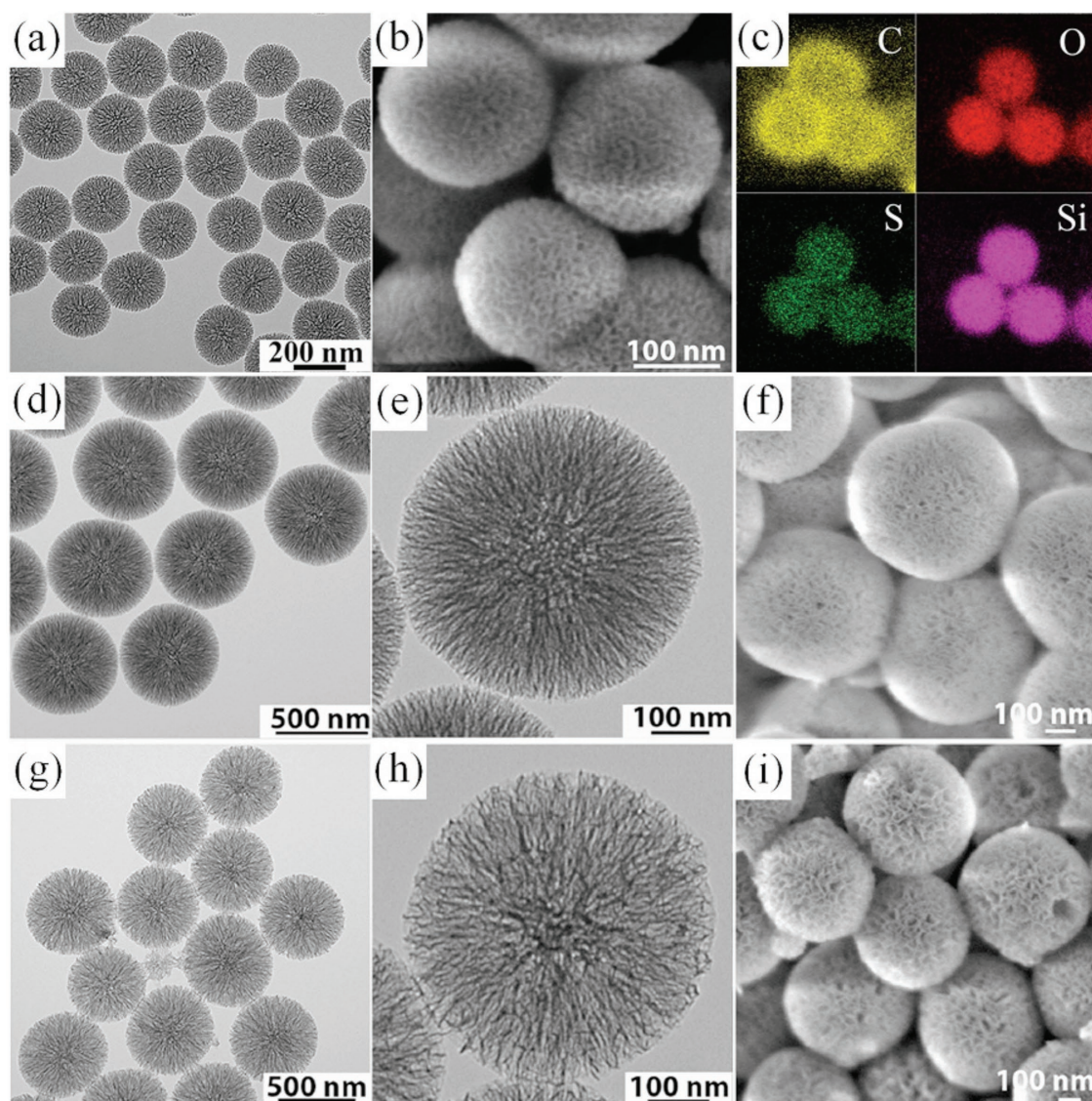


Figure 7. a,d,e,g,h) TEM, b,f,i) SEM, and c) EDX mapping images of DMONs synthesized at NaSal/CTAB molar ratio of a–c) 0.5/1, d–f) 1/2, and g–i) 1/1. Reproduced with permission.^[140] Copyright 2016, American Chemical Society.

100 nm by employing poly(acrylic acid) (PAA) as a core template (**Figure 11**).^[154] With an increase of BTEPTS or BTEPDS/TEOS volume ratio from 0.2/1.3 to 0.9/0.6, the shell thickness of HMONS could gradually and slightly be decreased, while the roughness of the interior and exterior surfaces, and the sulfur (S) content progressively increased. Zhang and co-workers prepared disulfide-bridged HONs by using sulfonic group-modified polystyrene (PS) nanospheres as a core template via co-condensation of TEOS, APTMS, and a disulfide-bridged silane (**Figure 3d**) in ethanol in the presence of ammonia.^[155]

2.2.4. Nanorods and Multipods

Croissant et al. synthesized ethene- and disulfide-bridged periodic mesoporous organosilica (PMO) nanorods and nanospheres in CTAB–NaOH–ethanol–water system, whose

shapes and sizes appeared to be related to the volume ratio ($R_{E/DIS}$) of BTEEE (E) to BTEPDS (DIS) (**Figure 12A**).^[127] The increase of $R_{E/DIS}$ from 100/0 to 0/100 gave rise to shape evolution from long ethene-bridged PMO nanorods to short mixed nanorods, then to mixed NPs, and finally to nonporous disulfide-bridged NPs. Ou-Yang and co-workers fabricated disulfide-bridged PMO nanorods with tunable aspect ratios of 2, 3, and 4 in a TEOS–BTEPTS–CTAB–NaOH–ethanol–water system by regulating the water amount.^[156] Yu et al. prepared disulfide-bridged PMO nanorods with higher aspect ratios from 1.4:1 to 9.5:1 in a similar system by tuning the molar quantities of CTAB and $NH_3 \cdot H_2O$.^[136] Croissant et al. also prepared hybrid multipodal PMO NPs composed of spherical benzene-bridged PMO cores and irregular ethene- and disulfide-bridged PMO pods with different lengths by the interfacial nucleation and growth of rods on the core surface (**Figure 12B**).^[157]

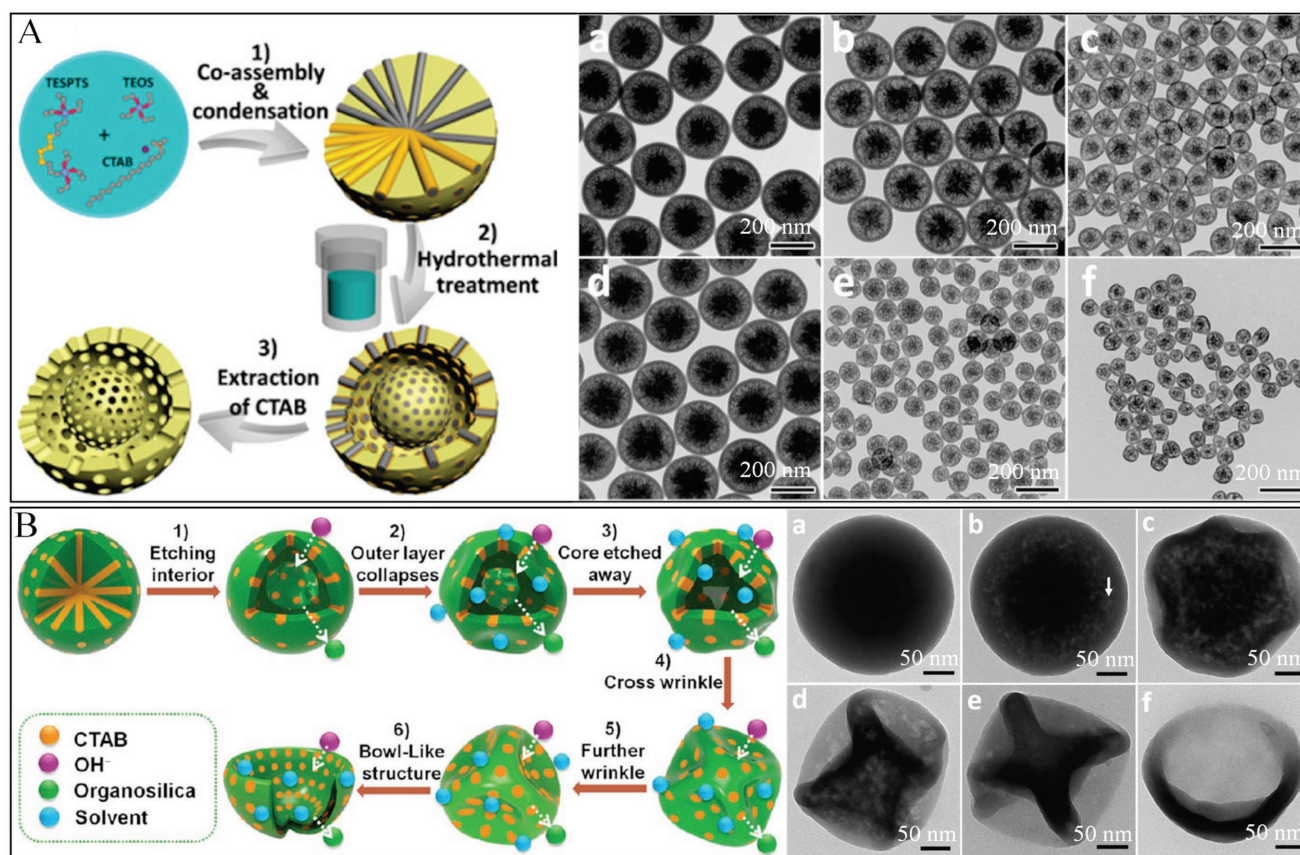


Figure 8. A) Schematic illustration (left) of synthesis process of yolk-shell structured MONs with disulfide-bridged organosilica frameworks by hydrothermal treatment, based on a “self-template selective etching” strategy. TEM images (right) of disulfide-bridged MONs with tunable structures fabricated with CTAB concentrations of a) 2.1, b) 3.2, and c) 6.3 mmol L⁻¹, and at ethanol/water volume ratios of d) 0.46, e) 0.35, and f) 0.32. Reproduced with permission.^[129] Copyright 2014, American Chemical Society. B) Schematic illustration (left) of formation mechanism of the disulfide-bridged HMONs deformable structure by etching with NaOH solution at room temperature. TEM images (right) of the corresponding products obtained by incubation in NaOH solution for varied time: a) 1, b) 3, c, d) 5, e) 20, and f) 60 min. Reproduced with permission.^[70] Copyright 2018, American Chemical Society.

2.2.5. Nanocomposites

Disulfide-bridged organosilicas can be coated on the surface of functional entities to form a biodegradable shell, thus producing core-shell nanocomposites.^[158–165] The design advantages are the shell can not only protect the stability of organic species in the extracellular environment, but it can also achieve GSH-triggered biodegradation in the intracellular microenvironment, especially in cancer cells of tumor tissues, accompanied by the responsive release of encapsulated functional molecules for specific diagnostic and/or therapeutic functions. Botella et al. synthesized hybrid NPs with a disulfide-bridged organosilica shell and a pyrene-loaded complex core composed of CTAB and biodegradable poly(lactic-co-glycolic acid) (PLGA) polymer (Figure 13A).^[158] The protective shell was formed on the core surface by co-condensation of TEOS and TESPDS with a molar ratio of TESPDS/TEOS of 0.2 in the NH₄OH-isopropanol-water system. Zhang and co-workers encapsulated rhodamine-modified chitosan (CS-RhB) as a macromolecular model drug with disulfide- and ethene-bridged organosilicas to form core-shell-structured nanocapsules for a redox-triggered shell degradation and subsequent drug release.^[159] Hayashi et al.

presented a one-pot synthesis strategy for doxorubicin (DOX) and photosensitizer (magnesium phthalocyanine, MgPc)-co-contained hollow NPs (DOX and MgPc HNPs) with a disulfide and siloxane framework by interface reactions of oil-in-water emulsion nanodroplets.^[108] As illustrated in Figure 13B, the formation of the hybrid NPs was achieved by both the hydrolysis–condensation reaction between 3-mercaptopropyltrimethoxysilane (MPTMS) and 3-thiocyanatopropyltriethoxysilane (TPTES), and the nucleophilic substitution reaction between the thiol of MPTMS and the thiocyanate of TPTES at the interface (Figure 3e). Timin et al. developed a straightforward strategy to coat (poly(allyl)amine hydrochloride (PAH)/poly(styrene) sulfonate (PSS))₄ microcapsules with disulfide-bridged organosilica shell while simultaneously achieving in situ DOX encapsulation by interfacial hydrolysis–condensation of TEOS and BTEPTS (Figure 13C).^[160] Prasetyanto et al. proposed a smart approach to encapsulate native proteins with disulfide-bridged organosilica matrices as a shell.^[161] The reaction was performed in the water-in-oil microemulsion of Triton X-100, *n*-hexanol, cyclohexane, cytochrome C, water, TEOS, and TESPDS followed by the addition of ammonia solution at room temperature. Based on a similar water-in-oil microemulsion system,

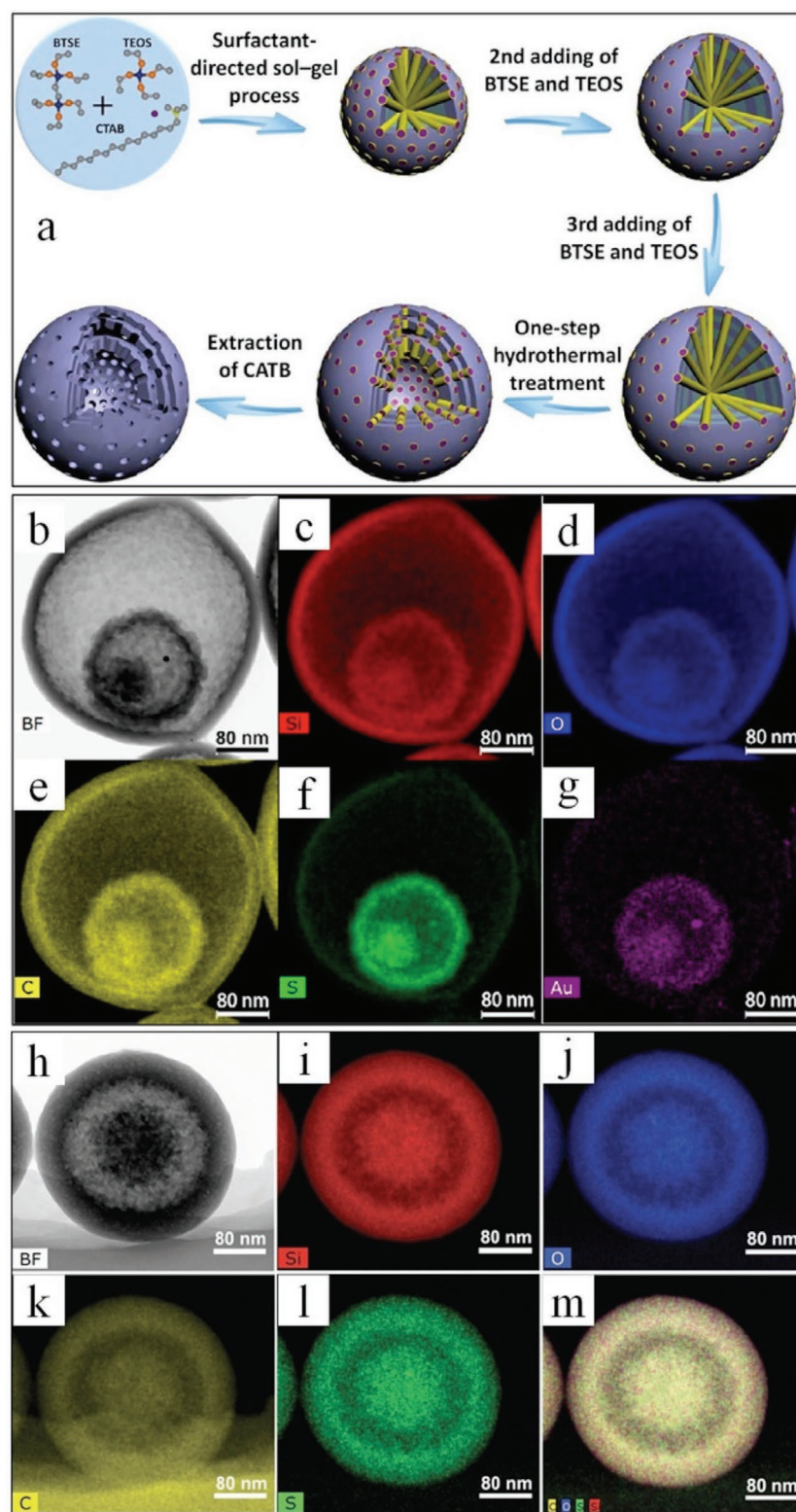


Figure 9. a) Schematic illustration of synthesis process of triple-shelled HMons by the multi-interface transformation approach. Reproduced with permission.^[144] Copyright 2014, American Chemical Society. b,h) TEM and c–g, i–m) EDX elemental mapping images of b–g) the double-shelled disulfide (internal shell)- and ethane (external shell)-bridged HMons. Reproduced with permission.^[144] Copyright 2014, American Chemical Society. h–m) and yolk-shell-structured triple (ethane-, disulfide-, and benzene)-hybridized HMons. Reproduced with permission.^[145] Copyright 2016, Wiley-VCH.

Yang et al. fabricated carbon dots-encapsulated disulfide-bridged organosilica nanocapsules (CDs@DONs) for responsive fluorescent detection. The synthesis was achieved by co-condensation of TEOS and BTEPDs, where hundreds of CDs were entrapped in each nanocapsule (Figure 13D).^[162] Hsu and co-workers coated the surface of Au NPs with a thin layer of disulfide-bridged and aminopropyl-contained organosilicas by using both substitution and hydrolysis co-condensation reactions of APTMS and cross-linker dithiobis(succinimidyl propionate) (DTSP) (Figure 3f) in aqueous solution at room temperature.^[163] Tian et al. achieved the interfacial growth of disulfide-bridged organosilica on the surface of Prussian blue (PB) nanocubes to form a mesoporous shell (thickness: 17 ± 1 nm) by co-condensation of TEOS and BTEPTS at the volume ratio of 1/10 in the CTAB- NH_4OH -ethanol-water system to generate an imaging-guided photothermal-chemotherapy system (Figure 13E).^[165]

In addition, besides its role as the protective and responsive shell, another option is to uniformly distribute various functional organic molecules into disulfide-bridged organosilica framework to form hybrid NPs. For example, Zhang et al. realized the uniform distribution of DOX drug molecules in the disulfide-bridged NPs by reaction of DOX, TEOS, and organosilanes (named BTOCD) in Figure 3d in ethanol-containing ammonia (Figure 13F).^[166]

3. Redox-Triggered Degradation, Biocompatibility, and Nanobiomedical Applications

The reaction schemes of disulfide bond reduction by GSH or DL-dithiothreitol (DTT, a commonly used strong reducing agent) are depicted in Figure 14a,b.^[167,168] Moreover, Figure 14c displays the possible biodegradation mechanism of a disulfide-bridged silsesquioxane framework: GSH-triggered redox reaction for disulfide-bond breaking (fast rate step) and aqueous medium (H^+ or OH^-)-induced hydrolysis reaction for $-\text{Si}-\text{O}-\text{Si}-$ bond breaking (slow rate step). The hydrolytic degradation generally involves three steps: i) the adsorption of H_2O on the siloxane framework, especially in the case of low condensation degree (i.e., $-\text{Si}-\text{OH}$ exists), via hydration, ii) the hydrolysis reaction whereby one siloxane is hydrolyzed into two silanols, and iii) the formation of silicic acid via multiple hydrolysis reactions, its subsequent

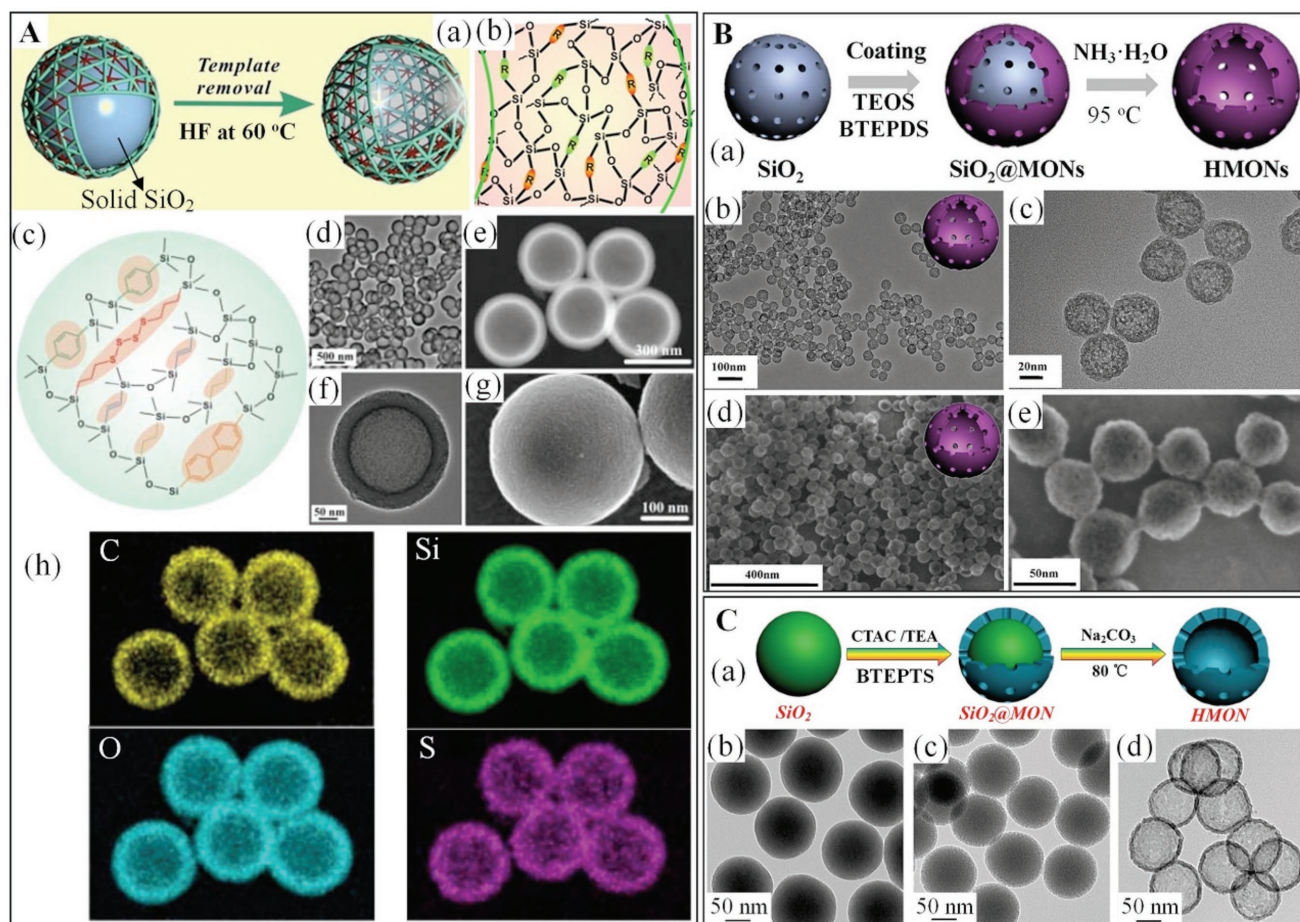


Figure 10. A) Schematic illustration of a) templating method to synthesize HMONs with b) multiple-bridged silsesquioxane framework and c) quintuple-bridged HMONs of (R_1 = disulfide, R_2 = benzene, R_3 = ethylene, and R_4 = ethane). d, f) Bright-field, e) dark-field TEM, g) SEM, and h) EDX element mapping images of quadruple-bridged HMONs. Reproduced with permission.^[147] Copyright 2014, American Chemical Society. B) a) Synthesis scheme, b, c) TEM, and d, e) SEM images of HMONs. Reproduced with permission.^[149] Copyright 2017, Elsevier. C) a) Synthesis scheme and b–d) TEM images of b) SiO₂, c) SiO₂@MONs, and d) HMONs. Reproduced with permission.^[152] Copyright 2016, Wiley-VCH.

leaching, and reaction under different pH (polysilicic acid (under pH < 2), Si(OH)₄ (relatively stable under pH 2–3 in very dilute aqueous solution), polysilicic acid (under 3 < pH < 9) or silicate (HSiO₃[−] or SiO₃^{2−} under pH > 9–10)).^[169] The basic chemistry of silicic acid is rather complex owing to the variety of silicon species in different aqueous solutions depending on pH, ionic strength, and reaction temperature.^[169] Furthermore, the hydrolytic degradation rate depends on the concentrations of surface groups: neutral silanol (Si–OH), protonated silanol (Si–OH₂⁺), and deprotonated silanol (Si–O[−]).^[170] It is easy to detect the formed thiol groups (–SH, stretching vibration peak at around 2550–2590 cm^{−1}) and silanol groups (–Si–OH, stretching vibration peak at around 960 cm^{−1}) by Fourier transform infrared (FTIR) spectroscopy. Based on the analysis of valence-bond theory, the bond length follows the order: –S–S– (≈202 pm) > –Si–C– (≈188 pm) > –Si–O– (≈162 pm); thus, the bond energy follows the opposite order.^[139,149] In turn, it may be easier to break the –Si–C– than –Si–O– by a nucleophilic substitution reaction during the degradation process.^[171,172] Ozin and co-workers reported the loss of almost all organic (benzene or thiophene) moieties under strongly basic

conditions and the removal of a proportion of organic moieties under acidic conditions during the synthesis of benzene- or thiophene-bridged PMO powders due to the cleavage of the –Si–C– bonds.^[171] Unfortunately, insufficient studies investigated whether or not the –Si–C– bond could be broken during redox-triggered degradation experiments, where it is important to determine what are the resulting degraded products. This redox reaction generally occurs at neutral or weak basic conditions, which can stabilize the reductive thiolate anion (S[−], pK_a = 8.3), while it is impossible to achieve the deprotonation of thiol groups (–SH) under acidic conditions. As shown in Table 3, GSH-triggered biodegradation behaviors of disulfide-bridged silsesquioxane frameworks have been investigated in a few reports. Most materials exhibited GSH-triggered and time-dependent degradation upon incubation, but displayed different biodegradation rates depending on the –S–S– content, other doped species, types of nanostructures, condensation degree of –Si–O–Si– bond (i.e., silanol (–Si–OH) content), synthesis conditions, etc. In addition, particle concentrations, the type and concentrations of the reducing agents, stirring rate, and temperature also affected the degradation rates. The

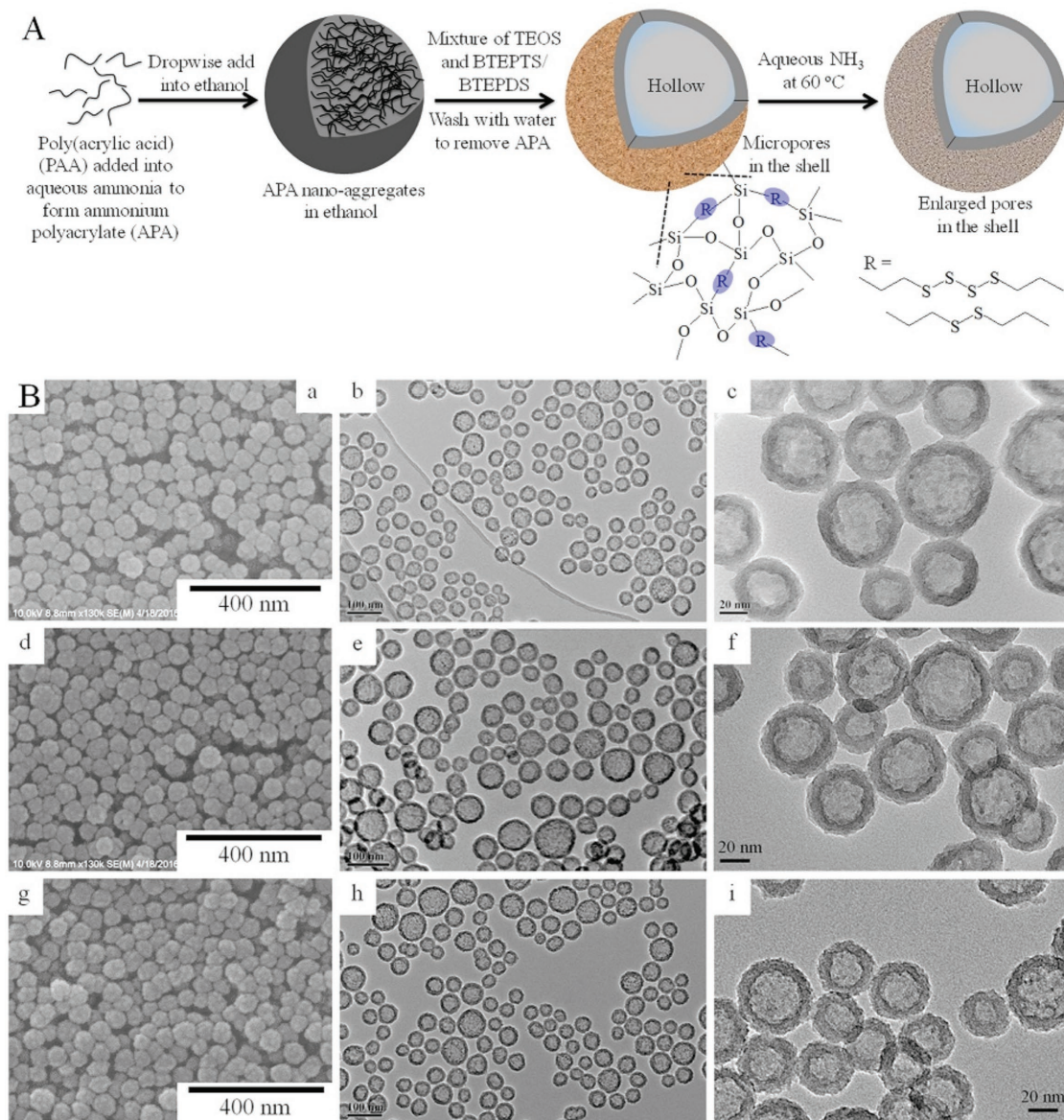


Figure 11. A) Schematic representation of the design and synthesis of HMons with a disulfide-bridged silsesquioxane framework. B) SEM and TEM images of HMons fabricated under varied volume ratios of TEOS/BTEPTS-4S (mL): a–c) 1.3/0.2, d–f) 1.1/0.4, and g–i) 0.9/0.6. Reproduced with permission.^[154] Copyright 2017, The Royal Society of Chemistry.

degradation rate is generally compared to that of a similar counterpart without disulfide function, while it is difficult to compare the biodegradation rates among publications because the characteristics of NPs and the degradation conditions usually differ significantly. Nevertheless, intracellular and in vivo degradation behaviors are dynamic and have much more complicated influencing factors; it is therefore difficult to monitor the “real-time,” accurate degradation process owing to complex environments and technological obstacles. It is expected that the intracellular GSH-triggered biodegradation of hybrid NPs with disulfide-bridged silsesquioxane framework can accelerate/regulate the release rate of loaded guest molecules for better biological effects, facilitate their excretion, and improve their biosafety. The possible in vivo destiny of these hybrid NPs

is deduced to be that after intravenous injection into blood and subsequently circulating in the blood system, that is, NPs are first taken up by tumor cells via passive or active targeting; next they escape from endosomes; then GSH-triggered biodegradation along with cargo release occurs, executing their therapeutic function; and finally the degraded products with small sizes ($\text{HD} \leq 6 \text{ nm}$) diffuse through the blood stream or the lymphatic system to be eventually cleared from the body via urine and feces. In addition, after a number of NPs are captured by RES, including liver, spleen, and lungs, the particles may still remain mostly undegraded. Thus, only a little amount of loaded cargos may release into normal tissues before excretion from these organs, resulting in the suppressed toxic side effects. Redox-triggered biodegradation behaviors combined with

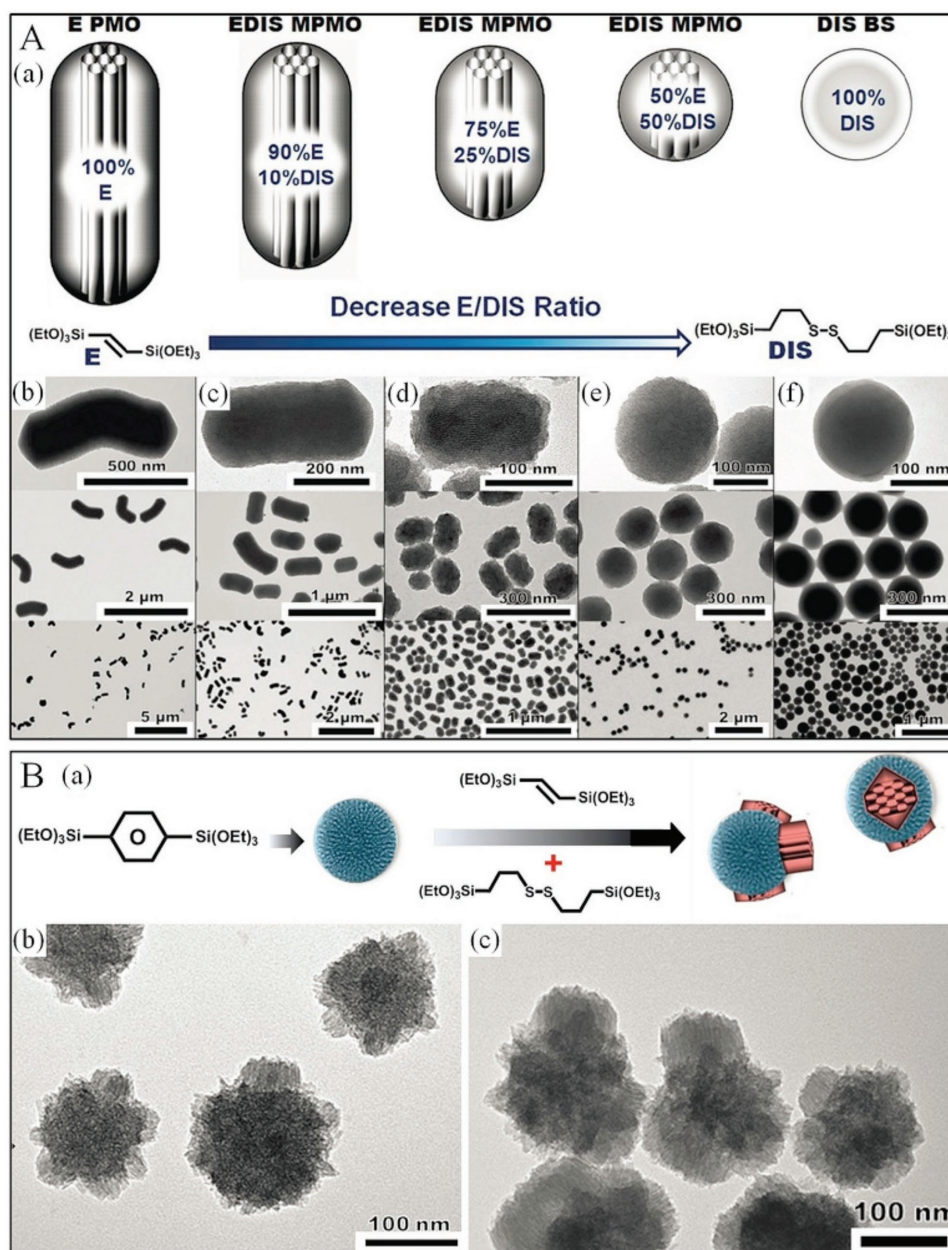


Figure 12. A) a) Structural and compositional schemes and b–f) TEM images of b) ethene-bridged PMO nanorods, c,d) ethene- and disulfide-bridged PMO nanorods, and e) ethene- and disulfide-bridged NPs, and f) nonporous disulfide-bridged NPs by the regulation of the volume ratio ($R_{E/DIS}$) of BTEEE (E)/BTEPDS (DIS) of 100/0, 90/10, 75/25, 50/50, and 0/100, respectively. Reproduced with permission.^[127] Copyright 2014, Wiley-VCH. B) (a) Synthesis scheme of hybrid multipodal PMO NPs composed of spherical benzene-bridged PMO cores and rod-shaped ethane- and disulfide-bridged PMO pods. TEM images of PMO NPs with b) short and c) longer pods. Reproduced with permission.^[157] Copyright 2015, Wiley-VCH.

biocompatibility and nanobiomedical applications are summarized and discussed in the following section.

3.1. Nonporous Nanoparticles

When dispersed in solutions at pH 7.4 (Tris buffer) and pH 4.5 (acetate buffer), the silica dissolution rates of dye-introduced and disulfide-bridged NPs (0.6 mg mL^{-1}) decreased with the increase of incorporated disulfide groups, while it had the

opposite effect when dispersed in Tris buffer solution (pH 7.4) in the presence of DTT ($1.4 \times 10^{-3} \text{ M}$), due to DTT-triggered cleavage of disulfide bonds.^[125] In addition, when adult dermal fibroblasts were incubated with NPs for 7 days, the structure evolved from porous to hollow, suggesting more sensitivity of the particle interior domains to the intracellular reducing conditions.^[125] GSH ($8 \times 10^{-3} \text{ M}$) in phosphate buffered saline (PBS) solution (pH 7.4) caused a structural change of bis(propylamide-ethyl)disulfide-bridged organosilica NPs with sizes of ≈ 50 and 200 nm from intact NPs to toroidal NPs (1 day),

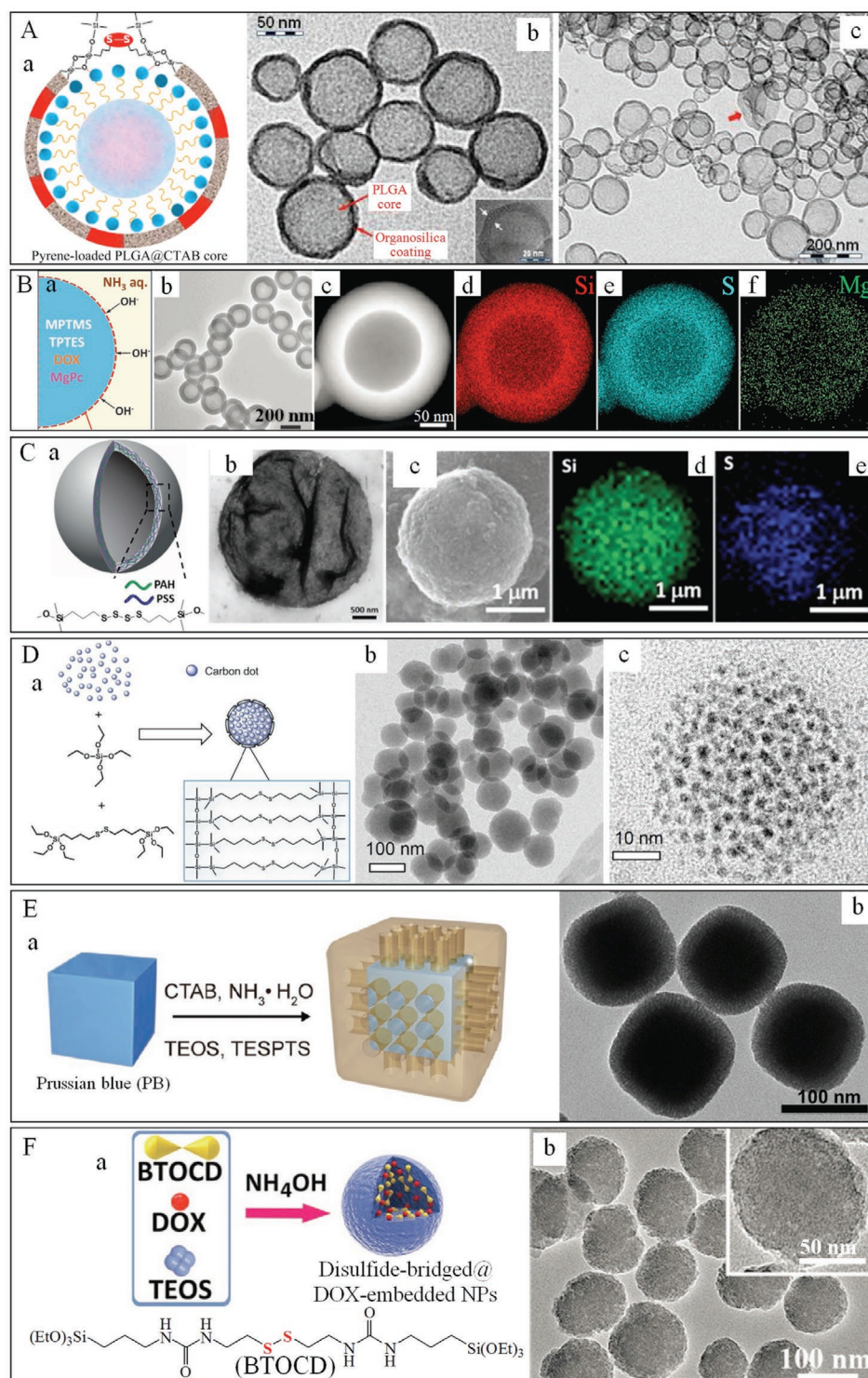


Figure 13. A) a) Schematic illustration and b, c) TEM images of pyrene-loaded composite NPs with a PLGA and CTAB core and an amorphous disulfide-bridged organosilica shell. Reproduced with permission.^[158] Copyright 2013, American Chemical Society. B) a) Schematic illustration of emulsion nanodroplets for the synthesis of DOX&MgPc HNPs. b) TEM, c) STEM, and d–f) EDX elemental mapping images of DOX&MgPc HNPs. Reproduced with permission.^[108] Copyright 2016, Wiley-VCH. C) a) Schematic illustration, b) TEM, c) SEM, and d, e) EDX elemental mapping images of (PAH/PSS)₄ microcapsules coated with disulfide-bridged organosilica shell. Reproduced with permission.^[160] Copyright 2017, Wiley-VCH. D) a) Schematic illustration of the synthesis and structure, and b, c) TEM images of the CDs@BONs. Reproduced with permission.^[162] Copyright 2018, American Chemical Society. E) a) Schematic illustration and b) TEM image of PB nanocubes coated with disulfide-bridged mesoporous organosilica shell. Reproduced with permission.^[165] Copyright 2017, Wiley-VCH. F) a) Synthesis scheme and b) TEM image of disulfide-bridged and DOX-embedded hybrid NPs. Reprinted with permission.^[166] Copyright 2017, Wiley-VCH.

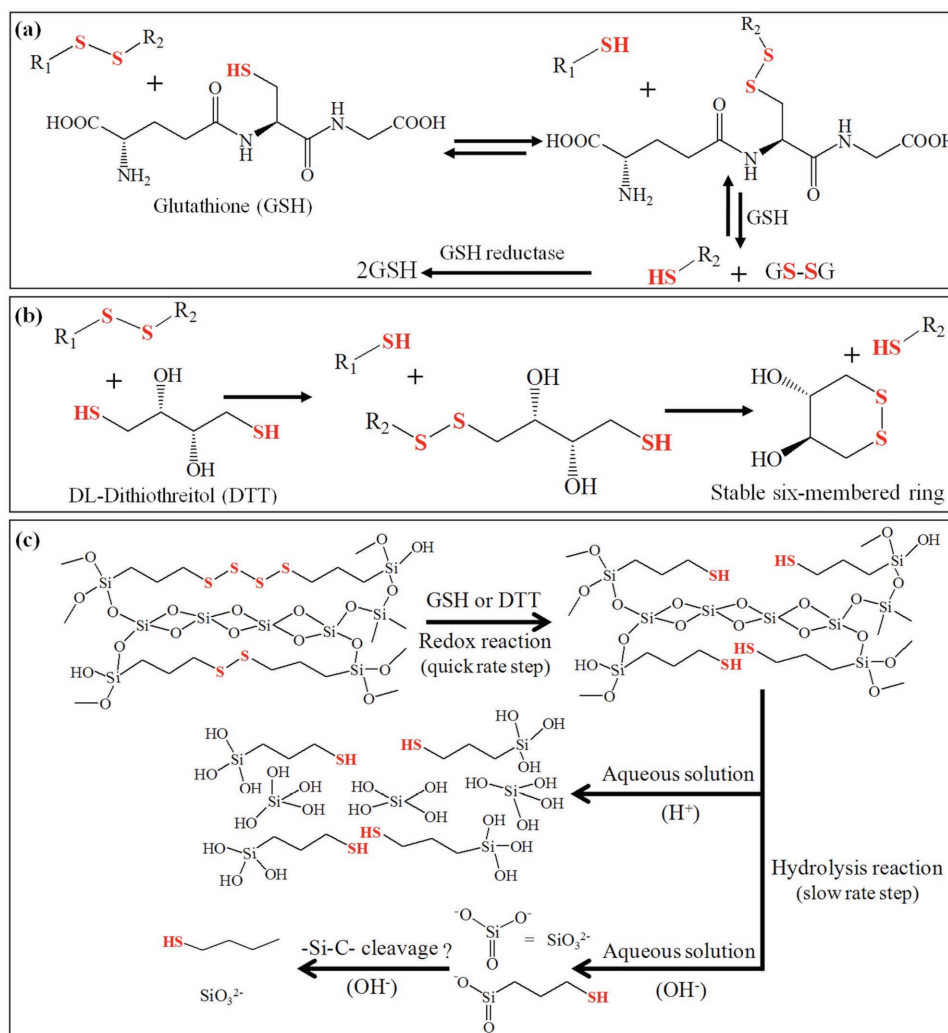


Figure 14. Reaction formulas of disulfide bond reduced by a) GSH or b) DTT. c) Possible mechanism of biodegradation of disulfide-bridged silsesquioxane framework triggered by GSH and caused by aqueous solution (H^+ or OH^-).

then to toroidal NPs with thinner shell (3 days), and finally to scattered pieces (5 days). In addition, negligible hemolytic effect was observed with particle concentration up to $500 \mu g mL^{-1}$, indicating good blood compatibility.^[107] The influence of DTT concentration at different pH values was investigated on the degradation behavior of NPs having a bis(propylamide-ethyl) disulfide-bridged and aminopropyl-modified organosilica scaffold.^[109] After treatment in $10 \times 10^{-3} M$ DTT for 1 h, the degradation decreased from 20% in neutral conditions to 5% at pH 3, indicating that neutral conditions are more favorable for redox reaction than the acidic one. The obvious time-dependent degradation from intact NPs to very small fragments was shown in scanning electron microscopy (SEM) images of **Figure 15a**, while no degradation phenomenon appeared in pure water. The surface of NPs was further modified with covalently anchored rhodamine for fluorescence imaging and electrostatically adsorbed transferrin for targeting identification as a proof of concept of drug delivery. The reductive conditions resulted in the release of more rhodamine in solutions with $10 \times 10^{-3} M$ DTT and intracellular microenvironments

of carcinoma cells (e.g., Hep G2 cells) with glutathione ethyl ester. In addition, the cytotoxicity assay displayed negligible effect of the bare NPs, functionalized NPs, and their degraded products with the formed $-SH$ groups (pretreated by DTT) on Hep G2 cell viability at concentrations below $0.4 mg mL^{-1}$.^[109] Disulfide-bridged nanospheres containing 2PS or POR gradually degraded when stirred in PBS (pH 7.4) with $2 \times 10^{-3} M$ mercaptoethanol (ME, a small-molecule reducing reagent) at $37^\circ C$ for 48 h.^[126] Dynamic light scattering (DLS) analysis and TEM images revealed the appearance of degraded fragments. In addition, both nanospheres displayed negligible cytotoxicity at concentrations below $125 \mu g mL^{-1}$ toward MCF-7 cancer cells. The TPE-fluorescence imaging showed the cellular uptake of NPs, and TPE-therapy resulted in 40–60% of cancer cell death.^[126]

PSQ NPs with disulfide-linked Gd chelates were stable in the absence of reducing agents, with only <5% release in the initial 4 h at $37^\circ C$. In contrast, after the addition of $10 \times 10^{-3} M$ cysteine, Gd chelates were quickly released with $t_{1/2}$ of 12 h. Over 90% of the Gd chelates were released after

Table 3. Framework compositions, degradation conditions and behaviors, and nanobiomedical applications. (“–” means “no investigation” in the reported references.)

| Component | Structure | Surface modification | Reducing agent | Degraded product | In vitro or in vivo degradation | Application | Ref. |
|--|-----------------|----------------------|--|--|---------------------------------|---|-----------|
| –Si–O–Si–, –Si–(CH ₂) ₃ –S ₂ –(CH ₂) ₃ –Si– | Solid | Non | 1.4 × 10 ^{–3} M DTT | Hollow NPs after 7 days | In vitro | Non | [125] |
| –Si–O–Si–, silane in Figure 3d | Solid | Non | 8 × 10 ^{–3} M GSH | Scattered pieces after 5 days | – | Non | [107] |
| –Si–(CH ₂) ₃ –NH ₂ , silane in Figure 3d | Solid | Transferrin | 10 × 10 ^{–3} M DTT | Fragments after 150 min | In vitro | Drug carrier | [109] |
| –Si–(CH ₂) ₃ –S ₂ –(CH ₂) ₃ –Si–2PS | Solid | Non | 2 × 10 ^{–3} M ME | Broken NPs and fragments after 48 h | – | TPE imaging and therapy | [126] |
| –Si–(CH ₂) ₃ –S ₂ –(CH ₂) ₃ –Si–POR | Soild | Non | 2 × 10 ^{–3} M ME | Broken NPs and fragments after 48 h | | | |
| Silane in Figure 3g | Solid | PEG | 10 × 10 ^{–3} M cysteine | >90% release after 2 days | – | MRI | [110] |
| Silane in Figure 3h | Solid | Non | 10 × 10 ^{–3} M DTT | Completely degraded after 8 days | – | Phototherapy | [111] |
| –Si–C≡C–Si–, –Si–(CH ₂) ₃ –S ₂ –(CH ₂) ₃ –Si– | MONs, rods | Non | 2 × 10 ^{–3} M ME | Broken NPs and fragments after 48 h | – | Drug delivery | [127] |
| –Si–O–Si–, –Si–(CH ₂) ₃ –S ₂ –(CH ₂) ₃ –Si– | MONs | RGD peptide | 5 × 10 ^{–3} M DTT, 10 × 10 ^{–3} M GSH | Fragments after 7 days | In vitro | Drug delivery | [132] |
| –Si–O–Si–, –Si–(CH ₂) ₃ –S ₂ –(CH ₂) ₃ –Si– | MONs or solid | Non | 8 × 10 ^{–3} M GSH | Different fragments after 15 days | In vitro | Drug delivery | [128] |
| –Si–O–Si–, –Si–(CH ₂) ₃ –S ₄ –(CH ₂) ₃ –Si– | MONs | | | | | | |
| –Si–O–Si–, –Si–(CH ₂) ₃ –S ₄ –(CH ₂) ₃ –Si– | MONs | PEI | 10 × 10 ^{–3} M GSH | Small debris with sizes of ≈35 nm after 2 days | In vitro | Protein delivery | [140] |
| –Si–O–Si–, –Si–(CH ₂) ₃ –S ₄ –(CH ₂) ₃ –Si– | MONs | Non | 10 × 10 ^{–3} M GSH | Less rough and less dense after 7 days | – | Non | [133] |
| –Si–O–Si–, –Si–(CH ₂) ₃ –S ₂ –(CH ₂) ₃ –Si– | MONs | PEG | 10 × 10 ^{–3} M GSH | ≈5 nm of fragments after 7 days | In vitro | Drug therapy | [136] |
| –Si–O–Si–, –Si–(CH ₂) ₃ –S ₄ –(CH ₂) ₃ –Si– | HMONs | PEG | 10 × 10 ^{–3} M GSH | Cracked NPs and small fragments | In vitro | Drug delivery | [154] |
| –Si–O–Si–, silane in Figure 3d | HONs | Non | 20 × 10 ^{–3} M GSH | Complete fragmentation after 2 days | – | Drug delivery | [155] |
| –Si–(CH ₂) ₃ –S ₄ –(CH ₂) ₃ –Si– | HMONs | Non | 10 × 10 ^{–3} M GSH | Almost complete degradation in 30 days | – | Gas therapy | [152] |
| –Si–C ₆ H ₄ –Si–, –Si–(CH ₂) ₃ –S ₄ –(CH ₂) ₃ –Si– | HMONs | Non | 10 × 10 ^{–3} M GSH | Broken NPs and fragments after 4 days | – | Drug therapy | [147–149] |
| –Si–O–Si–, –Si–(CH ₂) ₃ –S ₂ –(CH ₂) ₃ –Si– | HMONs | PEG | 10 × 10 ^{–3} M GSH | No intact HMONs after 14 days | In vitro In vivo | Drug therapy | |
| –Si–O–Si–, –Si–(CH ₂) ₃ –S ₂ –(CH ₂) ₃ –Si–, MnPPiX | HMONs | PEG | 10 × 10 ^{–3} M GSH | Broken NPs and fragments after 7 days | In vitro | MRI-guided SDT | |
| –Si–O–Si–, –Si–(CH ₂) ₃ –S ₂ –(CH ₂) ₃ –Si– | HMONs | PEG | 10 × 10 ^{–3} M GSH | Broken NPs and fragments after 7 days | In vitro | PA imaging-guided chemotherapy | [150] |
| –Si–O–Si–, –Si–(CH ₂) ₃ –S ₄ –(CH ₂) ₃ –Si– | HMONs | PEG | 10 × 10 ^{–3} M GSH | Floccules after 3 weeks | – | Multimodality imaging-guided radiotherapy | [151] |
| –Si–O–Si–, –Si–(CH ₂) ₃ –S ₂ –(CH ₂) ₃ –Si– | Shell | Non | 100 × 10 ^{–3} M DTT | Collapsed particles after 7 days | – | Drug release | [158] |
| –Si–C≡C–Si–, –Si–(CH ₂) ₃ –S ₂ –(CH ₂) ₃ –Si– | Shell | Drug | 5 × 10 ^{–3} M GSH | Small fragments after 24 h | In vitro | Drug delivery | [159] |
| –Si–O–Si–, –Si–(CH ₂) ₃ –S ₂ –(CH ₂) ₃ –Si– | Protein hybrids | Non | 5 × 10 ^{–3} M GSH | Broken capsules after 2 days | In vitro | Protein delivery | [161] |
| –Si–O–Si–, –Si–(CH ₂) ₃ –S ₄ –(CH ₂) ₃ –Si– | Shell | PEI | 10 × 10 ^{–3} M GSH | Accelerated siRNA release after 6 h | – | Gene/chemo therapy | [138] |

Table 3. Continued.

| Component | Structure | Surface modification | Reducing agent | Degraded product | In vitro or in vivo degradation | Application | Ref. |
|--|--------------|----------------------|-----------------------------------|--|---------------------------------|-------------------|-------|
| $-\text{Si}-(\text{CH}_2)_3-\text{S}_2-(\text{CH}_2)_3-\text{Si}-$ | Shell | FA-PEG | $10 \times 10^{-3} \text{ M GSH}$ | Deformed shell framework | – | Trimodal therapy | [108] |
| $-\text{Si}-\text{O}-\text{Si}-$, $-\text{Si}-(\text{CH}_2)_3-\text{S}_4-(\text{CH}_2)_3-\text{Si}-$ | Hybrid shell | Non | $20 \times 10^{-3} \text{ M GSH}$ | Broken capsules and fragments after 24 h | – | Drug delivery | [160] |
| $-\text{Si}-\text{O}-\text{Si}-$, silane in Figure 3d | Hybrid NPs | CD-PGEA | $10 \times 10^{-3} \text{ M DTT}$ | Scattered pieces after 7 days | In vivo | Chem/gene therapy | [166] |

2 days. In addition, PEGylation slowed down the release rate of the Gd chelates with a $t_{1/2}$ of 18 h due to steric hindrance caused by the PEG. PSQ NPs modified with anisamide-PEG chains exhibited higher biocompatibility, more uptake of NPs into cancer cells (targeted to sigma receptors) and enhanced T_1 -weighted magnetic resonance imaging (MRI) signal.^[110] For NPs with disulfide-bridged porphyrin, only <10% of the porphyrin derivative was released without reducing agents, while the addition of $10 \times 10^{-3} \text{ M DTT}$ resulted in the quick release: 25% release after 1 h, 50% after 23 h, and >80% after 96 h.^[111] Furthermore, these NPs were completely degraded after incubation in $10 \times 10^{-3} \text{ M DTT}$ for 8 days. Phototoxicity experiments demonstrated that the redox-responsive NPs led to more noticeable decrease of HeLa cell viability than the nonresponsive NPs as a control.^[111]

3.2. Mesoporous Organosilica Nanoparticles

After ethene- and disulfide nanorods and nanospheres were stirred in PBS solution (pH 7.4) with $6 \times 10^{-6} \text{ M}$ of ME (to mimic the extracellular GSH concentration) at 37°C for 48 h, their hydrodynamic sizes showed a little decrease alongside the appearance of a few fragments with sizes of 60–70 nm. In contrast, when dispersed in $2 \times 10^{-3} \text{ M}$ of ME to mimic intracellular GSH concentration, faster and greater size decrease was observed, indicating more pronounced degradation.

Furthermore, these nanospheres and nanorods, and their pre-degraded products appeared to be non-cytotoxic even at high particle concentrations up to $125 \mu\text{g mL}^{-1}$. DOX-loaded MONs could efficiently kill MCF-7 cells with $\approx 12\%$ of cell survival at $1 \mu\text{g mL}^{-1}$ of DOX.^[127] After disulfide-bridged MONs containing dye molecule (0.1 mg mL^{-1}) were stirred in PBS solution (pH 7.4) in the presence of $10 \times 10^{-3} \text{ M GSH}$ at 37°C for 0–7 days, a time-dependent structural breakdown was observed by TEM (Figure 15b), which was also confirmed by the cumulative increase of the photoluminescence emission signal of the supernatant as well as the appearance of small fragments in the supernatant (DLS data).^[132] These MONs were found to be biocompatible toward glioma C6 cells. The partial degradation could also be observed by TEM images inside glioma C6 cancer cells after 2 days of incubation, which was further confirmed by the detection of Si in the collected culture medium. Furthermore, RGD peptide-modified MONs could increase their cellular uptake, without affecting their GSH-triggered structural degradation. Moreover, the temozolomide-loaded MONs exhibited an enhanced efficiency to kill cancer cells in vitro.^[132] Moghaddam et al. found that the degradation kinetics in $8 \times 10^{-3} \text{ M GSH}$ were affected by both porosity and composition of the core. The 108 nm MONs exhibited the highest degradation rate among all the five NPs studied. TEM images showed that nonporous NPs underwent surface erosion, while MONs underwent both surface and bulk erosion in the reducing environment. This was also proved by

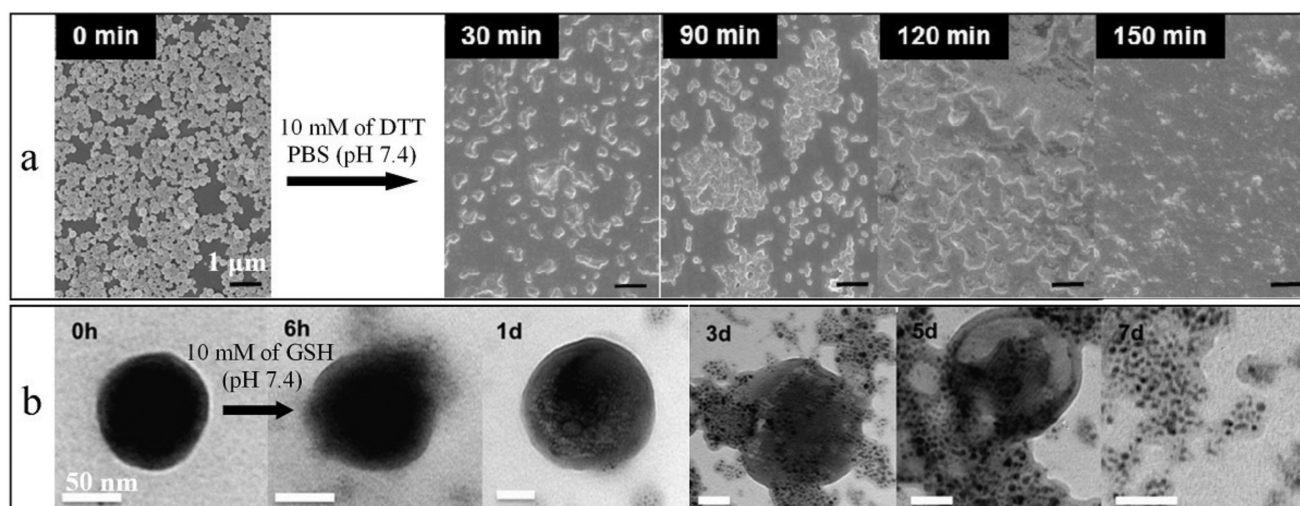


Figure 15. a) SEM images of NPs with bis(propylamide-ethyl)disulfide-bridged scaffold treated by $10 \times 10^{-3} \text{ M}$ of DTT for varied time. Reproduced with permission.^[109] Copyright 2015, Elsevier. b) TEM analysis of a suspension of disulfide-bridged MONs (0.1 mg mL^{-1} , PBS, 37°C) with $10 \times 10^{-3} \text{ M GSH}$ after incubation for different time. Reproduced with permission.^[132] Copyright 2016, The Royal Society of Chemistry.

the amount of silicon released and the GSH consumption, based on ICP-mass spectrometry (MS) data and GSH-orthophthalaldehyde (OPA) assays. All these NPs did not show cytotoxic effects in RAW 264.7 macrophages at concentrations lower than $125 \mu\text{g mL}^{-1}$, but had IC_{50} values ranging from 233 ± 42 up to $705 \pm 17 \mu\text{g mL}^{-1}$. Here, 108 nm MONs exhibited a higher degradation rate in response to GSH and a lower cytotoxicity. The degradation products of these NPs collected within 15 days showed over 85% cell viability (i.e., low cytotoxicity) in the same macrophage cell line after 24 h of incubation. In addition, the presence of $8 \times 10^{-3} \text{ M}$ GSH caused faster DOX release.^[128]

As shown in **Figure 16**, after DMONs with large pores were incubated in serum solutions containing $1 \times 10^{-3} \text{ M}$ GSH solution for 24 and 48 h, only partially collapsed structures were observed, while the structure completely degraded into small debris with sizes of about 35 nm after incubation in serum solution with $10 \times 10^{-3} \text{ M}$ GSH for a period of 48 h. In contrast, for MONs with small pores, only partially damaged structures were found in 1×10^{-3} and $10 \times 10^{-3} \text{ M}$ GSH at 24 and 48 h. The results were further corroborated by DLS, the oxidized GSH concentration, and the amount of generated $-\text{SH}$. The intracellular degradability results showed that the structure of polyethylenimine (PEI)-modified DMONs was completely

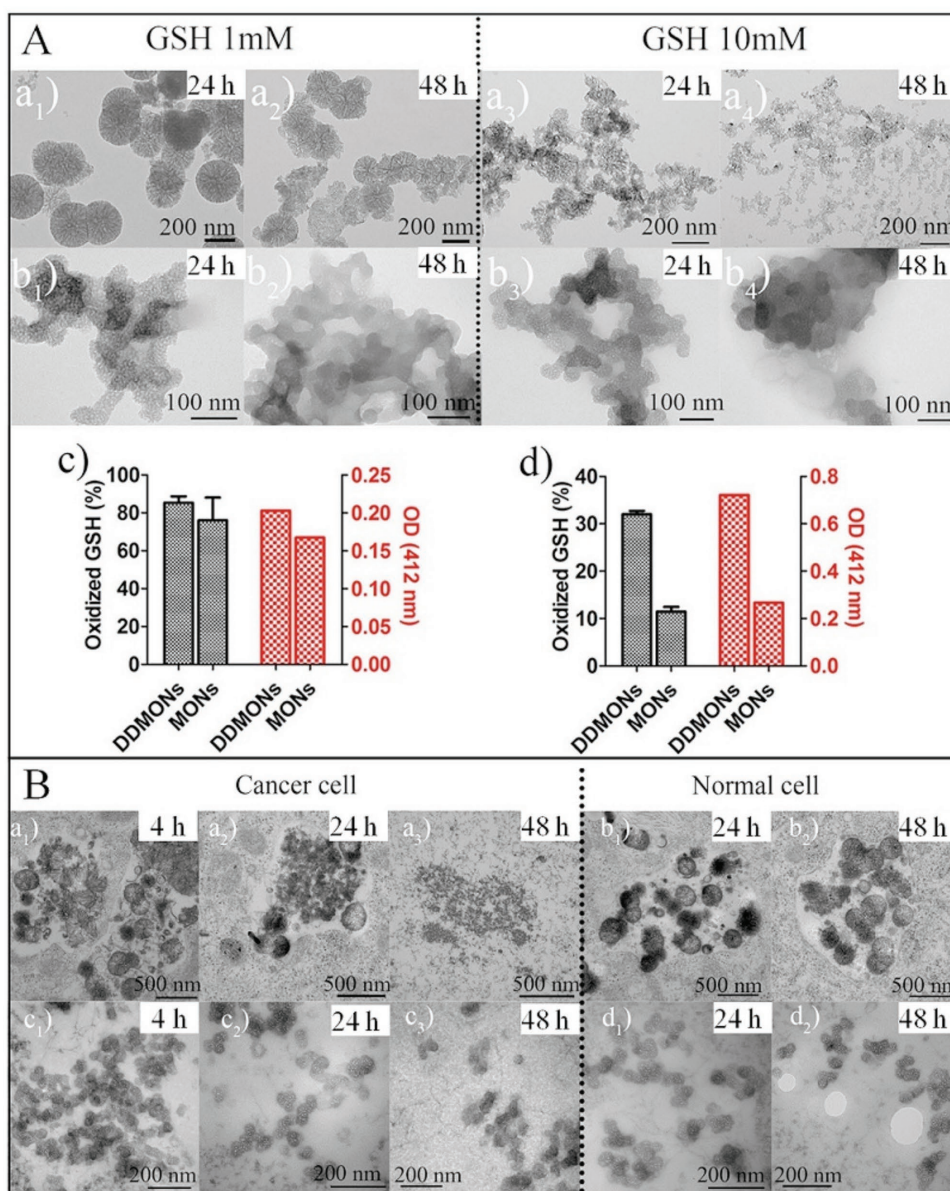


Figure 16. A) TEM images of a₁–a₄) DMONs with large pores and b₁–b₄) MONs with small pores tested at 1 and $10 \times 10^{-3} \text{ M}$ GSH solutions for different times. GSH oxidation percentage and relative quantity of $-\text{SH}$ groups (optical density (OD)) after incubation of DMONs or MONs in c) 1 M and d) $10 \times 10^{-3} \text{ M}$ GSH solution for 48 h. B) Bio-TEM images of ultrathin sections of a₁–a₃, b₁–b₂) DMONs–PEI with large pores and c₁–c₃, d₁, d₂) MONs–PEI with small pores after incubation with a₁–a₃, c₁–c₃) B16F0 cancer cell and b₁, b₂, d₁, d₂) HEK293t normal cells for different times. Reproduced with permission.^[140] Copyright 2016, American Chemical Society.

disintegrated into aggregated fragments after 48 h in B16F0 melanoma cancer cells. In comparison, the degradation of DMONs-PEI after incubation with HEK293t normal cells was obviously inhibited owing to the lower GSH concentration in normal human cells. In contrast to DMONs-PEI, MONs-PEI without disulfide introduction in both cell lines demonstrated no significant degradation even after 48 h of incubation. In addition, more than 80% cell survival of both cancer cell and normal cell was maintained after incubation of DMONs-PEI and MONs-PEI for 24 and 48 h when the particle concentrations were of $<40 \mu\text{g mL}^{-1}$. The higher GSH concentration led to faster release of loaded RNase A modified with *cis*-aconitic anhydride (RNase A-Aco) from DMONs-PEI, reaching $\approx 97\%$ in $10 \times 10^{-3} \text{ M}$ GSH at 48 h. Furthermore, DMONs-PEI/RNase A-Aco complexes exhibited higher cytotoxicity than that of nondegradable DMONs-PEI/RNase A-Aco toward B16F0 cancer cells, which might be essentially ascribed to quick GSH-triggered intracellular release.^[140] Chen and co-workers reported that after immersing disulfide-bridged MONs and traditional MSNs with similar worm-like mesopores and particle size ($\approx 40 \text{ nm}$) in SBF solutions with varied GSH concentrations, MONs in SBF solution with $10 \times 10^{-3} \text{ M}$ GSH became irregular and fragmented after 24 h and totally degraded into fragments of $\approx 5 \text{ nm}$ in size after 7 days, which made renal excretion possible, while MONs in pure SBF solution exhibited much decreased structure deterioration in the same periods. However, MSNs showed only slight degradation after 7 days of incubation in either pure or GSH-containing SBFs. DLS and ICP data show a similar trend. The degradation study of MONs in Hep G2 cells displayed that MONs became rough and vague at the particle edges after 1 day of co-incubation, began to disintegrate after 2 and 3 days, and most were completely degraded into small fragments after 7 days of incubation. In addition, MONs and PEG-modified MONs (PEG-MONs) showed low cytotoxicity, and high in vivo biocompatibility and biosafety. Moreover, PEG-MONs could deliver DOX into cells, more efficiently kill the tumor cells than free-DOX, and remarkably inhibit tumor growth. Most importantly, the organs of mice treated by PEG-MONs@DOX were mostly undamaged, while the organs (especially heart) of the mice treated with free-DOX were injured.^[136] The morphology of disulfide-bridged MONs evolved slightly to be less rough and less dense after treatment with $10 \times 10^{-3} \text{ M}$ GSH for a week.^[133] The merely partial decomposition might result from the high condensation degree caused by the high-temperature reaction implemented.^[133]

3.3. Core-Shell, Yolk-Shell, and Hollow Mesoporous Organosilica Nanoparticles

For disulfide-bridged yolk-shell MONs,^[129–131,143,145] higher GSH concentrations led to quicker DOX release due to GSH-triggered breakage of disulfide bonds, which further destroyed the hydrophobic interaction between DOX and the framework. However, 24 h of treatment in PBS solution with $10 \times 10^{-3} \text{ M}$ GSH just slightly changed the shape and caused indistinct edges,^[143] while more than 2 weeks resulted in the obvious breakdown of the yolk-shell structure.^[131] The slow

biodegradation might be attributed to high-framework condensation (caused again by hydrothermal synthesis treatment) and the low content of disulfide bonds. Moreover, these MONs were found to exhibit low cytotoxicity, good blood hemocompatibility, and histocompatibility. Both MONs modified with anti-Her2 affibody molecule for the specific recognition of Her2 expressed in tumor cells and MONs modified with acidic pH insertion peptide for targeting tumor acidic microenvironment exhibited enhanced cancer cell killing capacity in vitro and tumor inhibition in vivo in mice.^[130,143] In another example, CuS-doped yolk-shell MONs showed complete tumor growth suppression without recurrence toward U87MG tumor-bearing mice owing to mild hyperthermia-improved chemotherapy.^[131] Most disulfide-bridged, FITC-containing, and PEG-modified HONs (HONs-4S-FITC@PEG) appeared to be damaged and collapsed completely into fragments with $5 \times 10^{-3} \text{ M}$ DTT, while $10 \times 10^{-3} \text{ M}$ GSH caused a few ($\approx 20\%$) cracked hollow nanospheres, and the outline of uncracked nanospheres ($\approx 80\%$) became blurred, and many small species ($\leq 6 \text{ nm}$) appeared. DLS and drug release data revealed a similar degradation situation.^[154] In the collected cell culture medium, higher Si content was detected by inductively coupled plasma atomic emission spectrometry (ICP-AES). Both HONs-4S-FITC and HONs-4S-FITC@PEG showed low cytotoxicity ($>85\%$ viability) at a particle concentration of below $200 \mu\text{g mL}^{-1}$. Furthermore, HONs-4S-FITC@PEG could efficiently deliver DOX into A549 cells and reduce cell viability.^[154] After disulfide-bridged HONs were suspended in PBS solution ($50 \times 10^{-3} \text{ M}$, pH 7.4) with $20 \times 10^{-3} \text{ M}$ GSH, the hollow structure began to partly break in the early times, eventually resulting in complete fragmentation after 48 h. HONs indicated a hemolytic activity as low as 2.3% even at high particle concentrations of up to $400 \mu\text{g mL}^{-1}$. Moreover, HONs were non-cytotoxic for TCA8113 cells (cell viability $> 87\%$) at a particle concentration of up to $100 \mu\text{g mL}^{-1}$, while DOX-loaded HONs could achieve $\approx 75\%$ of a cell-killing ratio at a DOX concentration of $10 \mu\text{g mL}^{-1}$.^[155] Disulfide-bridged HMons exhibited a time-dependent biodegradation behavior in $10 \times 10^{-3} \text{ M}$ GSH solutions and almost all HMons were degraded within 30 days. Over 95% of U87MG cells stayed alive after incubation with HMons without surface modification for 24 h. Histological analysis showed no noticeable abnormality in the major organs of healthy female BALB/c nude mice after 30 days of intravenous injection of HMons (10 mg mL^{-1}), indicating the relatively high biocompatibility and biosafety of HMons in vivo. After modification with glucose oxidase for glucose oxidization and loading with L-arginine for producing nitric oxide (NO), the constructed systems remarkably eliminated the tumors of U87 tumor-bearing mice, suggesting synergistic cancer starving-like functionality and gas therapy.^[152]

Shi and co-workers reported that disulfide- and benzene-bridged HMons (particle concentration: 0.5 mg mL^{-1}) displayed a gradual biodegradation behavior from the initial hollow spheres to fragments after being stirred in SBF solution with $10 \times 10^{-3} \text{ M}$ GSH for 4 days. Concomitantly, the triggered degradation resulted in 69% of DOX release at 24 h, which was much higher than that in pure PBS solution (only 20%). Interestingly, the introduction of the $-(\text{CH}_2)_3-\text{S}_4-(\text{CH}_2)_3-$ chain improved the in vitro ultrasound (US) imaging performance of HMons. Significantly, the DOX-loaded HMons showed an

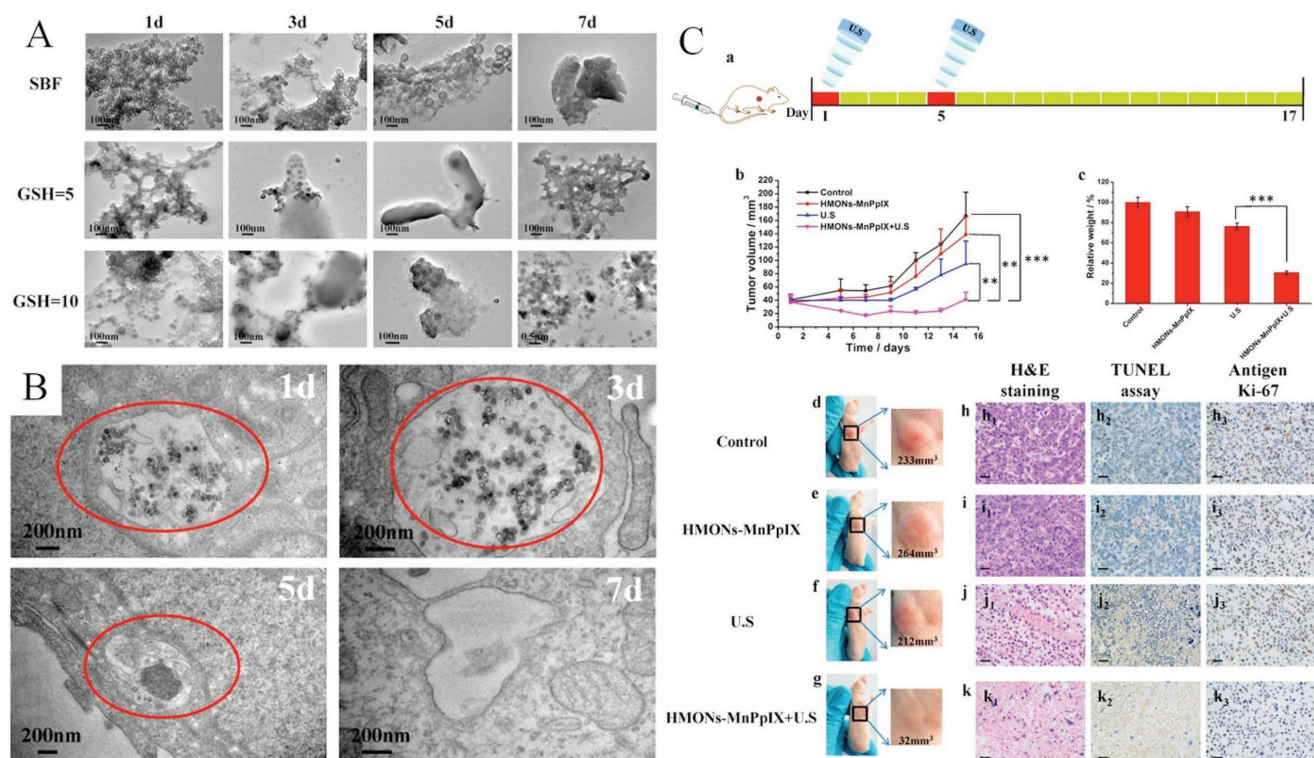


Figure 17. A) TEM images of HMONS–MnPpIX–PEG (0.1 mg mL^{-1}) in SBF solutions with varied GSH concentrations for different incubation times. B) Bio-TEM images of ultrathin sections after co-incubation HMONS–MnPpIX–PEG with 4T1 cells for varied time. C) a) Protocol of SDT on mice tumor xenograft. Changes of b) tumor volume and c) tumor weights after varied treatments of control group, HMONS–MnPpIX–PEG group, US only group, and HMONS–MnPpIX–PEG + US group. d–g) Digital images of tumor obtained at the end of treatments. h–k) Optical microscopic images of tumor sections. Reproduced with permission.^[148] Copyright 2017, American Chemical Society.

enhanced cancer cell-killing capacity in vitro and an improved antitumor chemotherapeutic efficiency on female BALB/c nude mice with tumors on the right mammary gland compared with free DOX.^[147] They also found that after disulfide-bridged HMONS^[149] and large pore-size HMONS^[139] (particle concentration: 0.1 mg mL^{-1}) were suspended in SBF solution with $10 \times 10^{-3} \text{ M}$ GSH and stirred for 14 days, almost no intact NPs could be detected, indicating facile biodegradation behavior in a reducing microenvironment. Careful intracellular observations revealed a time-dependent biodegradation behavior in breast cancer 4T1 cell line: collapsed HMONS after 2 days, more significant biodegradation after 3 days, and only very few collapsed HMONS after 7 days.^[149] Both large pore-size HMONS and PEG modified HMONS (i.e., HMONS@PEG) showed negligible cytotoxicity against 4T1 cells at a high particle concentration up to $160 \text{ } \mu\text{g mL}^{-1}$; however, DOX-loaded HMONS@PEG killed $\approx 85\%$ cells after treatment with a DOX concentration of $30 \text{ } \mu\text{g mL}^{-1}$ for 48 h, and the large pore-size HMONS exhibited a high killing capacity ($\approx 61\%$ vs 22%) against 4T1 cancer cells as compared to free protein drugs due to their high loading capacity ($323.0 \text{ } \mu\text{g mg}^{-1}$) for large RNase A proteins and efficient cellular uptake. An in vivo biocompatibility test revealed that the blood indices and body weight showed no obvious variation compared with the control group after intravenous administration of large pore-size HMONS and HMONS@PEG into healthy Kunming mice ($5, 10$, and 20 mg kg^{-1}) and further feeding for 30 days. The injected HMONS@PEG mainly accumulated

into liver and spleen, and the major organs showed no prominent pathological changes. The antitumor in vivo results revealed that DOX-loaded HMONS@PEG had decreased drug toxic side effects against normal organs; however, an improved tumor-inhibition effect was observed compared with free DOX at the dose of 5 mg kg^{-1} .^[149] They also grafted the organic sonosensitizer (protoporphyrin, PpIX) onto the mesopore surface of disulfide-bridged HMONS, then chelated paramagnetic Mn ions and finally modified PEG to form HMONS–MnPpIX–PEG for MRI-guided sonodynamic therapy (SDT) against cancer. As shown in Figure 17a, HMONS–MnPpIX–PEG still maintained their intact spherical structure after being stirred in SBF solution without GSH at 37°C for 1 day. However, they underwent a moderate biodegradation after extended incubation time up to 7 days. In contrast, they suffered a severe biodegradation in SBF solution with $5 \times 10^{-3} \text{ M}$ GSH over the same period, and the higher $10 \times 10^{-3} \text{ M}$ GSH condition caused a more serious biodegradation.^[148] After co-incubation with 4T1 cells for different times, HMONS–MnPpIX–PEG exhibited time-dependent biodegradation behavior in the intracellular microenvironment (Figure 17b), as follows: maintained hollow nanostructure after 1 day, partial degradation after 3 days, a large extent of degradation after 5 days, and almost complete degradation after 7 days. Intracellular Si content decreased with the extension of co-incubation time with 4T1 cells from 1 to 7 days. Facile excretion out of the mice body was found after the intravenous administration of HMONS–MnPpIX–PEG for 48 h. Importantly, the

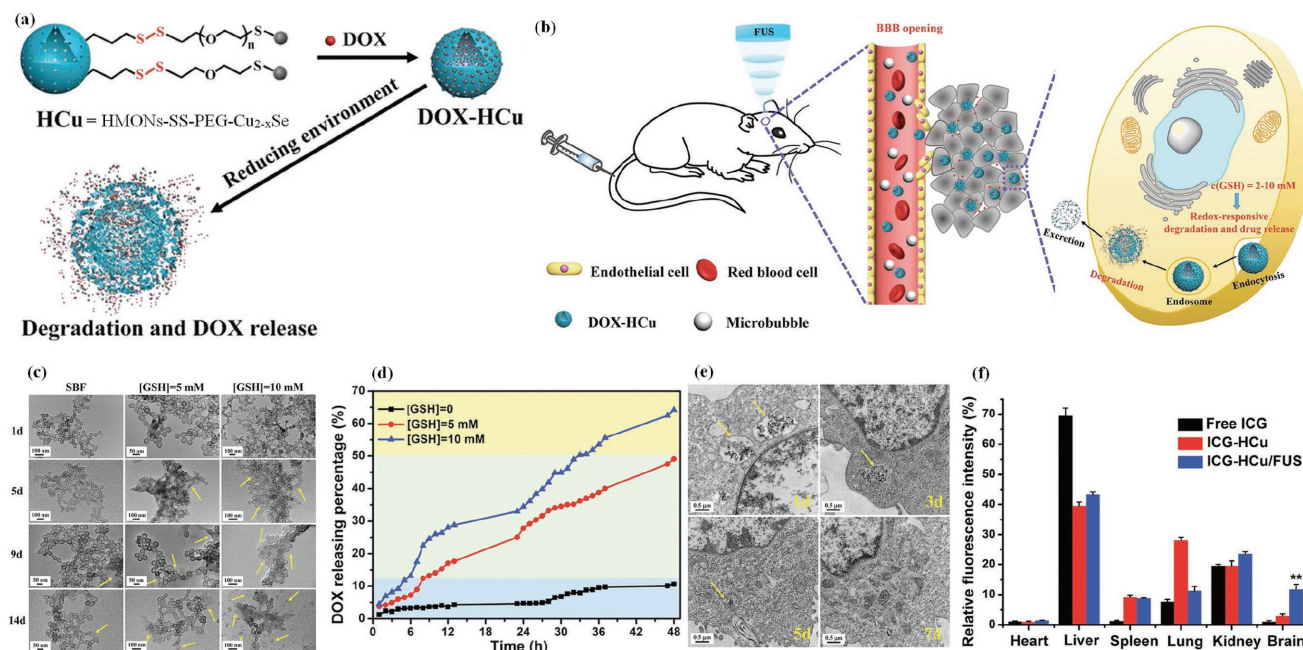


Figure 18. Schematic illustration of a) DOX-HCu nanosystems and GSH-triggered degradation and drug-releasing behavior, and b) the enhanced delivery of DOX-HCu nanosystems into brain tumor via FUS-induced blood-brain barrier (BBB) opening, and subsequent intracellular GSH-triggered biodegradation of DOX-HCu and excretion. c) TEM images of HCu in SBF solutions with varied GSH concentrations for different durations. d) The releasing profiles of DOX from DOX-HCu in SBF solutions with different GSH concentrations. e) Bio-TEM images of ultrathin sections after co-incubation HCu with U87 glioma cells for varied durations. f) The quantified relative fluorescence intensity in different organs of U87 glioma-bearing mice after being administrated with free indocyanine green (ICG), ICG-HCu, and ICG-HCu/FUS. Reproduced with permission.^[150] Copyright 2018, Wiley-VCH.

authors reported that HMOns-MnPpIX-PEG had high in vivo biocompatibility for healthy female Kunming mice, and efficiently inhibited the tumor growth of 4T1 tumor xenograft in nude mice by MRI-guided SDT combined with US therapy (Figure 17c,d).^[148]

Zheng and co-workers constructed a smart nanosystem with photoacoustic (PA) imaging, tumor-specific GSH-triggered biodegradability, and drug release for glioblastoma multiforme (GBM) treatment in combination with focused US (FUS), by decorating small Cu_{2-x}Se NPs on the surface of disulfide-bridged HMOns via a disulfide and PEG linker (HMOns-ss-PEG-Cu_{2-x}Se, designated as HCu) (Figure 18a,b).^[150] HCu could keep the relatively intact structure in pure SBF solution for 14 days, while structural collapse of HCu could be observed in SBF solutions with 5×10^{-3} and 10×10^{-3} M GSH (Figure 18c). In the meantime, the releasing amount of DOX after 48 h was only 10.6% in pure SBF solution, which increased to 49.1% and 64.2% in SBF solutions with 5×10^{-3} and 10×10^{-3} M GSH, respectively (Figure 18d). HCu nanosystems showed no significant cytotoxicity against U87 glioma cells even at a high concentration of $400 \mu\text{g mL}^{-1}$ in 48 h and high histo- and hemocompatibility. The intracellular biodegradation test showed that the endocytosed HCu nanosystems by U87 glioma cells could maintain their intact structure after 1 day of co-incubation. Then, partial NPs were degraded after 3 days. With the co-culture time prolonged to 5 days, more NPs would be degraded and a few NPs could be observed after 7 days of co-culture (Figure 18e). Based on FUS-induced opening of the blood-brain barrier (BBB), HCu nanosystems achieved brain tumor PA imaging with significant contrast

enhancement, greatly improved accumulation in the targeted brain regions (Figure 18f), and enhanced antiglioma efficacy. Lu et al. utilized disulfide-bridged HMOns as a platform to construct multifunctional oxygen-carrying nanotheranostics (HMOns-⁶⁴CuS-PEG) by the loading of O₂-saturated perfluoropentane (PFP) in the hollow cavity, and the modification of ⁶⁴CuS NPs and PEG on the particle surface (Figure 19A).^[151] HMOns-⁶⁴CuS-PEG was gradually degraded in 10×10^{-3} M GSH solutions, and the particles were completely converted into floccules after 3 weeks of immersion (Figure 19B). Through the assistance of PFP gasification resulting from NIR laser-triggered mild hyperthermia, simultaneous multimodality imaging of PA, PET, and US, and rapid oxygen diffusion across the tumor could be achieved for efficient radiotherapy toward mice bearing U87MG tumors (Figure 19C).

3.4. Nanocomposites

The disulfide-bridged organosilica shell broke partially and collapsed NPs were formed after being treated by a high DTT (100×10^{-3} M) concentration for 1 week. In parallel, these hybrid NPs displayed a much higher ($\approx 80\%$) pyrene release than that ($<40\%$) of NPs with a pure silica shell.^[158] After being treated in a solution with 5×10^{-3} M GSH for 24 h, nanocapsules with CS-RhB macromolecules as a core and disulfide- and ethene-bridged organosilicas as a shell were completely disintegrated into small fragments, and simultaneously caused 41% of CS-RhB release.^[159] In contrast, in a solution without GSH, the shell structure remained intact and only

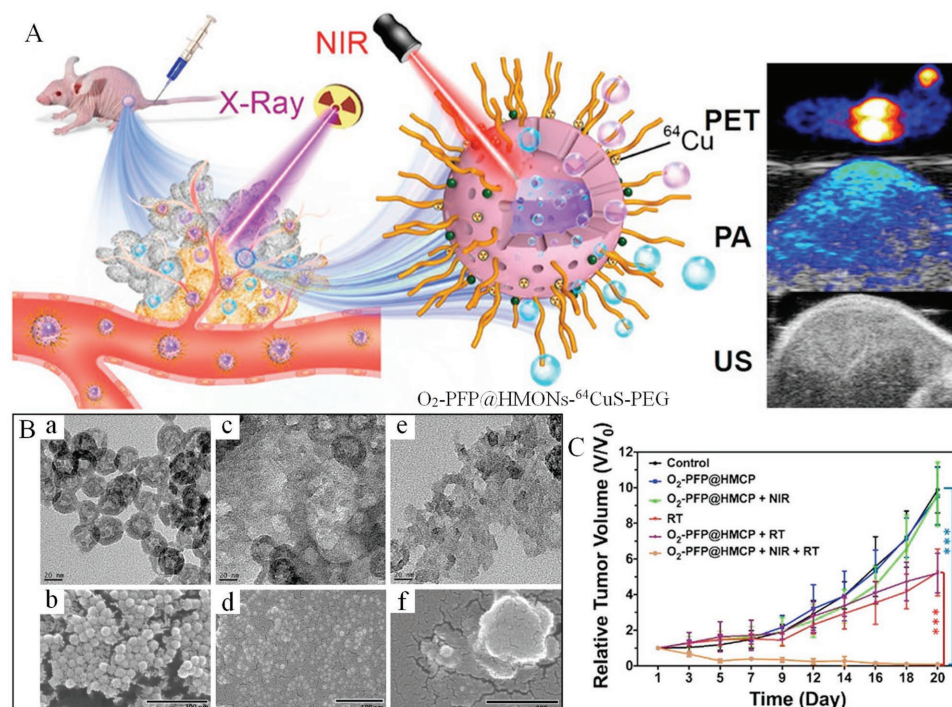


Figure 19. A) Schematic illustration of the construction of $O_2\text{-PFP@HMons-}^{64}\text{CuS-PEG}$ for PET, PA, and US imaging, mild hyperthermia-induced PFP bubble release, and oxygen-sensitized radiotherapy. B) TEM images of $HMons-^{64}\text{CuS-PEG}$ immersed in 10×10^{-3} M GSH aqueous solution for a,b) 3 days, c,d) 2 weeks, and e,f) 3 weeks. C) Tumor growth curves of mice bearing U87MG tumors subjected to various treatments. Reprinted with permission.^[151] Copyright 2018, American Chemical Society.

7.3% of CS-RhB was released. Even at a high concentration of $200 \mu\text{g mL}^{-1}$, the cell viability was over 80% in HeLa cancer and COS7 normal cell lines. In addition, based on differences of fluorescence intensity, it was deduced that the nanocapsules could not efficiently release CS-RhB into COS7 normal cells, but specifically release them into HeLa cancer cells, due to difference in GSH concentrations.^[159] When $(\text{PAH/PSS})_4$ microcapsules coated with disulfide-bridged organosilica shell were stirred at 37°C in PBS solution (pH 7.4) with 20×10^{-3} M GSH, hollow capsules began to break after 6 h, and were degraded into broken capsules and small fragments after 24 h. These capsules exhibited an inappreciable toxic effect on both HeLa cells and normal human mesenchymal stem cells (MSCs). DOX-loaded capsules killed $\approx 88\%$ of HeLa cells at a DOX concentration of $30 \mu\text{g mL}^{-1}$; however, they only caused the death of $\approx 20\%$ MSCs, which may be ascribed to the difference of GSH concentrations between cancer and normal cells.^[160] After folic acid (FA)-PEG modified DOX and MgPc HNPs consisting of a disulfide-bridged shell ($560 \mu\text{g mL}^{-1}$) were immersed in water with 10×10^{-3} M GSH, the shell framework was deformed, along with a GSH-responsive DOX release. Moreover, the combined stimulation of GSH and light caused the collapse of the hollow structure. There was an almost 100% survival rate of HeLa cells after incubated with the MgPc-HNPs-PEG-FA at a particle concentration of $<600 \mu\text{g mL}^{-1}$ for 24 h. DOX& MgPc-HNPs-PEG-FA revealed enhanced inhibition of tumor growth in tumor-bearing mice by the trimodal therapy of chem-, photodynamic therapy (PDT), and photothermal therapy (PTT).^[108]

After stirring in PBS solution (pH 7.4) with 10×10^{-3} M DTT at 37°C for varied times, disulfide-bridged and DOX-embedded hybrid NPs underwent time-dependent degradation starting from the particle surface, as follows: a rougher surface after 1 day, broken NPs after 4 days, and some scattered pieces after 7 days.^[166] In contrast, disulfide-bridged NPs without embedded DOX were degraded from the interior of NPs: a hollow structure after 1 day and a thinner shell after 4 days. This behavior might originate from the aggregation of the disulfide-bridged silane shown in Figure 3d, which served as nuclei for the growth of organosilica with a low content of disulfide bonds. In vivo degradation was further performed to exploit the excretion situation by detecting Si amounts in urine of mice after intravenous injection. Significantly higher excreted Si amounts via urine were found in the mice group of DOX-embedded NPs, compared with conventional silica- and disulfide-bridged NPs without DOX. This faster excretion was probably ascribed to the faster in vivo redox-triggered biodegradation property. After modified with polycation (β -cyclodextrin-poly(glycidyl methacrylate, CD-PGEA) for gene loading, the constructed system could achieve gene and drug co-delivery in vitro and in vivo, and remarkably suppress the tumor growth by applying a complementary gene- and chemotherapy.^[166]

For a PEI-modified disulfide-bridged shell with large radial mesopores on the surface of a conventional MSNs core, after incubation at 37°C for 6 h, the release of the entrapped small interfering ribonucleic acid (siRNA) in 10×10^{-3} M GSH was much faster than that in the absence of GSH. The loaded DOX in the MSNs core also showed a GSH concentration-dependent release behavior. Histological analyses displayed that no obvious

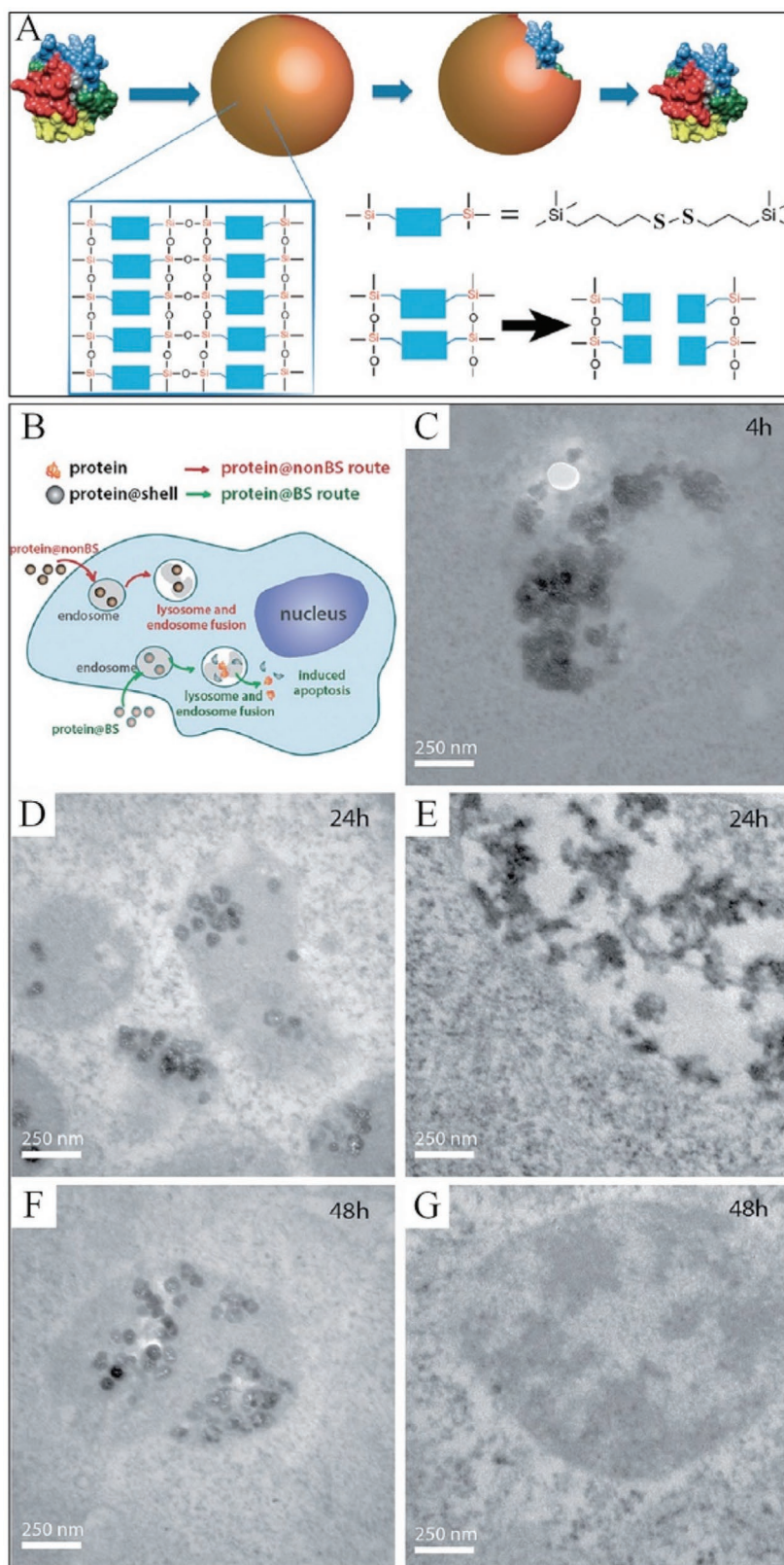


Figure 20. Schematic illustration of A) synthesis of the GSH-sensitive hybrid capsules by coating the protein cargo with disulfide-bridged organosilica network and B) internalization and possible intracellular degradation of protein@breakable silica (BS) and protein@nonBS. Bio-TEM images of C,E,G) internalized protein@BS and D,F) protein@nonBS in C6 glioma cells after incubated for different time. Reprinted with permission.^[161] Copyright 2016, Wiley-VCH.

damage was found in the MCF-7/adriamycin-resistant (ADR) tumor-bearing mice. In vitro and in vivo experiments indicated that such a co-delivery system could inhibit multidrug resistance (MDR) tumor growth.^[138] For Au NPs with a thin layer of disulfide-bridged organosilica, high intracellular GSH levels ($\approx 1\text{--}10 \times 10^{-3} \text{ M}$) were able to trigger the decomposition of the thin disulfide-bridged organosilica shell, leading to a rapid release of fluorescent molecules and correspondingly rapid recovery of the fluorescence signal from the quenching state.^[163]

Over 90% of cytochrome C was released from the broken capsules with disulfide-bridged organosilica frameworks after being dispersed in $5 \times 10^{-3} \text{ M}$ GSH for 48 h. After incubation in living C6 glioma cells for 48 h, TEM images showed that the organosilica shell was completely destroyed (**Figure 20**). Instead of cytochrome C, the intracellular response release of onconase resulted in the 40% drop of cell viability, suggesting its retained activity.^[161]

Tumor intracellular redox-triggered degradation of disulfide-bridged organosilica frameworks may also be useful in fluorescent detection. For example, when many fluorescent NPs, such as CDs, were encapsulated into one nanocapsule, it could cause severe fluorescence quenching. After the disulfide-bridged organosilica shell was totally degraded by reduction with NaBH_4 (1 mg mL^{-1}) for 30 min, CDs were released from CDs@DONs and the fluorescence intensity was increased 2.1 times.^[162] Furthermore, when CDs@DONs were applied in the detection of pathogenic bacteria, the fluorescent signal was amplified by two orders of magnitude, compared with that using more conventional CDs as fluorescent label.^[162] This fluorescence recovery was also found in a core-shell nanosystem with a CS-RhB core and a disulfide@ethene-bridged organosilica shell. The distance among RhB groups was too short to cause self-quenching. After the complete degradation of the organosilica shell, the fluorescence intensity was three times higher than that of the intact nanocapsules.^[159] Furthermore, this phenomenon of fluorescence recovery was also observed in HeLa cancer cells, however, not in COS7 normal cells, indirectly detecting a GSH-triggered degradation process of the organosilica nanocapsules and the concomitant drug release.^[159] This design strategy may be promising to construct advanced tracking and imaging nanosystems for sensitive and specific diagnosis of cancer owing to the high intracellular GSH concentration in cancer cells.^[173,174]

Thus, it may be a simple, available, and promising method to construct various nanosystems by in situ encapsulating/introducing single or multiple active cargos (drugs, proteins, genes, fluorescent molecules, functional solid cores, etc.) within a redox-triggered biodegradable organosilica shell/matrix,^[108,138,158–166,175] compared to postsynthesis loading.

In short, compared with similar counterparts, most disulfide-bridged silsesquioxane frameworks exhibited redox-triggered and time-dependent biodegradation in physiological solutions containing reducing agents (Table 3), along with adequate responsive cargo release. However, these hybrid NPs exhibited different degradation rates, which are dependent on the interior

(composition and structure) and exterior (environment and condition) parameters. It is possible to regulate the redox-triggered degradation rates and the concomitant cargo release profiles by controlling the condensation degree of the organosilica matrix, the disulfide bond content (through varying the disulfide-bridge silane/TEOS ratio), the particle structure (pore size, shell thickness, particle size, pore wall thickness, etc.), and particle surface functionalizations, as shown in **Figure 21**. A lot of recent experimental results in a rapidly increasing number of papers indicate that a low condensation degree, high content of disulfide bond, large pore size, thin shell thickness, etc. will result in faster degradation rates. Hydrothermal reaction at elevated temperature usually leads to higher condensation degree of $-\text{Si}-\text{O}-\text{Si}-$, which slows down the hydrolytic degradation rate. In addition, suitable surface functionalization can improve the stability in blood circulation and tumor targeting, yet preserving the GSH-triggered degradation behavior. Intracellular-enhanced degradation behaviors were also discussed in a few reports (Table 3); however, there were a few investigations and assessments concerning degradation behaviors in vivo (e.g., in mice).^[148,166] For the effect of enhanced degradation on excretion, much higher Si amounts were detected in the collected cell culture media after co-incubating disulfide-bridged NPs with cancer cells over a certain period.^[132,148,154,166] Xu and co-workers found significantly higher excretion of Si amounts via urine in the mice group treated with DOX-embedded and disulfide-bridged NPs, compared with conventional silica NPs.^[166] Most disulfide-bridged NPs with and without modifications showed negligible indications of cytotoxicity, good hemocompatibility,^[107,130,134,136,148,150] and in vivo biocompatibility.^[130,136,138,139,143,147–150] Their degraded products were also found to have low cytotoxicity,^[109,127,128] however, the accurate characterizations of the degraded products are still urgently needed. The in vitro and in vivo biosafety of the degraded products should also be given much more attention. Moreover, based on disulfide-bridged silsesquioxane frameworks, various nanosystems were developed and exhibited efficient in vivo cancer diagnostic and/or therapeutic effect toward mice.^[108,129–131,134–138,143,147–152,155,165,166] In short, the rapid degradation rates (such as complete degradation within 2 days) can accelerate the release rate of loaded guest molecules and cause their complete release for better biological effects, also facilitating the quick excretion of degraded products, and improving the biosafety of the injected NPs.

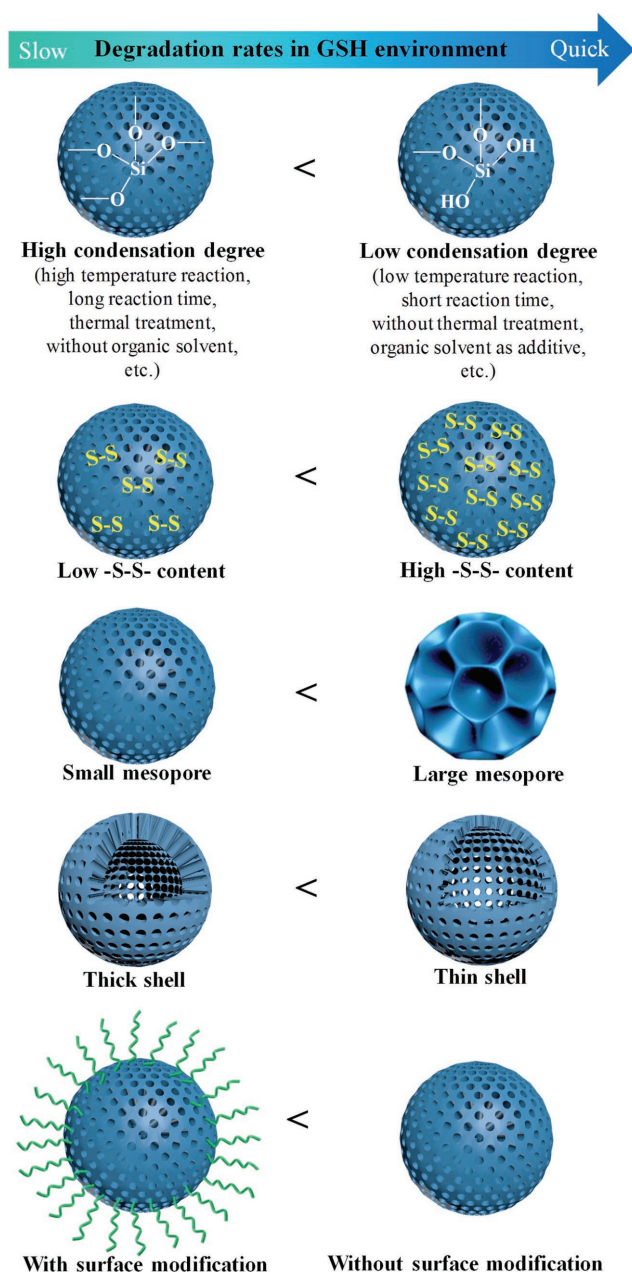


Figure 21. Schematic illustration of possible strategies for regulating the degradation rates of disulfide-bridged NPs in the GSH environment.

4. Conclusions and Outlook

An increasing number of studies have recently focused on exploring various disulfide-bridged organosilica frameworks. These contributions revealed that the introduction of disulfide bonds into the silica framework can not only maintain high structural stability in physiological conditions, but also achieve an interesting responsive biodegradation behavior and associated cargo release, specific to the disulfide-bridged systems, which are triggered by the intracellular reducing microenvironment in living cells. This is occurring especially in cancer cells; thus, it becomes particularly relevant for the improvement of

the cytosolic bioavailability and in vivo biosafety of silica-based nanotheranostics. Thus far, many disulfide-bridged hybrid NPs with different structures and S contents have been synthesized. However, it is still difficult to prepare NPs in a controlled manner with well-defined structures while maintaining the introduction of a high S content, due to the disturbing role of disulfide-bridged silane during the synthesis. As an emerging research field, there are still a lot of opportunities for the design and controlled fabrication of such nanomaterials, an example being in situ single or co-encapsulation of various active species (drug, gene, protein, fluorescent molecule, biocatalyst, Fe₃O₄ NPs, etc.) by disulfide-bridged organosilica shells for redox-triggered release.

Most hybrid NPs with disulfide-bridged silsesquioxane frameworks displayed redox-triggered and time-dependent biodegradation behavior in solutions, intracellular micro-environments, and mice (which are presented in only a few studies). Unfortunately, most studies did not provide the data about whether and how long these disulfide-bridged organosilicas could be completely degraded and what exactly were the degraded products. Therefore, the next steps should be concerned with achieving elaborate regulation of the degradation profile, explore the optimized ones for specific nanobiomedical applications, and perform accurate characterization of the degraded products. In addition, the detailed and accurate mechanism of redox-triggered and hydrolysis-induced degradation needs further elucidation. Most disulfide-bridged hybrid NPs, with and without modifications, displayed good in vitro and in vivo biocompatibility, and importantly, a few constructed nanosystems showed efficient in vivo cancer diagnostic and/or therapeutic effects in the case of animal studies (e.g., mice). Nevertheless, in the near future, scientists should pay more attention to in vitro and in vivo biosafety of the partially and completely degraded products, and the effects of the improved degradation rates on in vivo clearance. Interestingly, the rapid intracellular GSH-triggered degradation and subsequent rapid in vivo clearance may increase tolerance threshold and dosage of silica-based nanotheranostics under repeated high dosage treatment. However, more experimental data are needed to establish this possibility. In addition, only preliminary biosafety evaluations were performed regarding these disulfide-bridged silsesquioxane-based frameworks. Therefore, it requires systematic and strict biosafety evaluations. In conclusion, owing to intracellular redox-triggered framework degradation and cargo release, good biocompatibility, versatile composition/structures, easy functionalizations, and excellent performance in theranostic biomedicine, it may be anticipated that these nanohybrids with disulfide-bridged organosilica framework could pave the way to improve diagnosis and treatment of diseases with higher in vivo biosafety in comparison to conventional MSNs.

Acknowledgements

This work was supported by National Natural Science Foundation of China (Grant Nos. 21501009 and 51671181), Fundamental Research Funds for the Central Universities (Grant Nos. 2302015-06500017, FRF-BR-17-032A, and FRF-BR-17-002B), Beijing Municipal Science

and Technology Commission (z131102002813058), and the Australian Research Council (ARC) through the Discovery Project programs (DP170104464, DP140104062 and DP160104866). F.K. thanks the University of Vienna for financial support. Mathew Doyle (University of Vienna) is acknowledged for proofreading the manuscript.

Conflict of Interest

The authors declare no conflict of interest.

Keywords

biocompatibility, disulfide-bridged silsesquioxane frameworks, mesoporous silica nanoparticles, nanobiomedicine, redox-triggered biodegradation

Received: December 17, 2017

Revised: March 22, 2018

Published online: April 25, 2018

- [1] E. K. Lim, T. Kim, S. Paik, S. Haam, Y. M. Huh, K. Lee, *Chem. Rev.* **2015**, 115, 327.
- [2] H. Chen, W. Zhang, G. Zhu, J. Xie, X. Chen, *Nat. Rev. Mater.* **2017**, 2, 17024.
- [3] A. Z. Wang, R. Langer, O. C. Farokhzad, *Annu. Rev. Med.* **2012**, 63, 185.
- [4] V. R. Devadasu, V. Bhardwaj, M. N. V. R. Kumar, *Chem. Rev.* **2013**, 113, 1686.
- [5] L. Y. T. Chou, K. Ming, W. C. W. Chan, *Chem. Soc. Rev.* **2011**, 40, 233.
- [6] M. Vallet-Regí, A. Rámila, R. P. del Real, J. Pérez-Pariente, *Chem. Mater.* **2001**, 13, 308.
- [7] R. K. Singh, K. D. Patel, K. W. Leong, H. W. Kim, *ACS Appl. Mater. Interfaces* **2017**, 9, 10309.
- [8] J. Zhu, Y. Niu, Y. Li, Y. Gong, H. Shi, Q. Huo, Y. Liu, Q. Xu, *J. Mater. Chem. B* **2017**, 5, 1339.
- [9] J. L. Paris, M. Colilla, I. Izquierdo-Barba, M. Manzano, M. Vallet-Regí, *J. Mater. Sci.* **2017**, 52, 8761.
- [10] J. G. Croissant, Y. Fatieiev, N. M. Khashab, *Adv. Mater.* **2017**, 29, 1604634.
- [11] X. Du, X. Li, L. Xiong, X. Zhang, F. Kleitz, S. Z. Qiao, *Biomaterials* **2016**, 91, 90.
- [12] Y. Chen, J. Shi, *Adv. Mater.* **2016**, 28, 3235.
- [13] J. G. Croissant, X. Cattoën, M. Wong Chi Man, J.-O. Durand, N. M. Khashab, *Nanoscale* **2015**, 7, 20318.
- [14] J. G. Croissant, Y. Fatieiev, A. Almalik, N. M. Khashab, *Adv. Healthcare Mater.* **2018**, 7, 1700831.
- [15] D. Niu, Y. Li, J. Shi, *Chem. Soc. Rev.* **2017**, 46, 569.
- [16] J. Wen, K. Yang, F. Liu, H. Li, Y. Xu, S. Sun, *Chem. Soc. Rev.* **2017**, 46, 6024.
- [17] J. Florek, R. Caillard, F. Kleitz, *Nanoscale* **2017**, 9, 15252.
- [18] S. S. Park, C. S. Ha, *Adv. Funct. Mater.* **2017**, 27, 1703814.
- [19] M. Yu, Z. Gu, T. Ottewill, C. Yu, *J. Mater. Chem. B* **2017**, 5, 3241.
- [20] K. Albert, X. C. Huang, H. Y. Hsua, *Adv. Colloid Interface Sci.* **2017**, 249, 272.
- [21] W. Q. Lim, S. Z. F. Phua, H. V. Xu, S. Sreejith, Y. Zhao, *Nanoscale* **2016**, 8, 12510.
- [22] Y. Yang, C. Yu, *Nanomedicine* **2016**, 12, 317.
- [23] K. S. Butler, P. N. Durfee, C. Theron, C. E. Ashley, E. C. Carnes, C. J. Brinker, *Small* **2016**, 12, 2173.
- [24] B. Rühle, P. Saint-Cricq, J. I. Zink, *ChemPhysChem* **2016**, 17, 1769.

- [25] Y. Zhang, B. Y. W. Hsu, C. Ren, X. Li, J. Wang, *Chem. Soc. Rev.* **2015**, 44, 315.
- [26] H. Mekaru, J. Lu, F. Tamanoi, *Adv. Drug Delivery Rev.* **2015**, 95, 40.
- [27] C. Argyo, V. Weiss, C. Brauchle, T. Bein, *Chem. Mater.* **2014**, 26, 435.
- [28] D. Şen Karaman, M. P. Sarparanta, J. M. Rosenholm, A. J. Airaksinen, *Adv. Mater.* **2018**, 30, 1703651.
- [29] M. Montalti, L. Prodi, E. Rampazzo, N. Zaccheroni, *Chem. Soc. Rev.* **2014**, 43, 4243.
- [30] X. Du, S. Z. Qiao, *Small* **2015**, 11, 392.
- [31] Z. Li, J. C. Barnes, A. Bosoy, J. F. Stoddart, J. I. Zink, *Chem. Soc. Rev.* **2012**, 41, 2590.
- [32] Q. He, J. Shi, *Adv. Mater.* **2014**, 26, 391.
- [33] Y. Chen, H. Chen, J. Shi, *Adv. Mater.* **2013**, 25, 3144.
- [34] S. Murugadoss, D. Lison, L. Godderis, S. V. D. Brule, J. Mast, F. Brassinne, N. Sebaihi, P. H. Hoet, *Arch. Toxicol.* **2017**, 91, 2967.
- [35] V. Mamaeva, C. Sahlgren, M. Lindén, *Adv. Drug Delivery Rev.* **2013**, 65, 689.
- [36] F. Tang, L. Li, D. Chen, *Adv. Mater.* **2012**, 24, 1504.
- [37] Y. S. Lin, K. R. Hurley, C. L. Haynes, *J. Phys. Chem. Lett.* **2012**, 3, 364.
- [38] M. Benezra, O. Penate-Medina, P. B. Zanzonico, D. Schaer, H. Ow, A. A. Burns, E. DeStanchina, V. Longo, E. Herz, S. Iyer, J. Wolchok, S. M. Larson, U. Wiesner, M. S. Bradbury, *J. Clin. Invest.* **2011**, 121, 2768.
- [39] R. Friedman, *J. Natl. Cancer Inst.* **2011**, 103, 1428.
- [40] K. Ma, C. Mendoza, M. Hanson, U. Werner-Zwanziger, J. Zwanziger, U. Wiesner, *Chem. Mater.* **2015**, 27, 4119.
- [41] K. Ma, D. Zhang, Y. Cong, U. Wiesner, *Chem. Mater.* **2016**, 28, 1537.
- [42] F. Chen, K. Ma, L. Zhang, B. Madajewski, P. Zanzonico, S. Sequeira, M. Gonen, U. Wiesner, M. S. Bradbury, *Chem. Mater.* **2017**, 29, 8269.
- [43] K. Ma, U. Wiesner, *Chem. Mater.* **2017**, 29, 6840.
- [44] F. Chen, K. Ma, M. Benezra, L. Zhang, S. M. Cheal, E. Phillips, B. Yoo, M. Pauliah, M. Overholtzer, P. Zanzonico, S. Sequeira, M. Gonen, T. Quinn, U. Wiesner, M. S. Bradbury, *Chem. Mater.* **2017**, 29, 8766.
- [45] S. E. Kim, L. Zhang, K. Ma, M. Riegman, F. Chen, I. Ingold, M. Conrad, M. Z. Turker, M. Gao, X. Jiang, S. Monette, M. Pauliah, M. Gonen, P. Zanzonico, T. Quinn, U. Wiesner, M. S. Bradbury, M. Overholtzer, *Nat. Nanotechnol.* **2016**, 11, 977.
- [46] F. Chen, X. Zhang, K. Ma, B. Madajewski, M. Benezra, L. Zhang, E. Phillips, M. Z. Turker, F. Gallazzi, O. Penate-Medina, M. Overholtzer, M. Pauliah, M. Gonen, P. Zanzonico, U. Wiesner, M. S. Bradbury, T. P. Quinn, *ACS Appl. Mater. Interfaces* **2018**, 10, 4379.
- [47] E. Blanco, H. Shen, M. Ferrari, *Nat. Biotechnol.* **2015**, 33, 941.
- [48] A. E. Nel, L. Mädler, D. Velegol, T. Xia, E. M. V. Hoek, P. Somasundaran, F. Klaessig, V. Castranova, M. Thompson, *Nat. Mater.* **2009**, 8, 543.
- [49] M. P. Monopoli, C. Åberg, A. Salvati, K. A. Dawson, *Nat. Nanotechnol.* **2012**, 7, 779.
- [50] M. Mahmoudi, N. Bertrand, H. Zope, O. C. Farokhzad, *Nano Today* **2016**, 11, 817.
- [51] A. Salvati, A. S. Pitek, M. P. Monopoli, K. Prapainop, F. B. Bombelli, D. R. Hristov, P. M. Kelly, C. Åberg, E. Mahon, K. A. Dawson, *Nat. Nanotechnol.* **2013**, 8, 137.
- [52] J. Bourquin, A. Milosevic, D. Hauser, R. Lehner, F. Blank, A. Petri-Fink, B. Rothen-Rutishauser, *Adv. Mater.* **2018**, 30, 1704307.
- [53] J. Liu, M. Yu, C. Zhou, J. Zheng, *Mater. Today* **2013**, 16, 477.
- [54] M. Yu, J. Zheng, *ACS Nano* **2015**, 9, 6655.
- [55] E. B. Ehlerding, F. Chen, W. Cai, *Adv. Sci.* **2016**, 3, 1500223.
- [56] M. Longmire, P. L. Choyke, H. Kobayashi, *Nanomedicine* **2008**, 3, 703.
- [57] K. Zarschler, L. Rocks, N. Licciardello, L. Boselli, E. Polo, K. Pombo-Garcia, L. De Cola, H. Stephan, K. A. Dawson, *Nanomedicine* **2016**, 12, 1663.
- [58] J. Panyam, V. Labhasetwar, *Adv. Drug Delivery Rev.* **2012**, 64, 61.
- [59] H. S. Choi, W. Liu, P. Misra, E. Tanaka, J. P. Zimmer, B. I. Ipe, M. G. Bawendi, J. V. Frangioni, *Nat. Biotechnol.* **2007**, 25, 1165.
- [60] D. A. Hume, *Curr. Opin. Immunol.* **2006**, 18, 49.
- [61] A. Nel, E. Ruoslahti, H. Meng, *ACS Nano* **2017**, 11, 9567.
- [62] Q. Mu, G. Jiang, L. Chen, H. Zhou, D. Fourches, A. Tropsha, B. Yan, *Chem. Rev.* **2014**, 114, 7740.
- [63] K. E. Sapsford, W. R. Algar, L. Berti, K. B. Gemmill, B. J. Casey, E. Oh, M. H. Stewart, I. L. Medintz, *Chem. Rev.* **2013**, 113, 1904.
- [64] F. M. Veronese, G. Pasut, *Drug Discovery Today* **2005**, 10, 1451.
- [65] K. Knop, R. Hoogenboom, D. Fischer, U. S. Schubert, *Angew. Chem., Int. Ed.* **2010**, 49, 6288.
- [66] K. Pombo García, K. Zarschler, L. Barbaro, J. A. Barreto, W. O'Malley, L. Spiccia, H. Stephan, B. Graham, *Small* **2014**, 10, 2516.
- [67] G. Y. Tonga, K. Saha, V. M. Rotello, *Adv. Mater.* **2014**, 26, 359.
- [68] S. T. Kim, K. Saha, C. Kim, V. M. Rotello, *Acc. Chem. Res.* **2013**, 46, 681.
- [69] M. Vert, K. H. Hellwich, M. Hess, P. Hodge, P. Kubisa, M. Rinaudo, F. Schué, *Pure Appl. Chem.* **2012**, 84, 377.
- [70] Z. Teng, C. Wang, Y. Tang, W. Li, L. Bao, X. Zhang, X. Su, F. Zhang, J. Zhang, S. Wang, D. Zhao, G. Lu, *J. Am. Chem. Soc.* **2018**, 140, 1385.
- [71] Y. Hui, D. Wibowo, Y. Liu, R. Ran, H. F. Wang, A. Seth, A. P. J. Middelberg, C. X. Zhao, *ACS Nano* **2018**, 12, 2846.
- [72] J. Wang, G. Liu, *Angew. Chem., Int. Ed.* **2018**, 57, 3008.
- [73] Q. He, J. Shi, M. Zhu, Y. Chen, F. Chen, *Microporous Mesoporous Mater.* **2010**, 131, 314.
- [74] Q. He, Z. Zhang, Y. Gao, J. Shi, Y. Li, *Small* **2009**, 5, 2722.
- [75] K. Braun, A. Pochert, M. Beck, R. Fiedler, J. Gruber, M. Lindén, *J. Sol-Gel Sci. Technol.* **2016**, 79, 319.
- [76] D. Shen, J. Yang, X. Li, L. Zhou, R. Zhang, W. Li, L. Chen, R. Wang, F. Zhang, D. Zhao, *Nano Lett.* **2014**, 14, 923.
- [77] S. Quignard, G. Mosser, M. Boissière, T. Coradin, *Biomaterials* **2012**, 33, 4431.
- [78] V. Cauda, A. Schlossbauer, T. Bein, *Microporous Mesoporous Mater.* **2010**, 132, 60.
- [79] H. Yamada, C. Urata, Y. Aoyama, S. Osada, Y. Yamauchi, K. Kuroda, *Chem. Mater.* **2012**, 24, 1462.
- [80] J. L. Heinrich, C. L. Curtis, G. M. Credo, K. L. Kavanagh, M. J. Sailor, *Science* **1992**, 255, 66.
- [81] J. H. Park, L. Gu, G. V. Maltzahn, E. Ruoslahti, S. N. Bhatia, M. J. Sailor, *Nat. Mater.* **2009**, 8, 331.
- [82] L. Gu, D. J. Hall, Z. Qin, E. Anglin, J. Joo, D. J. Mooney, S. B. Howell, M. J. Sailor, *Nat. Commun.* **2013**, 4, 2326.
- [83] X. X. He, H. L. Nie, K. M. Wang, W. H. Tan, X. Wu, P. F. Zhang, *Anal. Chem.* **2008**, 80, 9597.
- [84] Q. J. He, Z. W. Zhang, F. Gao, Y. P. Li, J. L. Shi, *Small* **2011**, 7, 271.
- [85] J. Lu, M. Liong, Z. X. Li, J. I. Zink, F. Tamanoi, *Small* **2010**, 6, 1794.
- [86] J. Lu, Z. X. Li, J. I. Zink, F. Tamanoi, *Nanomedicine* **2012**, 8, 212.
- [87] X. Huang, L. Li, T. Liu, N. Hao, H. Liu, D. Chen, F. Tang, *ACS Nano* **2011**, 5, 5390.
- [88] M. Laprise-Pelletier, M. Bouchoucha, J. Laguerre, P. Chevallier, R. Lecomte, Y. Gossuin, F. Kleitz, M. A. Fortin, *J. Mater. Chem. B* **2015**, 3, 748.
- [89] L. Kramer, G. Winter, B. Baur, A. J. Kuntz, T. Kull, C. Solbach, A. J. Beer, M. Lindén, *Nanoscale* **2017**, 9, 9743.
- [90] T. Liu, L. Li, X. Teng, X. Huang, H. Liu, D. Chen, J. Ren, J. He, F. Tang, *Biomaterials* **2011**, 32, 1657.
- [91] T. L. Liu, L. L. Li, C. H. Fu, H. Y. Liu, D. Chen, F. Q. Tang, *Biomaterials* **2012**, 33, 2399.
- [92] C. C. Chou, W. Chen, Y. Hung, C. Y. Mou, *ACS Appl. Mater. Interfaces* **2017**, 9, 22235.
- [93] T. Yu, K. Greish, L. D. McGill, A. Ray, H. Ghandehari, *ACS Nano* **2012**, 6, 2289.
- [94] Q. Wei, Y. Chen, X. Ma, J. Ji, Y. Qiao, B. Zhou, F. Ma, D. Ling, H. Zhang, M. Tian, J. Tian, M. Zhou, *Adv. Funct. Mater.* **2018**, 28, 1704634.

- [95] M. Varache, I. Bezverkhyy, F. Bouyer, R. Chassagnon, F. Baras, F. Bouyer, *J. Nanopart. Res.* **2015**, 17, 356.
- [96] V. Misra, Q. Rahman, P. N. Viswanathan, *J. Appl. Toxicol.* **1983**, 3, 135.
- [97] R. Cheng, F. Feng, F. Meng, C. Deng, J. Feijen, Z. Zhong, *J. Controlled Release* **2011**, 152, 2.
- [98] M. H. Lee, Z. Yang, C. W. Lim, Y. H. Lee, S. Dongbang, C. Kang, J. S. Kim, *Chem. Rev.* **2013**, 113, 5071.
- [99] D. Yang, W. Chen, J. Hu, *J. Phys. Chem. B* **2014**, 118, 12311.
- [100] B. Chen, W. Dai, B. He, H. Zhang, X. Wang, Y. Wang, Q. Zhang, *Theranostics* **2017**, 7, 538.
- [101] L. Han, X. Y. Zhang, Y. L. Wang, X. Li, X. H. Yang, M. Huang, K. Hu, L. H. Li, Y. Wei, *J. Controlled Release* **2017**, 259, 40.
- [102] J. F. Quinn, M. R. Whittaker, T. P. Davis, *Polym. Chem.* **2017**, 8, 97.
- [103] A. Russo, W. Degraff, N. Friedman, J. B. Mitchell, *Cancer Res.* **1986**, 46, 2845.
- [104] B. Arunachalam, U. T. Phan, H. J. Geuze, P. Cresswell, *Proc. Natl. Acad. Sci. USA* **2000**, 97, 745.
- [105] T. Kurz, J. W. Eaton, U. T. Brunk, *Antioxid. Redox Signaling* **2010**, 13, 511.
- [106] J. Alauzun, A. Mehdi, C. Reye, R. J. P. Corriu, *Chem. Commun.* **2006**, 347.
- [107] Z. Xu, K. Zhang, X. Liu, H. Zhang, *RSC Adv.* **2013**, 3, 17700.
- [108] K. Hayashi, T. Maruhashi, M. Nakamura, W. Sakamoto, T. Yogo, *Adv. Funct. Mater.* **2016**, 26, 8613.
- [109] X. C. Huang, L. B. Wu, J. F. Hsu, S. Shigeto, H. Y. Hsu, *Acta Biomater.* **2015**, 23, 263.
- [110] J. L. Vivero-Escoto, W. J. Rieter, H. Lau, R. C. Huxford-Phillips, W. Lin, *Small* **2013**, 9, 3523.
- [111] D. L. Vega, P. Lodge, J. L. Vivero-Escoto, *Int. J. Mol. Sci.* **2016**, 17, 56.
- [112] L. Zhang, W. Zhang, J. Shi, Z. Hua, Y. Li, J. Yan, *Chem. Commun.* **2003**, 210.
- [113] J. Alauzun, A. Mehdi, C. Reyé, R. J. P. Corriu, *J. Am. Chem. Soc.* **2006**, 128, 8718.
- [114] E. Besson, A. Mehdi, C. Reyé, R. J. P. Corriu, *J. Mater. Chem.* **2009**, 19, 4746.
- [115] J. Liu, Q. Yang, L. Zhang, D. Jiang, X. Shi, J. Yang, H. Zhong, C. Li, *Adv. Funct. Mater.* **2007**, 17, 569.
- [116] C. Li, J. Liu, L. Zhang, J. Yang, Q. Yang, *Microporous Mesoporous Mater.* **2008**, 113, 333.
- [117] N. Hao, L. Han, Y. Yang, H. Wang, P. A. Webley, D. Zhao, *Appl. Surf. Sci.* **2010**, 256, 5334.
- [118] R. M. Grudzien, B. E. Grabicka, R. Felix, M. Jaroniec, *Adsorption* **2007**, 13, 323.
- [119] B. E. Grabicka, M. Jaroniec, *Microporous Mesoporous Mater.* **2009**, 119, 144.
- [120] S. Morante-Zarcero, D. Pérez-Quintanilla, I. Sierra, *J. Solid State Electrochem.* **2015**, 19, 2117.
- [121] M. Imamoglu, D. Pérez-Quintanilla, I. Sierra, *Microporous Mesoporous Mater.* **2016**, 229, 90.
- [122] J. Liu, J. Yang, Q. Yang, G. Wang, Y. Li, *Adv. Funct. Mater.* **2005**, 15, 1297.
- [123] P. J. Chiu, S. Vetrivel, A. S. T. Chiang, H. M. Kao, *New J. Chem.* **2011**, 35, 489.
- [124] J. H. Kim, B. Fang, M. Y. Song, J. S. Yu, *Chem. Mater.* **2012**, 24, 2256.
- [125] S. Quignard, S. Masse, G. Laurent, T. Coradin, *Chem. Commun.* **2013**, 49, 3410.
- [126] J. G. Croissant, C. Mauriello-Jimenez, M. Maynadier, X. Cattoën, M. W. C. Man, L. Raehm, O. Mongin, M. Blanchard-Desce, M. Garcia, M. Gary-Bobo, P. Maillard, J.-O. Durand, *Chem. Commun.* **2015**, 51, 12324.
- [127] J. Croissant, X. Cattoën, M. W. C. Man, A. Gallud, L. Raehm, P. Trens, M. Maynadier, J.-O. Durand, *Adv. Mater.* **2014**, 26, 6174.
- [128] S. P. H. Moghaddam, J. Saikia, M. Yazdimamaghani, H. Ghandehari, *ACS Appl. Mater. Interfaces* **2017**, 9, 21133.
- [129] Z. Teng, X. Su, B. Lee, C. Huang, Y. Liu, S. Wang, J. Wu, P. Xu, J. Sun, D. Shen, W. Li, G. Lu, *Chem. Mater.* **2014**, 26, 5980.
- [130] Y. Zhang, M. Dang, Y. Tian, Y. Zhu, W. Liu, W. Tian, Y. Su, Q. Ni, C. Xu, N. Lu, J. Tao, Y. Li, S. Zhao, Y. Zhao, Z. Yang, L. Sun, Z. Teng, G. Lu, *ACS Appl. Mater. Interfaces* **2017**, 9, 30543.
- [131] N. Lu, P. Huang, W. Fan, Z. Wang, Y. Liu, S. Wang, G. Zhang, J. Hu, W. Liu, G. Niu, R. D. Leapman, G. Lu, X. Chen, *Biomaterials* **2017**, 126, 39.
- [132] L. Maggini, I. Cabrera, A. Ruiz-Carretero, E. A. Prasetyanto, E. Robinet, L. De Cola, *Nanoscale* **2016**, 8, 7240.
- [133] K. Möller, T. Bein, *Chem. Mater.* **2017**, 29, 371.
- [134] M. Wu, Q. Meng, Y. Chen, Y. Du, L. Zhang, Y. Li, L. Zhang, J. Shi, *Adv. Mater.* **2014**, 27, 215.
- [135] T. Liu, N. Zhang, Z. Wang, M. Wu, Y. Chen, M. Ma, H. Chen, J. Shi, *ACS Nano* **2017**, 11, 9093.
- [136] L. Yu, Y. Chen, H. Lin, W. Du, H. Chen, J. Shi, *Biomaterials* **2018**, 161, 292.
- [137] L. Hu, J. Meng, D. Zhang, M. Chen, Y. Shu, J. Wang, *Talanta* **2018**, 177, 203.
- [138] L. Sun, D. Wang, Y. Chen, L. Wang, P. Huang, Y. Li, Z. Liu, H. Yao, J. Shi, *Biomaterials* **2017**, 133, 219.
- [139] L. Zhang, L. Wang, H. Yao, F. Xu, Y. Chen, *J. Mater. Chem. B* **2017**, 5, 8013.
- [140] Y. Yang, J. Wan, Y. Niu, Z. Gu, J. Zhang, M. Yu, C. Yu, *Chem. Mater.* **2016**, 28, 9008.
- [141] Y. Chen, H. R. Chen, J. Shi, *Acc. Chem. Res.* **2014**, 47, 125.
- [142] X. Du, J. He, *Nanoscale* **2011**, 3, 3984.
- [143] N. Lu, Y. Tian, W. Tian, P. Huang, Y. Liu, Y. Tang, C. Wang, S. Wang, Y. Su, Y. Zhang, J. Pan, Z. Teng, G. Lu, *ACS Appl. Mater. Interfaces* **2016**, 8, 2985.
- [144] Z. Teng, X. Su, Y. Zheng, J. Zhang, Y. Liu, S. Wang, J. Wu, G. Chen, J. Wang, D. Zhao, G. Lu, *J. Am. Chem. Soc.* **2015**, 137, 7935.
- [145] Z. Teng, J. Zhang, W. Li, Y. Zheng, X. Su, Y. Tang, M. Dang, Y. Tian, L. Yuwen, L. Weng, G. Lu, L. Wang, *Small* **2016**, 12, 3550.
- [146] J. Zhang, L. Weng, X. Su, G. Lu, W. Liu, Y. Tang, Y. Zhang, J. Wen, Z. Teng, L. Wang, *J. Colloid Interface Sci.* **2018**, 513, 214.
- [147] Y. Chen, Q. Meng, M. Wu, S. Wang, P. Xu, H. Chen, Y. Li, L. Zhang, L. Wang, J. Shi, *J. Am. Chem. Soc.* **2014**, 136, 16326.
- [148] P. Huang, X. Qian, Y. Chen, L. Yu, H. Lin, L. Wang, Y. Zhu, J. Shi, *J. Am. Chem. Soc.* **2017**, 139, 1275.
- [149] P. Huang, Y. Chen, H. Lin, L. Yu, L. Zhang, L. Wang, Y. Zhu, J. Shi, *Biomaterials* **2017**, 125, 23.
- [150] M. Wu, W. Chen, Y. Chen, H. Zhang, C. Liu, Z. Deng, Z. Sheng, J. Chen, X. Liu, F. Yan, H. Zheng, *Adv. Sci.* **2018**, 5, 1700474.
- [151] N. Lu, W. Fan, X. Yi, S. Wang, Z. Wang, R. Tian, O. Jacobson, Y. Liu, B. C. Yung, G. Zhang, Z. Teng, K. Yang, M. Zhang, G. Niu, G. Lu, X. Chen, *ACS Nano* **2018**, 12, 1580.
- [152] W. Fan, N. Lu, P. Huang, Y. Liu, Z. Yang, S. Wang, G. Yu, Y. Liu, J. Hu, Q. He, J. Qu, T. Wang, X. Chen, *Angew. Chem., Int. Ed.* **2016**, 56, 1229.
- [153] H. Tian, M. Saunders, A. Dodd, K. O'Donnell, M. Jaroniec, S. Liu, J. Liu, *J. Mater. Chem. A* **2016**, 4, 3721.
- [154] M. Zhou, X. Du, W. Li, X. Li, H. Huang, Q. Liao, B. Shi, X. Zhang, M. Zhang, *J. Mater. Chem. B* **2017**, 5, 4455.
- [155] D. Wang, Z. Xu, Z. Chen, X. Liu, C. Hou, X. Zhang, H. Zhang, *ACS Appl. Mater. Interfaces* **2014**, 6, 12600.
- [156] Y. Li, W. Guo, X. Su, L. Ou-Yang, M. Dang, J. Tao, G. Lu, Z. Teng, *J. Colloid Interface Sci.* **2018**, 512, 134.
- [157] J. Croissant, X. Cattoën, M. W. C. Man, P. Dieudonné, C. Charnay, L. Raehm, J.-O. Durand, *Adv. Mater.* **2015**, 27, 145.

- [158] M. Quesada, C. Muniesa, P. Botella, *Chem. Mater.* **2013**, 25, 2597.
- [159] J. L. Li, Y. J. Cheng, C. Zhang, H. Cheng, J. Feng, R. X. Zhuo, X. Zeng, X. Z. Zhang, *ACS Appl. Mater. Interfaces* **2018**, 10, 5287.
- [160] A. S. Timin, A. R. Muslimov, K. V. Lepik, M. V. Okilova, N. Y. Tsvetkov, A. I. Shakirova, B. V. Afanasyev, D. A. Gorin, G. B. Sukhorukov, *Part. Part. Syst. Charact.* **2017**, 34, 1600417.
- [161] E. A. Prasetyanto, A. Bertucci, D. Septiadi, R. Corradini, P. Castro-Hartmann, L. De Cola, *Angew. Chem., Int. Ed.* **2016**, 55, 3323.
- [162] L. Yang, W. Deng, C. Cheng, Y. Tan, Q. Xie, S. Yao, *ACS Appl. Mater. Interfaces* **2018**, 10, 3441.
- [163] Y. L. Luo, X. C. Huang, W. M. Tu, H. Y. Hsu, *Anal. Chim. Acta* **2016**, 902, 196.
- [164] S. Rahmani, A. Chaix, D. Aggad, P. Hoang, B. Moosa, M. Garcia, M. Gary-Bobo, C. Charnay, A. AlMalik, J. O. Durand, N. M. Khashab, *Mol. Syst. Des. Eng.* **2017**, 2, 380.
- [165] W. Tian, Y. Su, Y. Tian, S. Wang, X. Su, Y. Liu, Y. Zhang, Y. Tang, Q. Ni, W. Liu, M. Dang, C. Wang, J. Zhang, Z. Teng, G. Lu, *Adv. Sci.* **2017**, 4, 1600356.
- [166] Q. Zhang, C. Shen, N. Zhao, F. J. Xu, *Adv. Funct. Mater.* **2017**, 27, 1606229.
- [167] D. A. Keire, E. Strauss, W. Guo, B. Noszal, D. L. Rabenstein, *J. Org. Chem.* **1992**, 57, 123.
- [168] W. W. Cleland, *Biochemistry* **1964**, 3, 480.
- [169] G. R. Choppin, P. Pathak, P. Thakur, *Main Group Met. Chem.* **2008**, 31, 53.
- [170] H. Ehrlich, K. D. Demadis, O. S. Pokrovsky, P. G. Koutsoukos, *Chem. Rev.* **2010**, 110, 4656.
- [171] C. Yoshina-Ishii, T. Asefa, N. Coombs, M. J. MacLachlan, G. A. Ozin, *Chem. Commun.* **1999**, 2539.
- [172] R. Tacke, R. Bertermann, C. Burschka, S. Dragota, *Angew. Chem., Int. Ed.* **2005**, 44, 5292.
- [173] P. Yuan, H. Zhang, L. Qian, X. Mao, S. Du, C. Yu, B. Peng, S. Q. Yao, *Angew. Chem., Int. Ed.* **2017**, 56, 12481.
- [174] H. Kobayashi, M. Ogawa, R. Alford, P. L. Choyke, Y. Urano, *Chem. Rev.* **2010**, 110, 2620.
- [175] C. M. Walters, C. Pao, B. P. Gagnon, C. R. Zamecnik, G. C. Walker, *Adv. Mater.* **2018**, 30, 1705381.